



UNIVERSITY OF

LIVERPOOL

The Energy-absorbing Characteristics of Novel Contoured Core Sandwich Structures

Thesis submitted in accordance with the requirement of the
University of Liverpool for the degree of
Doctor of Philosophy

By
Amit Kumar Haldar
May 2016

Research Papers

- Haldar A.K., Zhou J. and Guan Z (2016), Energy absorbing characteristics of the composite contoured-core sandwich panels (submitted).
- Alia, R.A., Haldar, A.K Cantwell, W.J. and Guan, Z (2015) A Numerical Study of the Energy-absorption Characteristics of Metal Tube-reinforced Polymer Foams- Journal of Sandwich Structures and Materials.
- Haldar, A.K. and Mathew, J. and Cantwell, W.J. and Guan, Z.W. (2014) CAD/CAM Concepts of a Sophisticated Geometric Structure. In: ICCM2014, Fitzwilliam College, University of Cambridge.
- Haldar, A.K. and Cantwell, W.J. and Guan, Z.W. and Alia, R.A. (2014) Mechanical Characterization of CFRP Contour Core Panels. In: ICCM2014, Fitzwilliam College, University of Cambridge.
- Haldar, A.K., Cantwell, W.J., Guan, Z.W. Alia, R.A. and Guan, Zhongwei (2014) The compressive characteristics of novel contour core. In: ECCM16 - 16th European Conference on Composite Materials, University of Seville.
- Alia, R.A. and Guan, Z.W. and Cantwell, W.J. and Haldar, A.K. (2014) Modelling of energy-absorbing behaviour of metallic tubes reinforced polymer foams. In: ICCM2014, Fitzwilliam College, University of Cambridge.
- Alia, R.A. and Cantwell, W.J. and Guan, Z and Haldar, A.K. (2014) The energy-absorbing behaviour of polymer foams reinforced with composite tubes. In: ECCM16, University of Seville.

Abstract

Automobile and aerospace industries are facing problems more and more on reducing the weight and manufacturing cost of a structure, but guaranteeing an equal level of comfort with satisfactory structural performance of components. To overcome these contradictory requirements traditional designs and materials must be revised. Therefore, this research study aims to design, manufacture and characterise the properties of novel contoured-core sandwich structures to obtain strong, stiff and lightweight structures including air ventilation to reduce the danger of deterioration and humidity retraction. Two different contoured profiles, named flat-roof and spherical-roof contoured-cores, were designed to investigate structural response under quasi-static and dynamic loading conditions.

Flat-roof and spherical-roof structures were made from a glass fibre reinforced plastic (GFRP) and a carbon fibre reinforced plastic (CFRP). The composite contoured cores were fabricated using a hot press moulding technique and then bonded to skins based on the same material, to produce a range of lightweight sandwich structures. Testing was initially focused on establishing the influence of the number of unit cells, thickness of the cell wall, width of the cell and the core filled with foam on their mechanical behaviour under quasi-static loading. Fibre fracture and matrix cracking in the composite systems, as well as debonding between the skins and the core, were observed during the compression. The compression strength and modulus were shown to be dependent on the number of unit cells and the cell wall thickness. It has also been shown that the specific energy absorption capacity of the panel increases nonlinearly with increasing the cell wall thickness, with the spherical-roof cores outperforming their flat-roof counterparts. Moreover, the foam filling on the composite contoured-core systems improved the strength as well as specific energy-absorbing characteristics of the structures.

Low velocity impact loading was subsequently performed on the sandwich structures and showed that the values of energy absorption were slightly higher than the tests conducted at quasi-static loading, as a result of the rate-sensitive effects on the damage resistance of the composite material. In addition, blast tests were undertaken to subject the core materials to a much higher strain-rate. Extensive crushing of the contoured cores was observed, suggesting that these structures are capable of absorbing a significant amount of energy under the extreme loading condition.

Finally, the results of these tests were compared with previously-published data on a range of similar core structures. The energy absorbing characteristics of the current spherical-roof systems are shown to be superior to other core structures, such as aluminium and composite egg-box structures.

The finite element models using ABAQUS/explicit were further developed to simulate the quasi-static and low velocity impact response of woven carbon and glass fibre contoured-core designs. Initially, a two dimensional model with Hashin's failure criteria was developed to compare with the experiment. Following this, a user defined material subroutine (VUMAT) was implemented to model the through thickness damage of the contoured-core structures using Hashin's 3D failure criteria. The FE models were validated against the experimental results in terms of the stress-strain responses, the specific energy absorption and the failure mode, with reasonably good correlation. The models developed could be further used for parametric studies to assist in designing and optimising the structural behaviour of contoured-core sandwich structures.

Acknowledgements

Firstly, I would like to express my deep and sincere gratitude to my supervisors, Dr. Z.W. Guan and Prof. W.J. Cantwell for their supervision, inspiration and invaluable support throughout the research period. Also, they have been actively interested in my work and have always been available to advise me and provide assistance in numerous ways. I am also grateful for the scholarship, financial support from the Government of India and university of Liverpool. My sincere gratitude to the technical staff of the School of Engineering at the University of Liverpool, Mr. Jiji Mathew, Mr. Stephen Pennington and Mr. Dave Atkinson for all of their help and support as well as my friends and colleagues including Dr Mohd Ruzaimi, Dr. Alia Ruzanna, Dr. Siti Hajar, Dr. Mohd Zuhri, Mr. Kanna, Mr. Boonkong, Mr. Azmine, Mr. Nassier Mr. Jamil, Mr. Amjad Mr. Rind, Mr Deo, Mr Gideon and Mr Abed. My appreciation is also due to all of the staffs and my friends at the university with whom I have been associating directly or indirectly during my stay in Liverpool.

I should also like to heartily thank my family, especially my father Makhan Chandra, mother Shikha, for all of the support, love, patience and encouragement that they have given me over the years. I am delighted to thank my brother Manish and his wife Sumona, my sister Soma and her husband Sourav and my aunty Pinu Roy for their love and encouragement throughout my PhD in Liverpool. Special thanks to my father in law Mr Ashit kumar, mother in law Dipa, for their prayers, thoughts and motivation. I wish to thank my lovely wife, Anita Haldar, for her love, support, understanding and patience throughout the ups and downs in finishing this study.

Contents

Research Papers	ii
Abstract.....	iii
Acknowledgements.....	v
Contents	vi
List of figures.....	xiv
List of tables.....	xxiii
Chapter 1. Introduction.....	1
1.1 Overview:.....	2
1.2 Sandwich structures.....	3
1.2.1 Skin	5
1.2.2 Core.....	5
1.3 Draping process to form open channel sandwich panels	6
1.4 Applications of contoured core sandwich structures.....	7
1.4.1 Aerospace Applications	8
1.4.2 Automotive applications	8
1.4.3 Marin application	10

1.5	Motivation of the project.....	10
1.6	Project aim and objectives.....	12
1.7	Thesis outline	12
Chapter 2	Literature review	15
2.1	Introduction	16
2.2	Classification and manufacturing process of sandwich cores.....	16
2.2.1	Stochastic cellular material (foam)	17
2.2.2	Periodic cellular material (two dimensional core).....	18
2.2.3	Three dimensional periodic cores	20
2.3	Energy absorption and crashworthiness.....	25
2.3.1	Geometrical characteristics of egg box as an energy absorbing module	
	28	
2.4	Experimental Testing	31
2.4.1	Mechanical response under static compression tests	31
2.4.2	Mechanical response under low velocity impact	34
2.4.3	Mechanical response under blast loading	36
2.5	Finite element modelling and simulation	38

2.5.1	Background of the finite element method.....	38
2.5.2	Numerical simulation and analysis	39
2.6	Modification from egg box to contour core structure for optimum energy absorption.....	43
	Summary of the chapter	47
Chapter 3 Experimental work		48
3.1	Introduction.....	49
3.2	Surface design and mould machining	49
3.2.1	A part model design by scoping the design parameters of the structure	51
3.2.2	Transfer the part model to triangulate surfaces in ProToolmaker(CAM) to create the CNC programme in G codes	54
3.2.3	Set the raw materials in Haas CNC milling machine and manufacture the desired mould.....	56
3.3	Composite materials used in present work	58
3.4	Specimen Preparation	58
3.4.1	Fabrication of the contoured core	58
3.4.2	Skin manufacturing	63

3.4.3 Bonding between skin and core	63
3.5 Foam filled contoured sandwich panels.....	66
3.6 Mechanical Properties of Materials	67
3.6.1 Tensile tests on the GFRP and CFRP composites	68
3.6.2 Compression tests on rigid PU foam	68
3.7 Static compression tests of contoured-core sandwich structures.....	69
3.8 Low velocity impact tests	70
3.9 Blast tests	73
Summary of the chapter	76
Chapter 4 Results and discussion	77
4.1 Introduction	78
4.2 Mechanical properties of the materials	78
4.2.1 Tensile tests on the composites.....	78
4.2.2 Compression tests on the rigid polyurethane foam.....	80
4.3 Static compression tests on contoured cores	81
4.3.1 The compression behaviour of the flat roof contoured core	81

4.3.2	The compression behaviour of the flat-roof contoured core sandwich structures	82
4.3.3	The Effect of edge constraint on contoured cores	85
4.3.4	Compression on foam-filled flat roof contoured panels	90
4.4	Compressive behaviour of the flat roof contoured panels subjected to impact loading.....	92
4.5	Novel spherical roof contoured structures under quasi-static compression ..	96
4.5.1	Compressive response of the GFRP spherical roof contoured structures	96
4.5.2	Compressive response of the CFRP spherical roof contoured structures	97
4.5.3	Compression response of composite contoured structures as a function of cell wall thicknesses	99
4.6	The effect of varying the number of unit cells	105
4.7	Energy absorption	109
4.8	Compression on the foam filled spherical roof contoured panels.....	113
4.9	Fracture modes	114
4.9.1	Failure of the CFRP core	114

4.9.2	Failure of the GFRP core	118
4.10	The Compressive behaviour of spherical roof contoured panels at high strain rates	120
4.11	Blast tests.....	124
4.12	Comparison of the current contoured core panels with other energy-absorbing cores	127
	Summary of the chapter	130
Chapter 5.	Finite element modelling	131
5.1	Introduction:.....	132
5.2	Constitutive model	132
5.2.1	Contoured composite	132
5.2.2	Damage model for the fibre-reinforced composites	134
5.3	Quasi-static compression modelling of contoured core sandwich structure	138
5.3.1	Selection of the part and element.....	138
5.3.2	Loading and boundary conditions.....	138
5.3.3	Interaction properties	139

5.3.4	Mesh generation and control.....	139
5.3.5	Model convergence.....	141
5.3.6	Modelling data output.....	144
5.3.7	Quasi-static compression results from the two dimensional finite element simulations	145
5.4	Dynamic finite element modelling.....	151
5.4.1	Input data	151
5.4.2	Output data.....	152
5.4.3	Results from the numerical analysis	152
5.5	3D finite element modelling.....	156
5.5.1	Mesh generation, boundary and loading conditions	156
5.5.2	Modified 3D Hashin's failure criteria.....	159
5.6	Implementation of the material model in ABAQUS/Explicit.....	161
5.6.1	Cohesive elements and material properties.....	162
5.7	3D Numerical modelling of the compression response of flat-roof and spherical-roof contoured cores.....	163
5.8	The effect of varying the number of unit cells	170

5.9	Specific energy absorption	171
	Summary of the chapter	173
Chapter 6.	Conclusions and recommendations for future work	174
6.1	Introduction:	175
6.2	Conclusions of the research work	175
6.3	Recommendations for future work.....	179
References.....		181

List of figures

Figure 1.1 Applications of composite materials in various industries [1].	3
Figure 1.2 Sandwich structure.	4
Figure 1.3 Distribution of composite materials and locations on the A380 [2].	4
Figure 1.4 VeSCo concept [3].	6
Figure 1.5 Number of fatalities per year due to the collision between the pedestrian, pedal cyclists and HGVs [9].	9
Figure 1.6 Vehicle-pedestrian collision, highlighting impacts to the passengers and pedestrians [9, 10].	10
Figure 2.1 Division of cellular materials into stochastic (open cell and closed cell) and periodic (2D and 3D) structures [22].	17
Figure 2.2 (a) Schematic diagram of square-honeycomb core [26] and (b) photograph of an assembled composite square-honeycomb core [27].	19
Figure 2.3 Classification of corrugated-core sandwich panels [28].	19
Figure 2.4 (a) Sinusoidal corrugated-core made from carbon fiber and (b) Schematic geometry of sinusoidal core for morphing wing [34].	20
Figure 2.5 Micro-lattice blocks manufactured by SLM technology.	21
Figure 2.6 : Chevron folded paper [46]	22

Figure 2.7 Schematic diagram of a Egg-Box core [47]	23
Figure 2.8 Composite egg-box and cross sectional dimensions of the core: (a) overall	24
Figure 2.9 The egg box energy absorbing structure [71].....	28
Figure 2.10 Egg box deformation procedures [72].....	30
Figure 2.11 Schematic diagram of the crush stages of a unit cell of an aluminium egg- box structure under compression [9].....	32
Figure 2.12 Schematic diagram of low velocity impact test rig and Instrumentation of the impact machine [77].....	34
Figure 2.13 Schematic of the experimental rig used for blast test [88].	37
Figure 3.1. Photographs of the (a) aluminium flat-roof contoured moulds (egg box mould) (b) cross section of the geometry.	50
Figure 3.2 Plan view and section Geometry of contoured profile.	51
Figure 3.3 detail design of the cell.....	53
Figure 3.4 Material left for finishing is 0.5mm in x, y and z directions.	55
Figure 3.5 Milling cutter on smooth concave profile.	55
Figure 3.6 Milling cutter and work piece in Haas CNC milling machine	57
Figure 3.7 Spherical roof countoured mould.	57

Figure 3.8 A roll of composite prepreg in the as-received condition before cutting to a size of 240 mm x240 mm.....	59
Figure 3.9 Photograph of the Meyer hot press machine.	60
Figure 3.10 Heating cycle for the curing of (a) Glass fibre and (b) Carbon fibre prepregs.....	61
Figure 3.11 Photograph of spherical roof contoured core specimens following removal from the mould.....	62
Figure 3.12 Spherical roof contour core specimens.....	62
Figure 3.13 Schematic diagram of a spherical top dome covered with glue until the filling of an imaginary cylinder.	64
Figure 3.14 Adhesive been applied to (a) Flat-roof sample; (b) Spherical-roof sample.	65
Figure 3.15 Foam filled spherical roof contoured panels (a) GFRP (b) CFRP	66
Figure 3.16 (a) Free-rise in the rigid PU foam and (b) a cube-shaped foam block on the weight scale.....	67
Figure 3.17 Tensile test geometry for a composite specimen.....	68
Figure 3.18 The rigid PU foam under compression loading.....	69
Figure 3.19 A specimen under compression loading using Universal Testing Machine INSTRON 4505.	70

Figure 3.20 The instrumented drop-weight impact test set-up adopted for testing the contoured-core sandwich structures.....	71
Figure 3.21 (a) Photograph of the ballistic pendulum used for conducting the blast tests and (b) schematic of the detonator and blast tube arrangement	74
Figure 4.1 Tensile stress-strain curves for the GFRP and CFRP specimens.....	79
Figure 4.2 Failed composite samples.....	79
Figure 4.3 Compression stress-strain behaviour of the rigid PU foam.....	81
Figure 4.4 Quasi-static stress-strain traces for unbonded (without skin) 2x2 flat roof contoured cores.	82
Figure 4.5 Quasi-static stress-strain traces on bonded 2x2 flat roof contoured core panels, the wall thicknesses are indicated in the figure.	84
Figure 4.6 Progressive crushing of the flat roof glass fiber contoured panel during a compression test.....	85
Figure 4.7 The platen arrangement used to restrict the deformation of the specimen during compression testing.	86
Figure 4.8 Quasi-static stress-strain curves of constrained 2x2 flat-roof contoured GFRP and CFRP core.	87
Figure 4.9 Images of progressive damage development in the constrained flat-roof contoured systems.....	88

Figure 4.10 A comparison of the bonded, unbonded and constrained 2x2 flat-roof contoured structures under quasi-static load.....	90
Figure 4.11 Stress-strain traces following tests on the foam filled 2x2 flat-roof panels.	92
Figure 4.12 The stress-strain relationship from low velocity impact tests on 2x2 flat roof contoured panels.....	95
Figure 4.13 Specific energy absorption of 2x2 flat-roof contoured panels made of CFRP and GFRP.....	96
Figure 4.14. Mechanical response of the 3x3 bounded and unbounded contoured structures subjected to compression.....	98
Figure 4.15 Fractured surfaces of GFRP and CFRP.....	99
Figure 4.16 Crushing process in the GFRP spherical roof contoured core.	100
Figure 4.17 Quasi-static stress-strain traces for the 3x3 unbonded spherical roof contoured structures.	101
Figure 4.18 Quasi-static stress-strain traces of 3x3 bonded spherical roof contoured panels.	103
Figure 4.19 Comparison of the compression strength and stiffness properties as a function of cell wall thicknesses of the 3x3 spherical roof contoured panels.	105

Figure 4.20 Photograph of damage in GFRP samples based on (a) (1x1) and (b) (3x3) unit cells.....	107
Figure 4.21 Photograph of damage in CFRP samples based on (a) (2x2) and (b) (3x3) unit cells.....	108
Figure 4.22 Compression strength and stiffness responses to the different number of unit cells for (a) GFRP (b) CFRP.	109
Figure 4.23 Comparison of Energy abortion of GFRP and CFRP as a function of (a) Cell wall thicknesses and (b) Number of unit cells.	111
Figure 4.24 Stereo-microscopic images of the fractured surfaces of (a) GFRP (b) CFRP.....	112
Figure 4.25 Stress-strain traces on foam filled 3x3 spherical roof contoured panels.	114
Figure 4.26 Step-wise collapse response of the 3x3 CFRP spherical core.....	115
Figure 4.27 Summary on the fractured surfaces of spherical-roof core.	117
Figure 4.28 Step-wise collapse response of 3x3 GFRP spherical core.....	118
Figure 4.29 Summary on fractured surface of spherical roof core.	120
Figure 4.30 Dynamic compression tests on 3x3 spherical roofed panels.....	122
Figure 4.31 Specific energy absorption of the 3x3 spherical roof contoured structures made of CFRP and GFRP.....	123

Figure 4.32 Percent crush versus applied impulse for the spherical roof contoured sandwich panels.	125
Figure 4.33 Blast load deformation on 10 gram mass of explosives (a) GFRP and (b) CFRP.....	126
Figure 4.34 Energy absorption per unit mass of the current panels and data from the literature.	128
Figure 4.35 Energy absorption per unit mass as a function of peak stress.	129
Figure 5.1 Loading direction, boundary conditions and assembly of the contoured core model between two platens.	139
Figure 5.2 Typical meshes used in numerical contoured core modelling.....	140
Figure 5.3 An imperfection sensitivity analysis study for the GFRP contoured core.	142
Figure 5.4 Variation of the prediction to test data and CPU time with element size.	144
Figure 5.5 Stress-strain traces for the flat-roof contoured core panels, with the predictions from the 2-D imperfection finite element model.	146
Figure 5.6 Stress-strain traces for the spherical-roof contoured core panels, with the predictions from the 2-D imperfection finite element mode.	148
Figure 5.7 Progressive failure of GFRP spherical-roof panels (*displacement ratio=displacement/the original height of the core).	149

Figure 5.8 Progressive failure of CFRP spherical-roof panels (*displacement ratio=displacement/the original height of the core).....	150
Figure 5.9 Low-velocity stress-strain traces following compression tests on the contoured panels.	154
Figure 5.10 Low-velocity stress-strain traces following compression tests on the spherical-roof contoured panels.....	155
Figure 5.11 Deformation of spherical-roof GFRP contoured under low-velocity impact loading.....	156
Figure 5.12 The geometry, mesh, boundary and loading conditions of contoured core based sandwich panels (the top skin and loading platen are removed).	157
Figure 5.13 Quasi-static stress-strain traces following compression tests on the flat-roof contoured panels.....	165
Figure 5.14 Various level of deformation in the flat-roof glass fibre contoured panel during compression (*displacement ratio=displacement/the original height of the core).	166
Figure 5.15 Quasi-static stress-strain traces following compression tests on the spherical-roof contoured panels.....	167
Figure 5.16 Various level of deformation in the spherical-roof glass fibre contoured panel during compression.	168
Figure 5.17 Ultimately collapsed flat-roof contoured core (legend in meter).	168

Figure 5.18 Crushed core of spherical-roof contoured panels (*displacement ratio=displacement/the original height of the core).....	169
Figure 5.19 Comparison of the 1x1 and 2x2 unit cells of GFRP predicted by the numerical model with the experimental samples.....	170
Figure 5.20 Comparison of the 1x1 and 2x2 unit cells of CFRP predicted by the numerical model with the experimental samples.....	171
Figure 5.21 Specific energy absorption of Spherical-roof and Flat-roof contoured structures made of CFRP and GFRP.	172

List of tables

Table 3.1. Details of the raw materials Glass Fibre and Carbon Fibre Reinforced.	59
Table 4.1 Test values used to test the flat roof contoured panels.	93
Table 4.2 Properties and characteristics of the contour core structures.....	111
Table 4.3 Test values used to test the spherical roof contoured panels.	121
Table 4.4 Details of blast pendulum.	125
Table 5.1 Summary of the elasticity properties of the carbon and glass fibre/epoxy materials [7, 122, 123].	134
Table 5.2 Summary of the damage initiation and fracture energy data of the carbon and glass fibre/epoxy materials [7].	137
Table 5.3 Details of mesh sensitivity analysis.	143
Table 5.4 Properties of the woven fabric glass-fibre reinforced plastic, (GFRP) and the woven fabric carbon-fibre reinforced plastic, (CFRP) [7, 122, 123].	158

Chapter 1. Introduction

1.1 Overview:

There is a constant pressure on the automotive, aerospace and naval industries to come up with lightweight structural solutions to improve the fuel efficiency without sacrificing the structural performance of components. In addition, the design choices are subjected to stringent cost constraints as innovations in automotive engineering are seldom successful unless both performance and cost advantages prevail. Therefore, these engineering challenges have led a number of researchers to design and manufacture lightweight structures that can offer a higher strength and absorb more energy under various loading conditions.

One of the ways to achieve weight savings is by replacing metals with composite materials. A composite material can have two or more than two distinct constituents or phases in assembly, whereby both constituents are present in reasonable proportions, each having different properties, resulting in altogether different properties for the composite material. The constituents that are present in a continuous form and often, but not always, present in the greater quantity is termed the ‘matrix’, such as polymeric materials. In general, polymers are known to have a poor strength and a low Young’s modulus. The second constituent is termed as the reinforcing phase, or the ‘reinforcement’, with the purpose of enhancing or reinforcing the mechanical properties of the matrix, such as carbon fibers. In general, the reinforcement is stronger and stiffer than the matrix. The breakdown of composite application in various industries is shown in Figure 1.1. Manufacturers in many industries are becoming increasingly interested in composite materials, as they are useful in all areas from simple to complex applications.

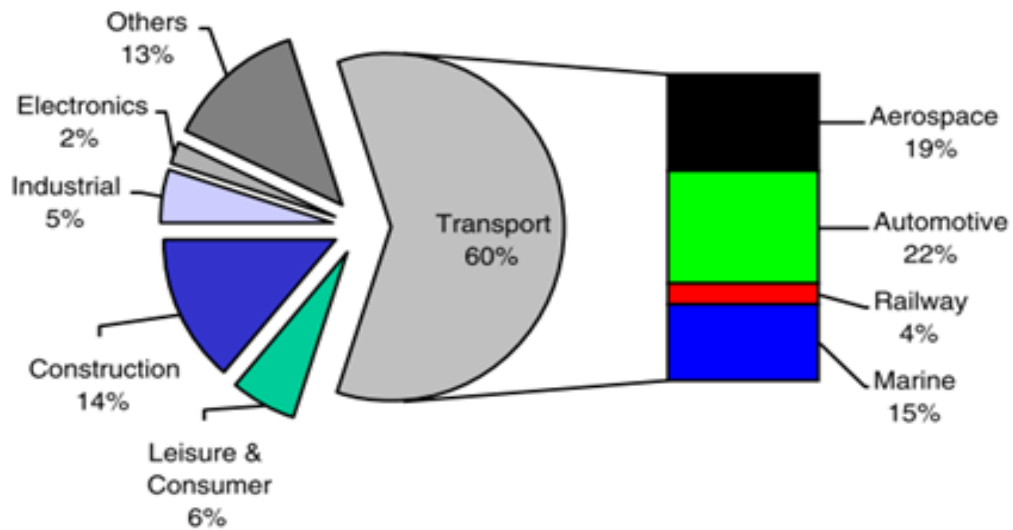


Figure 1.1 Applications of composite materials in various industries [1].

1.2 Sandwich structures

Recently, composites have also been widely used either in a monolithic form or in a sandwich structure. A sandwich structure typically consists of two thin but stiff skins, made from a fully dense material, and separated by a thick and light core, as shown in Figure 1.2. The result of this construction is a structure with a high bending stiffness and strength but a low overall density. In fact, the specific strength of a sandwich structure is always superior to that of a monolithic structure made from the same material and having the same weight [1].

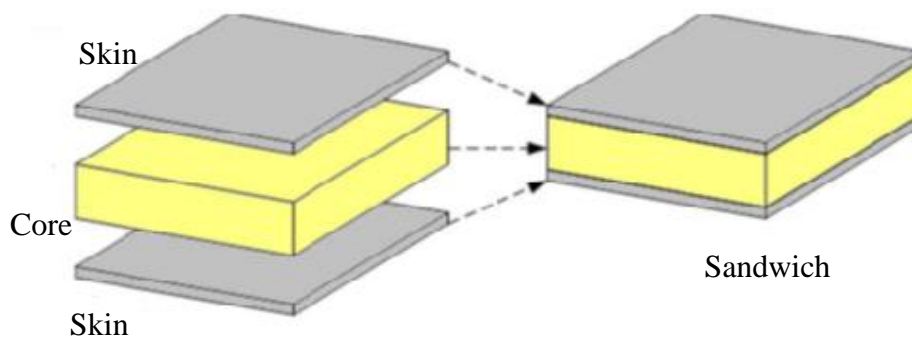


Figure 1.2 Sandwich structure.

For more than a half-century, there has been a growing increase in the use of composite sandwich structures in a wide range of applications. These applications include structures in the automotive, aerospace, naval and construction industries. For example, the largest airliner in the sky, the Airbus A380, is an excellent example of the evolution and the use of the composite materials [2]. In Figure 1.3, the distribution of composite materials in the A380 is shown. The increased use of carbon fibre reinforced plastic (CFRP) laminates has resulted in a drastic weight reduction in the A380. The major material improvements in the A380 are a CFRP composite centre wing box, which is a first in commercial aviation. CFRP has also replaced aluminium in the lateral panels and the secondary rib.

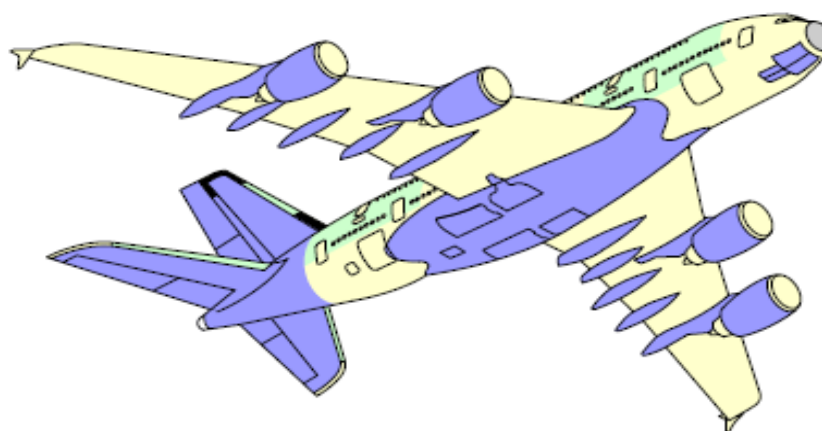
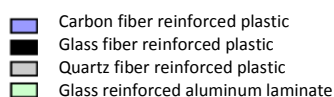


Figure 1.3 Distribution of composite materials and locations on the A380 [2].

1.2.1 Skin

The skin materials are one of the important components in a sandwich structure. It can be divided into fibre reinforced composites and non-composites (metals, woods). For non-composites, the most common skin material is an aluminium sheet metal. Its applications include refrigerated transportation containers and construction panels. Most fibre reinforced composites are employed as the skins in a sandwich structure, with the most common ones as glass fibre, carbon fibre and aramid. The composite skin may be composed of different architectures, such as chopped strand mat (CSM), unidirectional (UD) and woven roving (WR). UD skin has a high strength in one direction (fibre direction only), whereas a WR skin has a moderate strength in two-perpendicular directions. In general, composites skins have an excellent strength, stiffness, corrosion resistance, thermal properties and are lightweight in nature. However, composites are still more expensive than sheet metals and sometimes require complex manufacturing processes.

1.2.2 Core

The second important component in a sandwich structures is the core material. The core in a sandwich structure may be of the various types of cellular material, such as honeycomb, foam or wood. The most common foams are made from polymers. In general, polymeric foams are good as energy absorption devices and heat insulators. Unfortunately, polymeric foams are based on a system of closed channels and are very conservative. Sandwich structures with closed channel cellular materials often contain air and humidity. Containing humidity in aircraft sandwich structures is one of the problems for aviation industries. The weight of the sandwich structure can increase by humidity accumulation, which may lead degradation of core properties.

To solve those problems associated with humidity accumulation, Airbus [3] has developed the sandwich fuselage concept, called the Ventable Shear Core (VeSCo). Figure 1.4 shows schematically the VeSCo concept. This VeSCo concept provides a maximum weight saving, while still offering attractive protection against impact and noise. The outer skin provides the aerodynamic surface and inner the skin provide a smooth surface, while in between the two skins, an open channel core material is ventable in order to avoid moisture accumulation.

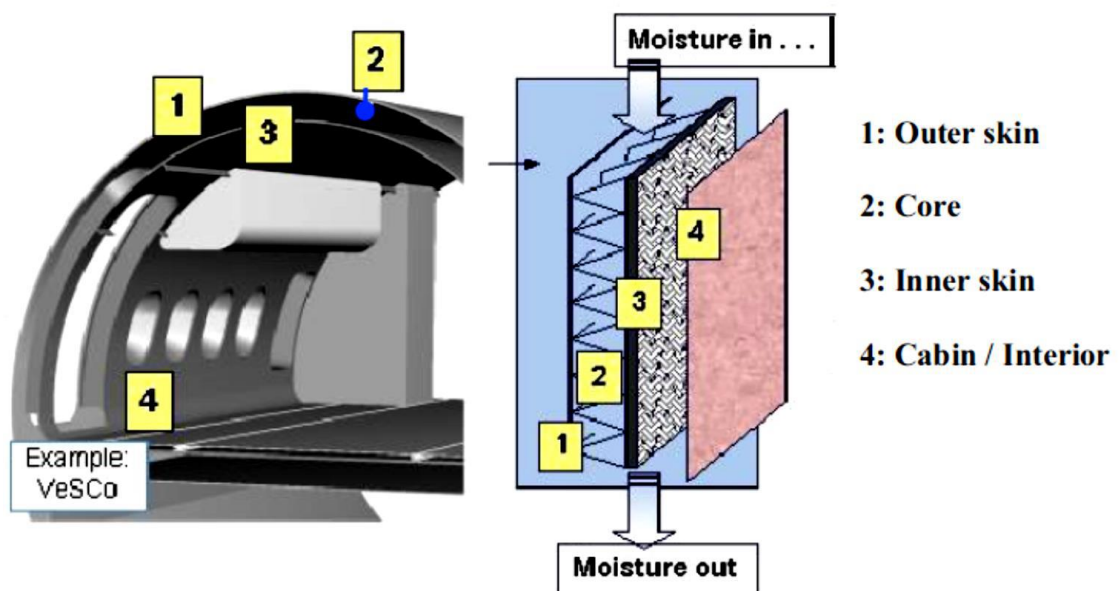


Figure 1.4 VeSCo concept [3].

1.3 Draping process to form open channel sandwich panels

Sandwich structures with curved mid-planes are difficult to drape due to complex shape. As a result, sandwich constructions are mostly limited to flat panel-type of structures reducing their scope of applications. In addition the manufacturing cost is another concern to design and fabricate a sandwich structure. The compression

moulding process and vacuumed autoclave draping are relatively low cost methods for manufacturing an open channel core geometry [2, 4]. However, it is important to identify and understand the failure mechanisms that occur in composite laminates, before draping into the complicated structures, which can vary greatly from thin to thick laminates. This can be understood from the fact that failure in thick composites often involves more complex fracture modes. From a statistical point of view, there is a greater possibility of the thicker composite containing larger defects. Generally, failure occurs as a result of fiber instability, due to misalignment of the reinforcement. Thicker composite contains more layers, leading to a greater possibility of fibre misalignment [5].

When prepregs are draped onto 3-D moulds they tend to deform to fit into the mould surface which induces different fiber misalignments, according to the position and local geometry of the mould. During the design stage of a 3-D structure by a draping process [6], information on the local deformations and the corresponding material properties is essential, before and after the draping, to predict the performance of the final product. The mechanical properties of corrugated sandwich panels draped into a predefined mould, based on three different materials, were investigated in order to gauge their overall potential. In this current project a similar method was followed as described by Rejab and Cantwell [7], to manufacture a curved and open channel based geometry, termed as contoured core sandwich structure.

1.4 Applications of contoured core sandwich structures

The three-dimensional periodic contoured core that is the focus of this research has its important applications in the automotive, aerospace and marine industries. Such the core is of the high energy absorption, high strength-to-weight ratio, three dimensional

open channel designs and low manufacturing cost. This makes it a suitable design to replace other existing core designs for various purposes as described below.

1.4.1 Aerospace Applications

In morphing applications, where large shape changes are expected, the design of a suitable application is a huge challenge and a key issue. In general, the wing structures are required to be stiff in order to withstand aerodynamic pressure loads, while being flexible for the underlying morphing wings. Contoured composites have a great potential to replace the conventional wing-materials. Other than the wing-materials, it can also be used on flight control surfaces, cabin floor boards, and other applications.

1.4.2 Automotive applications

The number of serious accidents and fatalities from accidents between commercial vehicles and vulnerable road users (VRUs) is still high and shows no sign of declining. For pedestrians, this is traumatic due to high incompatibility (very high stiffness) of vehicle fronts. Though the accidents involving collision between pedestrian and heavy goods vehicles (HGVs) shows a bigger picture of the European Union (EU) [8], statistical data still indicate that more than 1400 VRUs in the 15 foremost EU member states lose their lives every year due to accidents with HGVs [8]. Figure 1.5 represents the statistical data [9], for the number of fatalities of pedestrian and pedal cyclists in Great Britain between the years 1994–2002. Pedestrian fatalities show a decreasing trend from 1994 to 1998 and there is a sharp rise in the statistics until about mid-2001. Thereafter there is a decrease in the number of fatalities until about the year 2002; however, the figures are relatively higher than those in the 1990s as shown in Figure 1.5.

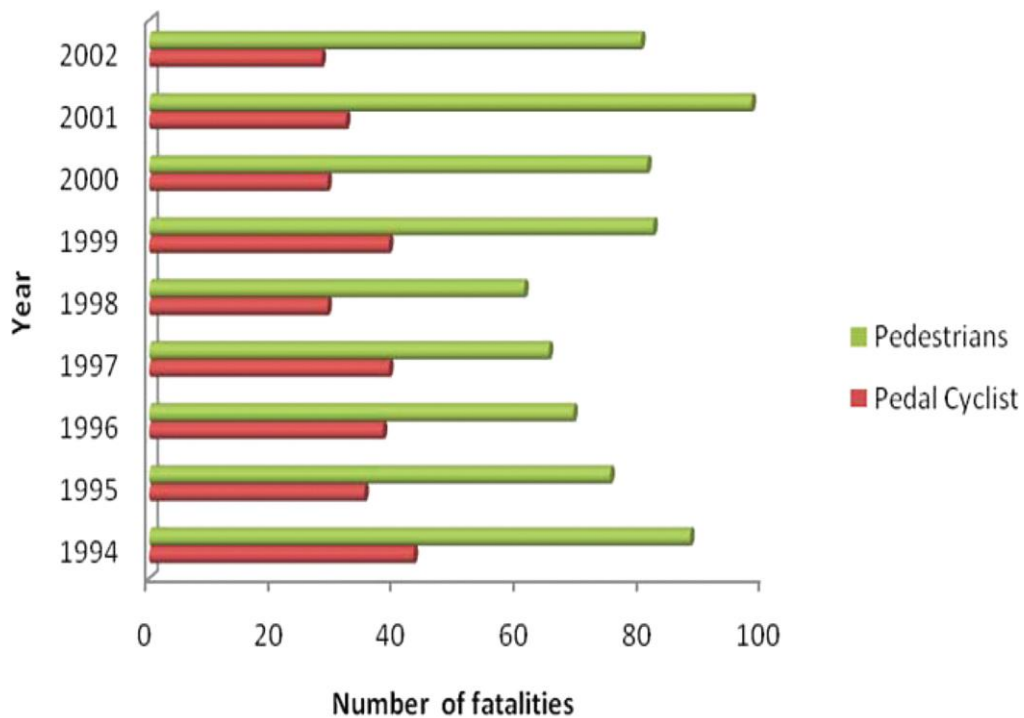


Figure 1.5 Number of fatalities per year due to the collision between the pedestrian, pedal cyclists and HGVs [9].

In Europe, 4% of all fatal road accidents can be categorised as HGV–VRU accidents, 28% of all fatalities resulting from collisions with vehicles are a result of HGV–VRU accidents and 13% of all VRUs involved in HGV accidents die [9]. Hence, Contoured core panels could be designed and used with that purpose for pedestrian’s injuries mitigation in the event of an accident with a vehicle as shown in Figure 1.6. Depending on the places that the panels were mounted, not only the pedestrians, but also the vehicle passenger would benefit, if there were impacts between them and the internal parts of the car/truck (Figure 1.6). Due to low incompatibility and high energy absorption capacity these contoured composites can minimise the kinetic effect during the collision.

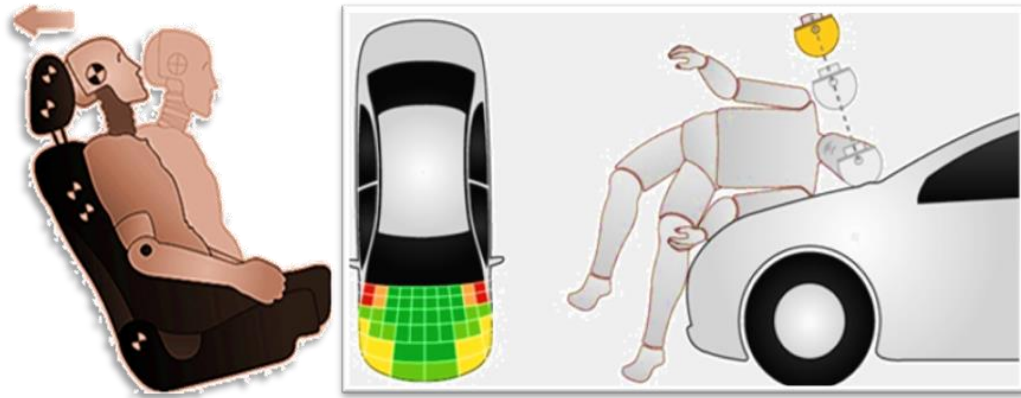


Figure 1.6 Vehicle-pedestrian collision, highlighting impacts to the passengers and pedestrians [9, 10].

1.4.3 Marin application

Almost 90% of boats and ships are constructed using either carbon and glass fibre-reinforced polyester or vinyl ester resin, Such as life boats, fishing boats, sail boats, yachts and dinghies. Carbon fibre-reinforced epoxy laminates and carbon fibre-reinforced epoxy skins with either foam core or honeycomb core based sandwich laminates have been used as the structural components, such as the complete hull, deck, keel, boom, mast and other structural members.

1.5 Motivation of the project

It is clear that the main objective of producing sandwich cores is to obtain strong, stiff and lightweight structures including air ventilation, which can help to reduce the danger of deterioration and humidity retraction. In addition, the manufacturing cost is another concern when designing and fabricating a sandwich structure.

Considering the role of energy-absorption, various geometrical shapes have been considered for energy- absorbing geometry such as tubes, frusta, multicorner columns and struts [11]. The appropriate shape for energy absorbing structures will depend on

the use and the type of loading and the constraints. Lam et al [12] evaluated the energy-absorption behaviour of a flat topped grid-domed cellular structure made of different textile composites and identified the effects of fibre type, fibre volume fraction and fibre architecture on energy absorption. Yu et al. [13] evaluated the compressive behaviour and energy-absorption characteristics of grid-domed composites made of knitted fabrics and their response with several conventional foams. Soutis and Poubady [14] and Velecela et al. [15] investigated the energy absorption capacities of flat composite specimens subjected to ‘edgewise compression’ to understand the collapse mechanisms and to identify the most effective boundary condition for inducing progressive failure of specimens.

A potential new class of energy-absorbing structure based on aluminium egg box was introduced by Zupan et al. [16]. Experiments suggested that egg-box structures deform by either the rotation of a stationary plastic hinge or by a travelling plastic knuckle, depending upon the in-plane kinematic constraints imposed upon the egg-box. Egg-box shaped energy-absorbing structures made of fabric composites were fabricated to determine the compressive characteristics and energy-absorption capacity. The energy absorption per unit mass of composite egg-box panels made of different types of material and stacking sequences were calculated and compared [17]. Compressive tests on foam-filled composite egg-box panels were carried out to assess their performance as energy absorbers. The material type, the number of plies and the stacking angle were varied. It was found that the foam-filled composite egg-box sandwich panels offered a good energy absorption capacity with a stable collapse response resembling an ideal energy absorber [18]. A very closed geometry similar to the egg-box, but modified with the addition of curved shape spherical face called

contoured core, has been studied in the current project to understand the mechanical behaviour of the structure under different loading conditions.

1.6 Project aim and objectives

Based on the above discussion the principal aim of this research work is to investigate the mechanical properties of these novel contoured-core sandwich structures. The research focuses on composites (glass fibre reinforced plastic and carbon fibre reinforced plastic) structures, with the project objectives as:

- i) To design and manufacture contoured cores and the related sandwich structures.
- ii) To investigate the mechanical performance of contoured core sandwich structures subjected to static compression, low velocity impact and blast loading.
- iii) To understand the in-depth failure mechanisms in contoured core sandwich structures subjected to different loading conditions.
- iv) To compare the energy absorption capability of contoured core structures with the similar designs (egg-box) used for sandwich structures.
- v) To develop finite element models of contoured core sandwich structures by proposing suitable constitutive models and failure criteria.
- vi) To validate these finite element models using experimental results.

1.7 Thesis outline

At the beginning of each chapter, a brief overview of the chapter will be given. A summary relevant to the topic will be concluded at the end of each chapter to highlight the main findings. This thesis consists of six chapters as follows:

Chapter 1: Introduction

This chapter presents the significance of the research in different industrial applications. The main focus was on transportation industries, includes aerospace and heavy vehicles applications which underlining its main objectives for accomplishing the benefits of this study.

Chapter 2: Literature review

This chapter gives an overview on the design and manufacturing methods of sandwich structures, geometric characteristics including energy absorption and crashworthy. Previously published experimental techniques to find out the mechanical response under compression, low velocity impact and blast loading will be presented. Finite element modelling that is related to this research will also be summarized with previously published examples.

Chapter 3: Experimental procedures

This chapter describes the experimental procedures of various tests conducted on the materials used in the present study. These includes specimen manufacturing methods and process, test setups to perform tensile, quasi-static compression, low velocity impact and blast tests. This provides the parameters used to measure the performance of the tests. It also gives the details of the equipment necessary for these test methods.

Chapter 4: Experimental results and discussions

This chapter shows the experimental results obtained from tensile, quasi-static compression, low velocity impact and blast tests. The behaviour of two different geometries, called spherical-roof and flat-roof contoured core specimens under static

and low velocity tests, are presented and analyzed. The influence of the design parameters, thickness of the specimens, materials and the specimen sizes are explained in detail. An in-depth understanding of the crushing response by examining the failure mechanisms in each structure is presented here. Energy absorption capability of these contoured core structures are also presented and compared with the previously investigated egg-box sandwich structures.

Chapter 5: Finite element modelling

This chapter describes the steps followed in order to predict and simulate the response of the structures studied in the finite element analysis. The finite element models using ABAQUS/explicit are developed to simulate the quasi-static and low velocity impact response of woven carbon and glass fiber contoured core designs. The finite element models developed are validated against the experimental results presented in Chapter 4. This will consider the effect of geometry, varying thicknesses and the size of the specimens. Initially, a two dimensional model will be developed to verify the experimental results, followed by a three dimensional model. A user defined material subroutine (VUMAT) is developed to define the mechanical constitutive behaviour and Hashin's 3D failure criteria suitable for simulating the composite failure through its thickness in composite contoured core structures.

Chapter 6: Conclusions

This chapter discusses the results obtained by the different tests performed in a series of structures designed to absorb energy. It also summarizes the output of the whole project and presents recommendations for future work.

Chapter 2 Literature review

2.1 Introduction

This chapter presents a review of the relevant work published on sandwich panels made with different cores subjected to quasi-static, low velocity impact and blast loading. The design and manufacturing processes of sandwich panels are briefly reviewed. Other important aspects, such as the effect of geometrical parameters on the behaviour of the core under quasi-static, low velocity impact and blast loading, are also reviewed and explained. Additionally, the research work on cellular egg-box sandwich structures is discussed, with various examples.

2.2 Classification and manufacturing process of sandwich cores

The simplest type of sandwich consists of two thin, stiff and strong sheets of dense material separated by a thick layer of low density material which may be much less stiff and strong [19]. A range of sandwich cores were designed and manufactured to develop lightweight structures, which have higher compressive strength, stiffness and energy absorption. From balsa wood to polymeric foams and honeycomb cores, recently more research activities are covering investigation of ideal lightweight cellular core candidates for sandwich structures. Ashby [20] explained that the mechanical properties of sandwich core materials are controlled by three factors, i.e. (1) the relative density of the core, (2) the properties of the parent material and (3) the topology of the cellular materials.

To improve the mechanical response of sandwich panels, many different cellular core topologies have been developed. Those cellular structures can be divided into stochastic and periodic cellular structures, which are further classified as open cell, closed cell, 2D cell and 3D cell as illustrated in Figure 2.1. Open and closed cells are falling in the schematic category [21]. On the other hand, a precise unit cell, which is

repeated in an array to form periodic structures, can be two-dimensional open channel or three-dimensional truss or textile based assemblies [22].

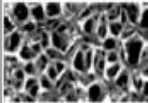






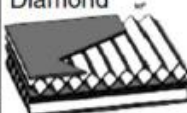

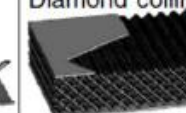




Cellular materials					
Stochastic		Periodic			
Open cell	Closed cell	2D		3D (lattice)	
		Honeycombs	Prismatic	Truss	Textile
		Hexagonal 	Triangular 	Tetrahedral 	Diamond textile 
		Square 	Diamond 	Pyramidal 	Diamond collinear 
		Triangular 	Navtruss 	3D kagome 	Square textile 

Figure 2.1 Division of cellular materials into stochastic (open cell and closed cell) and periodic (2D and 3D) structures [22].

2.2.1 Stochastic cellular material (foam)

There are two types of foams, namely polymeric and metallic foam. These can be regraded into two other sub categories, which are called open cell and closed cell. These cell types are identified by their densities, where a closed cell foam has a much higher density than an open cell one. Polymer foams are manufactured by introducing gas bubbles into a liquid monomer or a hot polymer, allowing the bubbles to grow and stabilise, and then solidifying by cross-linking or cooling [23]

The manufacturing process and characteristics of polymeric foams are well explained in many research papers [23] and books [24]. Metal foams are well defined with 75-90% of voids in overall volume of the structure. The fabrication processes of metal foams have been studied and their mechanical responses are discussed in details [24].

Here, metal foams are commonly made by injecting a gas or mixing a foaming agent into molten metal. Normally, In general, metal foam has a higher density than polymeric foam. However, both foam materials are good in energy-absorbing applications as both can sustain large compressive strains.

2.2.2 Periodic cellular material (two dimensional core)

Two-dimensional periodic cores can be classified into two forms: prismatic and honeycomb cores. Honeycombs are made of sheets or plates that form a group of unit cells. This united structure can be placed between the skins to create a hexagonal-core sandwich panel [22]. Other shapes, such as square, triangular or circular shapes, can be used as core for honeycomb sandwich panel. Moreover, honeycombs, like prismatic cores can be rotated 90° about their horizontal axis, which can form an open channel structure on one direction and a closed-cell structure in the orthogonal direction. Better cross-flow air for a heat exchanger can be offered by these periodic channels [3].

2.2.2.1 Honeycomb core

A honeycomb core can be manufactured by many innovative ways. A thermoplastic folded honeycomb core from one single thermoplastic sheet using successive in-line operations was invented and patented by Bratfisch et al. [25]. By cutting and slotting sheets, square honeycomb and diamond cores can be assembled as illustrated in Figure 2.2. For example, Zok et al. [26] manufactured a sandwich panel by brazing the core and the face sheets of stainless steel. Slotting technique was adopted by Russell et al. [27] on various composite materials to manufacture the honeycomb cores. The slotted rectangular plates were assembled together (Figure 2.2) to obtain a

square honeycomb core. These cores were then bonded with the skins to get a sandwich structure.

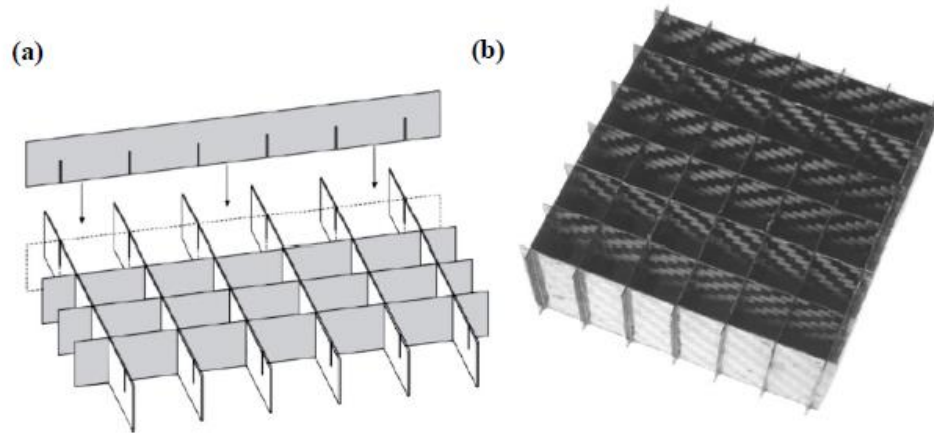


Figure 2.2 (a) Schematic diagram of square-honeycomb core [26] and (b) photograph of an assembled composite square-honeycomb core [27].

2.2.2.2 Corrugated Core

Corrugated-cores are two-dimensional periodic cores. Corrugated-cores can be classified into four geometries, i.e. hat-type or trapezium, triangular, straight, and curvilinear as reported by Buannic et al. [28], depicted in Figure 2.3. The authors then compared the properties of the four core geometries to a reference stiffened panel, to determine the pure bending characteristics of periodic plates.

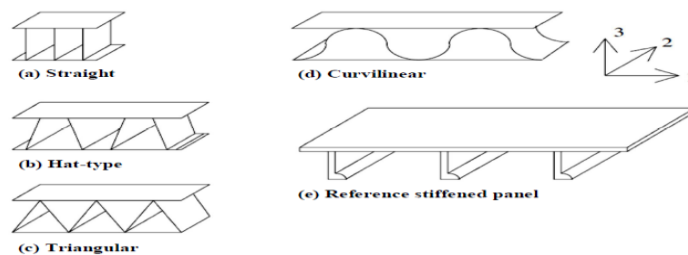


Figure 2.3 Classification of corrugated-core sandwich panels [28].

Amongst these four cores, curvilinear or sinusoidal were the most common core design in the corrugated-core sandwich panels. Particularly in the packaging industry, this type of geometry has been widely used. Nordstrand and Carlsson [29, 30] studied

the compression, buckling and shearing deformation behaviour of these five different corrugated structures. The compression and buckling response of these corrugated structures were also investigated by many researchers and scientists [31-33]. It was concluded that the corrugated structures were failed due to buckling and shearing deformation of cell walls. In order to find the effect of design measurements on the compressive strength of the structure, pre- and post-buckling responses of the panels were studied. To investigate the elastic behaviour of the corrugated plies, an analytical model was proposed by Aboura et al.[33]. Due to the flexible geometry, sinusoidal corrugated structures could be used in morphing wing structures as explained by Yokozeki et al. [34] and Ge et al. [35], Figure 2.4. Challenges to simulate these sinusoidal corrugated-core are also demonstrated in [36, 37].

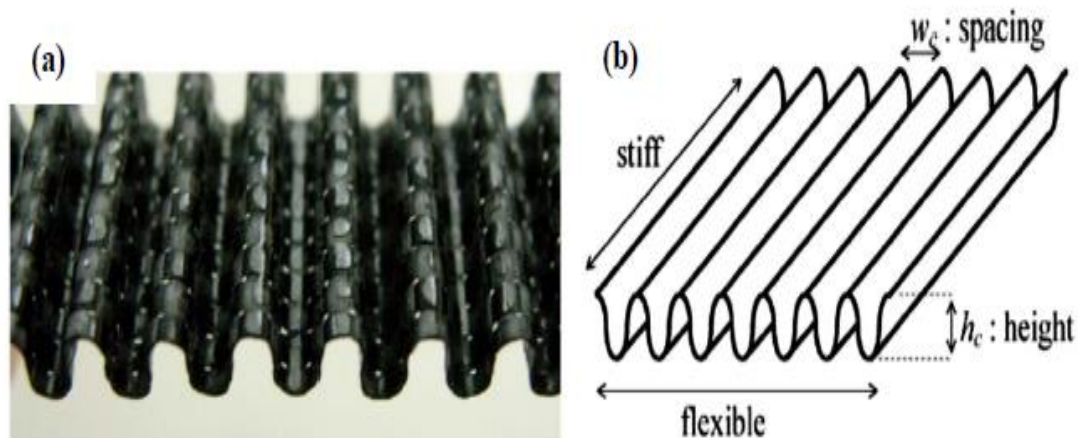


Figure 2.4 (a) Sinusoidal corrugated-core made from carbon fiber and (b) Schematic geometry of sinusoidal core for morphing wing [34].

2.2.3 Three dimensional periodic cores

2.2.3.1 Lattice core

Truss and woven textile based lattice materials are the examples of 3D open cell structures. Truss or strut-based lattices are composed of a network of interconnecting struts, which meet at nodes. Here, the use of the words 'strut' and 'truss' refers to a

rigidly-joined member as opposed to a pin-jointed member, which is used in structural mechanics. Textile-based lattice structures are also open celled structures, consisting of layers of woven metal wires that have been bonded together. These structures also offer excellent energy absorbing properties with very low density. The open cell structure renders truss-based materials suitable for multifunctional applications, such as cross-flow heat exchangers, baffle structures and low-pressure drop catalyst systems. In 2001, investment casting process was used to fabricate the tetrahedral and Kagome lattices [38]. In the advanced manufacturing process of lattice structure, a Selective Laser Melting (SLM) technique was used by Smith et al. [39] and Gümrük *et al.* [40] to manufacture the periodic metallic lattice structures. Using SLM technology, an array of stainless steel micro-lattice blocks were manufactured as shown in Figure 2.5.

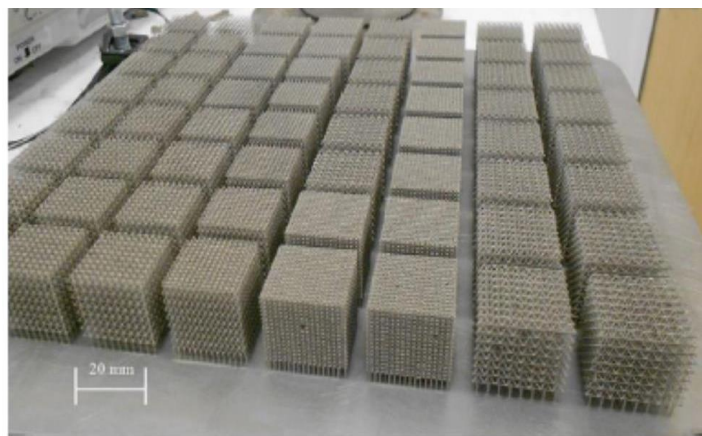


Figure 2.5 Micro-lattice blocks manufactured by SLM technology.

2.2.3.2 *Folded core*

Movchan [41] introduced the three-dimensional periodic folded core geometries. He suggested a folded core made from Nomex aramid paper. Those folded cores are promising because of the new production means [42]. The investigated folded cores are made from Nomex paper coated with epoxy resin. Folded cores are air ventilated

due to their channel-like structure, which can help to reduce the danger of deterioration, which is a big advancement for applications in the aerospace industry.

Chevron folded core was probably the first manufactured core among newly designed folded cores, as shown in Figure 2.6. In the beginning of the 20th century, the chevron folded core was manufactured. Later, the pattern was under review in University of Kazan. More recently, continuous production and a lot of new techniques have emerged. Basily and Elsayed [43], experimentally investigated the strength of chevron folded cores, and was further numerically simulated by Nguyen et al. [44] and Heimbs et al.[45]. Moreover, their transverse shear stiffness has been experimentally studied [42]. The geometric description of the chevron pattern was discussed by Lebée et [46]. It was found that the larger the shear deformation, the smaller was the residual compression stiffness. This was due to initial shear deformation, where the cell walls of the folded core were deformed against the original position.

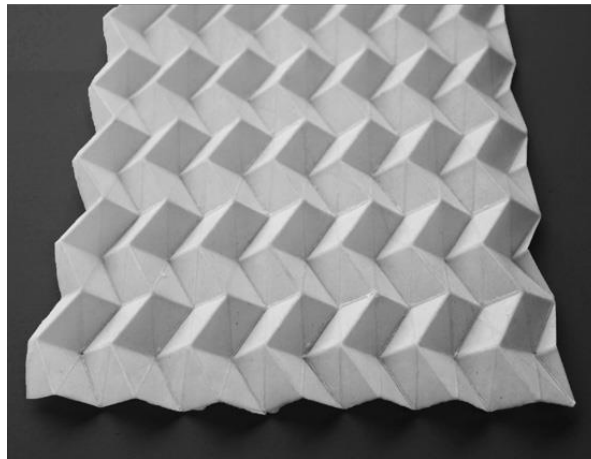


Figure 2.6 : Chevron folded paper [46]

2.2.3.3 *Egg-box core*

Amongst the variety of cellular cores existed, it is worth emphasizing a subset of the three-dimensional periodical lattices that is the egg-box structure. A schematic of this

design is shown in Figure 2.7. This new class of energy absorbing structure based on aluminium egg-box was introduced to understand the collapse mechanism of egg-box cells [16]. Experiments suggested that egg-box structures deform by either the rotation of a stationary plastic hinge or by a travelling plastic knuckle, depending upon the in-plane kinematic constraints imposed upon the egg-box. Egg-box shaped energy absorbing structures made of fabric composites were fabricated to determine the compressive characteristics and energy absorption capacity.

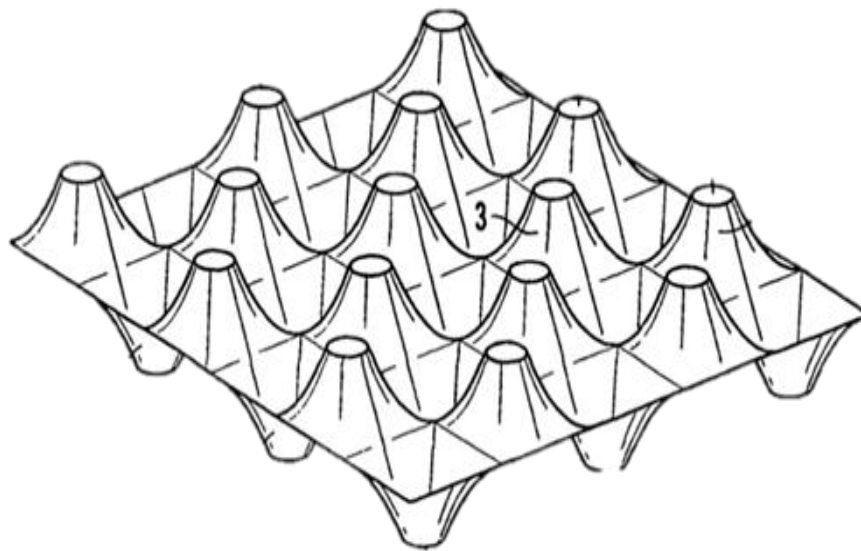


Figure 2.7 Schematic diagram of a Egg-Box core [47]

Chung et al. [48] fabricated composite egg-box structures and stated that its density, boundary conditions and geometry affected the energy absorption. Fibre reinforced composite structures were manufactured via vacuum bagging and autoclave curing. Figure 2.8 exhibits the model of the overall geometry of Chung's samples. Fibre volume fraction and fibre architecture were varied by changing the stacking sequence of the fabrics during the initial lay-up and draping. In these samples, two parameters,

namely fibre volume fraction and fibre architecture, were modified to define the amount of energy absorbed by the core.

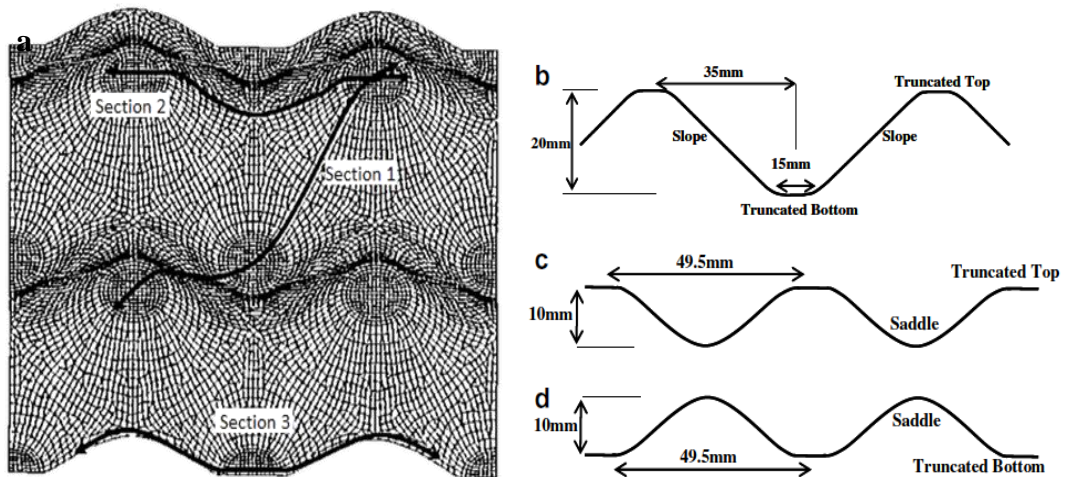


Figure 2.8 Composite egg-box and cross sectional dimensions of the core: (a) overall geometry, (b) Section 1, (c) Section 2, (d) Section 3 [48].

The production of foam filled egg-box sandwiches via autoclave curing was explained by Yoo et al. [18]. It consisted of draping the prepregs onto the lower half of a silicone rubber mould, closing with the upper half and vacuum bagging the tool with a breather fabric and a nylon film. The set-up with the core was cured in an autoclave following a specific heating cycle. Flat composite sheets were then attached to the surfaces of the core using adhesive bonding, creating a sandwich panel. Lastly, self-expanding foam with spraying gases was sprayed into the core, with its cavities completely filled. The crushing behaviour, crushing force and energy absorption of the egg box cells, which is essential for comprehensive design and subsequent improvements, were analysed.

2.3 Energy absorption and crashworthiness

A structure can be called as an ideal energy absorber if it can enhance the specific energy absorption capacity and minimise the effect of kinetic energy. High speed vehicles like motor car and passenger coach can be improved in their safety characteristics by the use of such structures in the vehicle design. A crash or shock enduring structure is the one that controls the impact forces and the safe transfer of kinetic energy by collapsing in a predictable behaviour [49]. The possibility of passenger's injury can be minimised by introducing this controlled collapse in vehicle design. The level of the crashworthiness of a system can be determined by certain factors like maximum strength, structural stiffness and energy-absorbing capacity at plateau stage.

Many safety features have been developed, including front and side airbags, seat belts and anti-lock braking systems (ABS) to minimise injuries to occupants from a collision. Other than these accessories, the front and rear bumpers, air filter, bonnet, dashboard, doors, liquid storage components and other parts of a vehicle body can be designed to absorb optimum energy absorber during collision [50]. These accessories could play a major role to make a safe journey for both pedestrians and passengers.

The energy absorption in cellular absorbers can be determined through collapse processes such as plastic yield, plastic buckling, or folding through stationary plastic hinges and travelling plastic hinges, depending on the type of the geometry [51]. The theoretical model for axial collapse of tube was first proposed by a researcher named Alexander. The mean crush force in Alexander's model is derived based on the balance of internal and external work. Later, Abramowicz adopted and Jones [52] modified this simple theoretical model into a more precise model. In some

geometrical cases the energy-absorption of the structures cause fail due to material tearing [53].

Thin-walled rectangular tubes, circular tubes, hat-section tubes (the cross section of this structure has flat-roof at the top), tapered rectangular tubes, conical shells and frusta, metallic foams, polymeric (Non-Metallic) foams [54] and cellular solids [55] are the most demanding categories of energy absorbing systems. Examples of energy-absorbing geometries are displayed in Figure 2.1. Investigations have been carried out on each structure for many years, to look at the mechanical properties of those geometries.

In the studies of energy absorbing structures, thin-walled tapered structures are new and novel among the tubical design. In early 1986, Reid et. al. [56] briefly looked at the collapse mechanisms of these structures. Based on this study, Nagel and Thambiratnam [57] carried out various tests to find the deformation nature of tapered rectangular tubes under different loading conditions. This work was further undertaken by Mirfendereski et al. [58]. The researchers concluded that tapered rectangular tubes raise the energy absorption capacity by their deformation pattern as well as minimises the possibility of initial peak stress due to their tapered shape geometry. It results in reduction of damage due to the impact load on the protected bodies [59]. In fact, it is ideal to use tapered structures as energy absorbing system under various load conditions, proposed by Reid and Reddy [60]. Hence, due to a circular cross section on tapered geometry, conical shells also fall into this category.

Deformation and the crushing pattern of thin-walled conical shell and frusta make them as the most ideal existing structures in numerous types of energy-absorbing applications like automobile, marine and aerospace designs [61]. The crush and

energy-absorbing response of these structures have been studied by many researchers, when it is subjected to various loading conditions such as compressive, axial inversion, axial splitting, lateral bending, lateral indentation, lateral flattening and impact [61-64]. The chance of buckling or global bending in a conical shell is much less than that in a circular tube, which makes this structure a better substitute [62]. In comparison, it also displays a more stable deformation pattern [65]. Efforts have been taken to determine the behaviour of closed top conical frusta in order to find a deformation pattern for egg box cellular structures, studied by Deshpande et al. [66]. They explained that the behaviour of these structures frame-ups a pattern that can be expanded into more complex structures consisting of arrangements of conical frusta. More recently, the effect of quasi-static compressive loading have studied on various stages of the collapse and crashworthiness of aluminium egg-box structure, by Nowpada et. al. [67]. A comparison with the deformation nature of tubes reveals that the drop in strength exhibited in these structures is diminished in the egg-box structures. Therefore, they have drawn an inference that to improve the crashworthiness of vehicles, the egg-box energy absorbers can play a vital role.

Johnson described the definition of crashworthiness as a measure of the ability of a structure to absorb impact energy in a controlled manner. Thereby, it ensures that vehicle can absorb the majority of the crash energy and minimises the impact experienced by occupants, thus ensuring survival of the occupants [68]. Later, Wierzbicki and Abramowicz [69] defined the structural crashworthiness as the impact performance of two objects colliding with each other. Future structures must be manufactured to ensure the crashworthiness design for safety.

Theoretically, a crashworthy design sifts a part of a load due to the collision of the vehicle's bodies. To protect the body from damage, it is necessary that the impact load value should be lower than the amount which could damage the structure. An ideal energy absorbing structure can minimise the effect of this impact that would result in damage. It is also important that the peak load value must be within a reasonable range to reduce the kinetic effects [70].

2.3.1 Geometrical characteristics of egg box as an energy absorbing module

It is a challenging task for engineers and designers to find a cost effective and efficient energy-absorbing system in vehicle parts, to guarantee an equal level of comfort to the occupants. Symmetrically interconnected cellular system can bring a solution to meet with the occupants need. These interconnected cellular systems deform constantly under compression, which in return produces a continuous force. One of such energy absorbers is the egg-box structure [71].

As the name implies, egg-box is a structure comprised of a set of flat-roofed conical cells, forming the shape given in Figure 2.9.

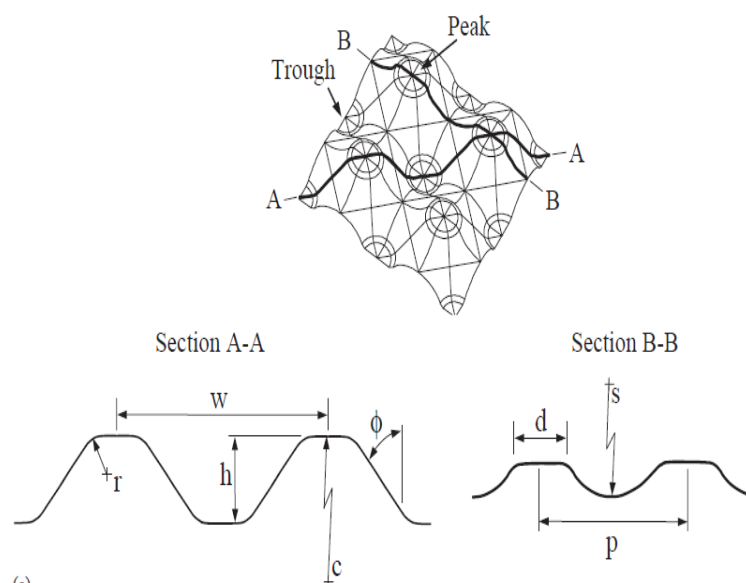


Figure 2.9 The egg box energy absorbing structure [71]

Under various impact angles, the regular flat-top structure is known for its ability to deform in a predictable manner and produce consistent results [72]. Low weight egg-box structure can be fabricated, which is based on the material consumed in its production and can be manufactured to the desired geometrical features for specific applications. It has been shown that by reducing the inter-peak distance between the adjacent cells, a higher density of cones can be achieved through the structure, which in turn increases the stiffness and stress level, that reflects into a higher energy-absorption [66].

The manufacturing cost of egg-box is very low as it can be fabricated from metallic plies by pressing it between the moulds. It can be also produced by injection moulding while using plastic materials [50]. As a result of this simple manufacturing process, it is relatively easy to mould a complexly shaped egg-box structure and adapt compressive strengths for various uses. Egg-box can be easily assembled into sandwich panel, which can offer excellent mechanical response in sandwich systems [50]. These are the most desirable features in advanced engineering and design for automobile and aerospace industries.

Along with the excellent energy absorber, additional advantages of the egg-box panels are to have an open channel throughout the length and width. This is structurally useful in allowing for wirings to pass along the length of the panel structures and air ventilated, which can help to reduce the danger of deterioration and humidity retraction.

A specific feature can be illustrated in the deformation process of the egg-box structure, which explains a suitable energy-absorbing mechanism with the collapse of the egg-box geometry under compression loading. Hinge and plastic buckling are two

important deformation mechanisms during the compression of egg-box as shown in Figure 2.10.

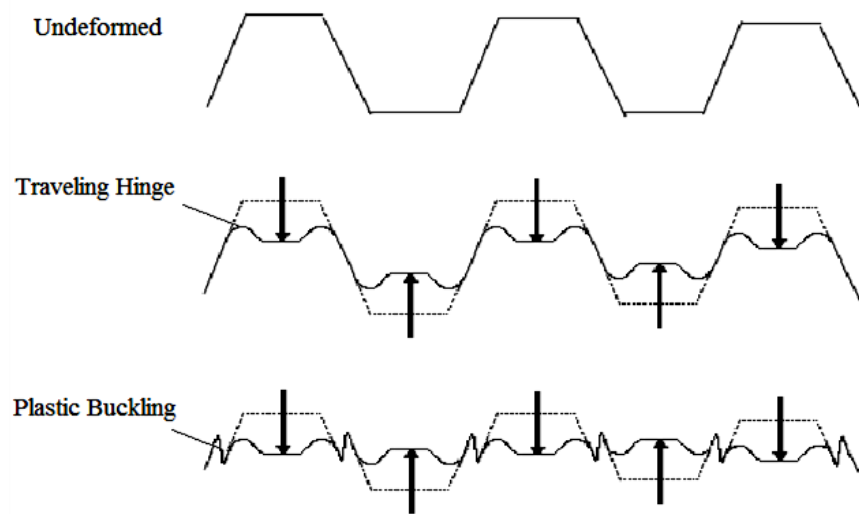


Figure 2.10 Egg box deformation procedures [72]

Uniaxial compression deformation mechanisms of these structures are very complex. To understand the different deformation modes of egg-box energy absorbing systems, different variables are considered and evaluated by mechanical engineers for specific purposes. Optimisation of these key factors can enhance the structural behaviour and efficiency of the structure that would fulfil the specific requirement of the market.

Usually, experimental testing is the main practical procedure to understand the effect of variations of geometric characteristics in the structural behaviour and its specific energy absorption capability [51, 73]. Various experimental works have also been carried-out to verify numerical simulations and analytical methods [11, 30, 66, 67, 71]. Numerous practical techniques are existed to understand the mechanical response, which can be separated into three main categories, i.e. quasi-static compression, dynamic impact and blast testing. In the next part of this chapter, the previous and current researches are to be reviewed.

2.4 Experimental Testing

In this section, mechanical response of relevant cellular structures under quasi-static, low velocity impact and blast loading are discussed to help in understanding the behaviour of energy absorbing sandwich structures.

2.4.1 Mechanical response under static compression tests

Oliveira and Wierzbicki [74] investigated the crushing of conical and spherical shells under compression loading. An analytical modelling was carried out to evaluate the behaviour of the structures. A general methodology was expressed to resolve practical problems associated with a conical and spherical shell crushing between rigid plates, and a spherical cap under external uniform pressure. A good correlation was found with some existing solutions of similar problems obtained through much lengthier calculations.

For the safety purpose of pedestrian, a quasi-static test on lightweight aluminium egg box structure was performed by Nowpada et. al. [75]. The egg-box panel structures, made up of arrays of positive and negative frusta, were investigated. To understand the collapse mechanism and the factors influencing the energy absorption, compressive tests were conducted under similar test conditions on two single frusta, one constrained in situ and the other separated from the egg-box panel exposing the free-free edges. Their load-displacement histories showed characteristics that were similar, with a rise in load to a point where they plateau at a steady state load for the entire collapse time. However the energy absorbed by the in situ constrained frustum is 80% greater than that separated from the egg-box panel with free-free edges. It is thus evident that the natural restraint due to the presence of flanges in between the

frusta has a greater influence over the energy absorption capability of the aluminum egg-box structure.

The four stages of a typical compression test were also reported by Nowpada et al. [9] on their study on the usage of egg-box panels on vehicles front. Figure 2.11 shows a schematic diagram of the specimen deformation at each stage of a unit cell of egg box. The first one is elastic deformation, which is carried until the yield point. Following on this, the deflection of the top cone starts and the load decreases as the specimen collapses. The next stage is characterised by an increase in load as a result of the formation of the plastic hinges. The final stage is known as bottoming of the plate and starts when the frustum begins to invert until the fracture of the structure.

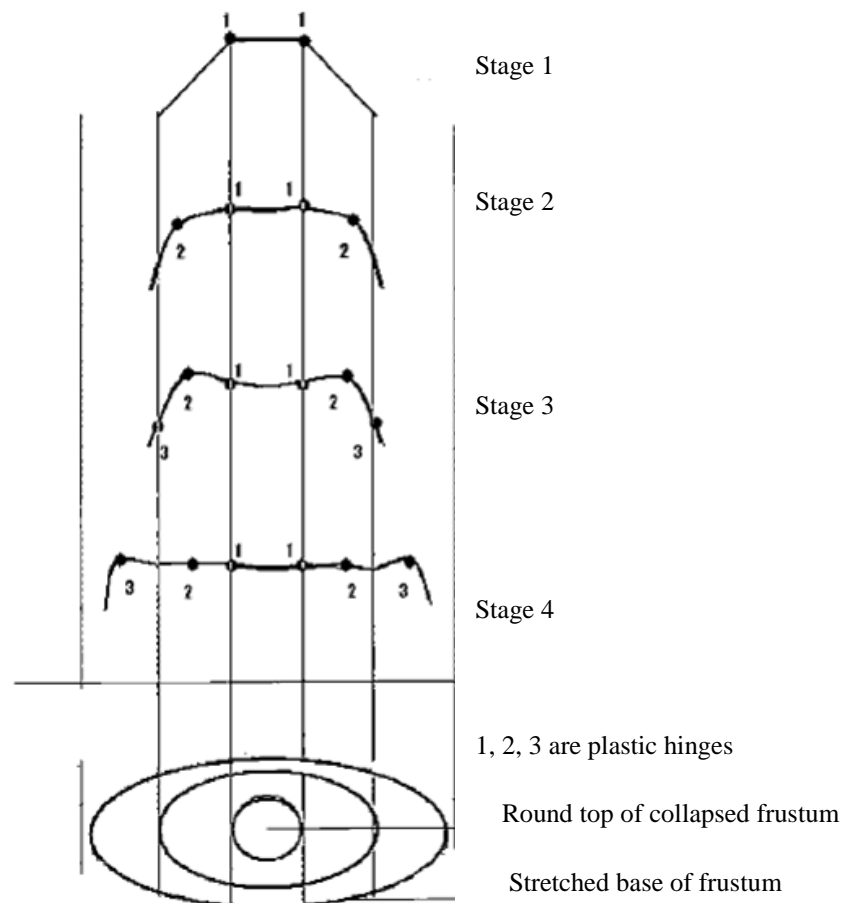


Figure 2.11 Schematic diagram of the crush stages of a unit cell of an aluminium egg-box structure under compression [9]

Static compressive tests of composite egg-box panels, whose stacking sequences and number of plies were controlled, were carried out by Chung et. al. [48] to investigate their deformation behaviour and energy absorption capacity. The nominal stress–strain traces of the specimens were compared and compression tests were interrupted at different stages to identify fracture initiation and crack growth. The specific energy absorptions of composite egg-box sandwich panels were compared with previously published work based on an aluminium egg-box panel. It was concluded from the test results that the compressive response of the composite structure is affected by the variation of stacking sequence of the fabrics and by shear deformation during initial lay-up.

Yoo et al. [18] found out that a flexible interphase between the unit cells of a structure can increase its energy absorption. His studies were then focused on the inclusion of foam in the core of a sandwich structure aiming to achieve likewise good thermal insulation properties and high load carrying capacity. Compression tests were carried on foam-filled panels, which have shown the similar stress levels to the unfilled structures. However, the filled panels behaved in a much more stable way during the plateau regime and did not show any initial stress peak. Overall, filling can optimise the energy absorption for a given stress level because the foam provides a rotational moment to the side walls, which induces premature buckling. Thus, the peak load is reduced but it does not affect the subsequent collapse response. Inclusion of foam does not affect positively the energy absorption per unit of mass, so that when the peak load is not critical, unfilled cores perform better. On the other hand, foam-filled sandwiches can be used when peak load and thermal insulation are considered.

2.4.2 Mechanical response under low velocity impact

Another relevant aspect for sandwich composites is how they respond to impact loads. A low velocity impact is commonly performed to understand the deformation in a small restricted area around the contact between specimen and impactor [76]. Besides the impact mass and velocity, impact duration is also considered during the tests. Figure 2.12 represents a diagram of an impact testing machine using a punctual impactor and the mechanism of signal transmission.

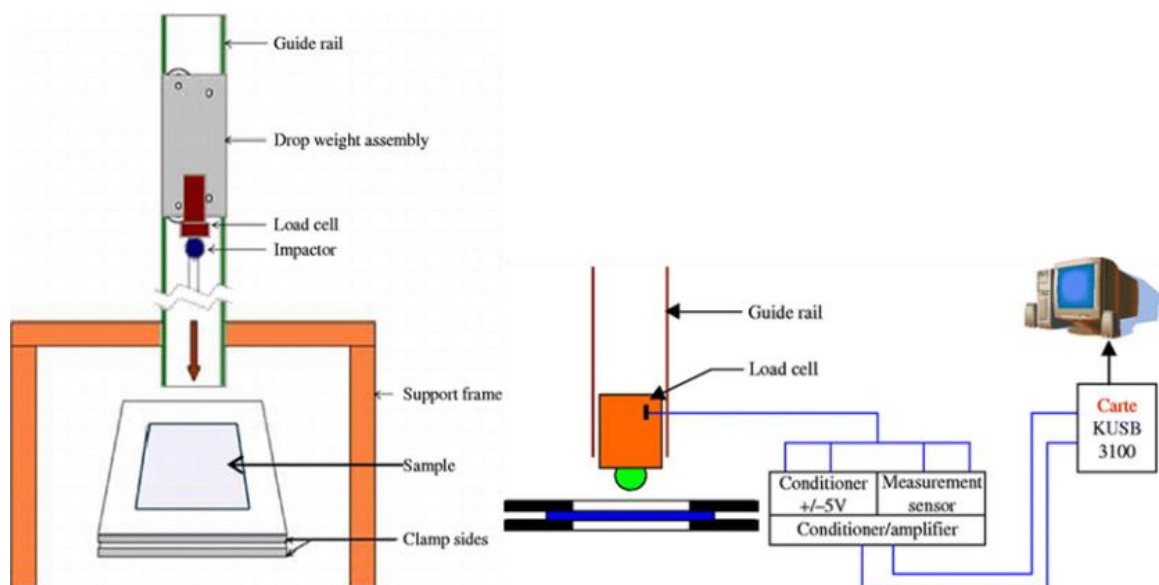


Figure 2.12 Schematic diagram of low velocity impact test rig and Instrumentation of the impact machine [77].

Shen [78] reported that the deformation of cellular materials at high strain-rates may result in an increase in the mechanical properties and energy absorption of the structure. The effect of strain-rate has been shown to depend on the material, geometry and the processing method.

The low velocity impact response of a range of foam-based sandwich structures has been investigated using an instrumented falling-weight impact tower [79]. Initially,

the rate-sensitivity of the skin and core materials was investigated through a series of flexure and indentation tests. It was shown that the flexural modulus of the skins and foam materials did not exhibit any sensitivity to crosshead displacement rate. The tests on the sandwich structures resulted in a number of different failure modes. Here, shear fracture and buckling failure were found on foam based sandwich structures.

The low velocity impact test was performed and explained by Cartié [80], in order to analyse the extension of fibre and resin properties, on the panel characteristics. According to this study, the impact response for composites can be generally described by an initial rise in load followed by a sudden drop that leads to rest load. Considering the force vs. displacement traces, the impact failure process was separated into initiation of delamination and propagation of the damage. The main energy absorption mechanism was associated with the delamination and fibre breaking.

The effects of varying the properties of the core of sandwich structures on low velocity impact response were studied by Akay and Hanna [81]. They examine the impact performance of sandwich panels based on carbon/epoxy skin and either on aramid/phenolic honeycomb or a PMI foam core. They found that the foam core offered higher energy absorption than the aramid/phenolic honeycomb. They suggested that the core provides considerable support to the facesheet and improves the impact resistance and reduces crack propagation in the skin.

Energy absorption in an aluminium foam and PVC foam sandwich structures was investigated by Compston et.al. [82] using a double pendulum impact tester. The energy absorption of each structure was similar, but the significant difference in damage mode was observed. Damage in polymer foam was localised and

characterised by matrix cracking and core indentation at low energies. In contrast, the aluminium foam core samples experienced some foam cell crushing at all impact energies and minor composite skin buckling damage at the higher energies.

The effect of varying the core density following low velocity impact was studied by Caprino and Teti [83]. Sandwich structures with three densities of PVC foam core and thin glass facings were examined. They found that high density foam cores offer higher local rigidities, leading to an increase in maximum contact force. Similar results were reported by Zhou et. Al. [84] following quasi-static loading on honeycomb sandwich structures. This behaviour highlighted the potential advantage of stronger cores in protecting the facings against impact damage.

2.4.3 Mechanical response under blast loading

As cellular structures are widely used for blast protection [85], therefore the response of these structures under blast and shock loading is also an interesting field of research.

McShane et al. [86] measured the dynamic response of monolithic and sandwich plates comprising of a steel pyramidal or square honeycomb cores under blast load. The resistance to shock loading was quantified by the permanent transverse deflection at the mid-span of the plates. It was noticed that the sandwich panels outperformed the monolithic panels with an equal mass and that the honeycomb panels had a higher shock resistance compared to the pyramidal core plates at a very high strain rate.

Hanssen et al. [87] reported the blast response of aluminium foam panels when used as a cladding type of structure. It was observed that aluminium foam with metal face sheet was effective under blast loading. The results showed that the energy and impulse transferred to the ballistic pendulum were rapidly increased by inclusion of a

face sheet to the foam panel. It is believed that due to the deformation of face sheet in to a concave shape, the overall energy transfer was controlled rather than the deformation of the core material.

Jacob et al. [88] investigated the effect of stand-off distance and charge mass on the blast response of perfectly clamped circular mild steel plates, of radius 53 mm, subjected to a very high strain rate travelling along tubular structures. It is illustrated in Figure 2.13 that the blast impulse was generated by using a plastic explosive mounted onto the end of mild steel tubes. The stand-off distance can varied, from 13 to 300 mm by placing different tube lengths. Based on the stand-off distance between the explosive charge and the plate, various load regimes were observed. At stand-off distances less than the plate radius (13–40 mm), the blast load was considered to be localized. The loading was considered uniformly distributed over the entire plate area when the stand-off distances is greater than the plate radius (100–300 mm).

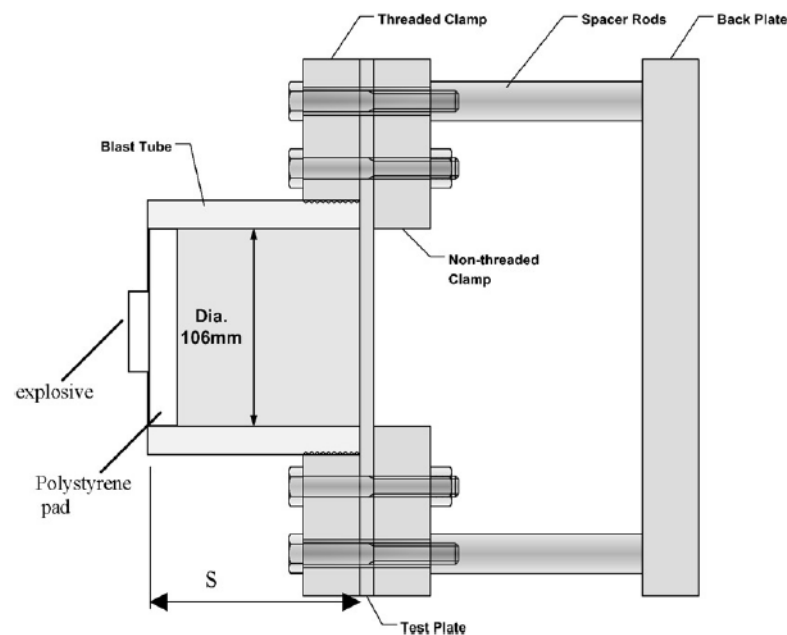


Figure 2.13 Schematic of the experimental rig used for blast test [88].

The effect of core density and cover plate thickness of Cymat aluminium foam cladding panels under blast loading was examined by Langdon et al. [89]. Steel cover plate thicknesses of 2 and 4 mm and core densities of 10, 15 and 20% were tested. The cover plate of 2mm thickness had a significant effect on the panel response with various levels of crush across the section with significant permanent deformation. The cover plate with the thickness of 4 mm has shown more rigidity leading the core to crush uniformly. The influence of adding face-sheets to the foam core was also investigated and noticed that the level of fracture increased in the core.

Ashby et al. [90] explored the detailed design of sandwich panels for blast protection. The author noted that it is beneficial to fix a thin or thick face-sheet to the front of the energy absorber as the blast impulse imparts a momentum to the face-plate accelerating it to a certain velocity with an associated kinetic energy. Thick face-sheet results a lower velocity and therefore a lower kinetic energy for the absorber to dissipate.

2.5 Finite element modelling and simulation

The background of the finite element method, the modelling of sandwich structures and other factors involved in static and dynamic FE modelling are explained in this section.

2.5.1 Background of the finite element method

The finite element (FE) analysis is a significant tool for the world of engineering and structural calculations. It can help in studying and deep understanding of mechanical behaviour of various structures and designs. In general, most of the engineering geometries tend to display complicated deformation characteristics which cannot be precisely modelled using the traditional analytical methods. With the correct use of

FE packages, engineers can model the accurate response of the structure under quasi-static or dynamic compression load [91]. In the initial design of energy absorbing structures such as body parts of vehicles, this technique becomes extremely valuable. Finite element analysis can be a time-saving process with accuracy and inexpensive repeatability.

For technical analysis, the use of the Finite Element Method (FEM) as a computer-aided engineering (CAE) tool has become common in recent years. Abaqus, LS-Dyna, ANSYS, CosmosM, ALGOR, Nastran, Hypermesh etc. are the examples of numerous commercial FE packages available.

All researchers in automotive and aviation industries are the end-users of commercially available FE packages as the FEM technique is already well established. Though the finite element techniques have been well established, it is important to grab the basic knowledge of the FE software in order to deliver the optimum solutions. Nowadays, the end-users are capable to produce detailed visualisations in CAE including stresses, strains and deformations of structural components. Hence, before the production of the components, a high level of confidence can be obtained.

2.5.2 Numerical simulation and analysis

The torsion deformation and bending collapse of foam and foam filling structures were studied by Chen et al. [92] and Reyes et al. [93] to determine the bending strength of the panel. It was found that bending strength of foam filled panel was increased. An FE simulation of the axial compression of metallic thin-walled square frusta was performed by Mamalis et al. [94]. The FE code LS-DYNA has been widely applied by researchers and designers. Several researcher works have been

reported on energy absorbing applications where LS–DYNA was used and outcomes were verified against experimental results. The investigation on the vehicular impact on a portable concrete barrier was undertaken by Ulker et al [95], where a crash test is simulated by the help of LS–DYNA with the aim to update a set of charts for assessing the barrier displacement and the related variables before to entering the phase of design [95].

Olabi et al. [96] investigated the energy absorbing behaviour of a tube using ANSYS. The quasi–static lateral crushing of tested systems was modelled by implicit version of ANSYS. Morris et al. [97] also employed the implicit ANSYS to analyse the energy absorption of tube with various constraints and indenters. ANSYS was also used to investigate the crashworthiness of cylindrical columns made of honeycomb sandwiches, under axial crushing loads at Dalian University of Technology in China [98]. They concluded that the dynamic performances of these sandwich structures have been significantly improved.

The choice of the suitable FE package, constitutive models and failure criteria are significantly important. It is based on the geometry and material characteristics of the structure as well as the output data needed from simulation. Karagiozova et al. [99, 100] employed the explicit version of ABAQUS for their simulations. Due to the complexity of the structure, the experimental criteria were replicated by the FE analysis to produce two or three- dimensional axisymmetric modelling, representing the geometrical and material attributes of the structure. Aljawi et al. [101] employed the two-dimensional axisymmetric simulation method to model the inversion of plastic tubes through ABAQUS software. Good agreement was obtained between the

experimental results and their FE predictions. This two-dimensional method helps to save the computation time.

Tilbrook et al. [102] used FE Aaqus/Explicit to predict the quasi-static and dynamic performance of the stainless steel corrugated sandwich structures. A 2-D finite element modelling was created with the same geometry and test conditions for which it has been being experimented. A four-noded plane strain quadrilateral element was used in meshing. A perfect bonding was given between the core material and skins of corrugated sandwich structure. A hard contact was also employed between the contacting surfaces. A good agreement was remarked between the predicted numerical response of the quasi-static model and experimental results through the crushing process. A high level of buckling response was produced in the corrugated panels, when it was modelled for dynamic impact. Research was focused on determining the crushing behaviour of corrugated panels under dynamic compression at 50 and 100 m/s. In conclusion they found that the tested specimens were able to show the dynamic strengthening mechanism of the corrugated sandwich structure.

A three-dimensional metal corrugated-core sandwich structure under a low impact with heavy mass was simulated by Qin et al. [103]. Corrugated-cores were meshed with reduced integration of eight-noded linear brick element to simulate the core and face sheets in Abaqus/Explicit. To save the simulation time it was enough to analyse the half length of corrugation as the corrugated beam is symmetric. The structural behaviour was modelled using elastic and plastic strain hardening properties. It was concluded from their research that the dynamic behaviour of the sandwich core outperforms monolithic solid plate of similar mass.

Vaziri et al. [104] developed models for clamped-end metal sandwich plates with two different sandwich cores (folded cores and square honeycomb) subjected to quasi-static and impulsive loading, using Abaqus/Explicit. The buckling resistance of the core was increased due to support of foam to the cell walls. It was one of the main achievements of the investigation. Models of specimens were created using brick elements to all components including core cell wall, polymeric foams and face sheets. Flow theory based on the von-Mises yield surface and isotropic hardening was employed in the simulations. All the simulations were executed using the explicit time integration (Abaqus/Explicit), both for quasi-static and dynamic loads.

In the models of foam-filled cores, the displacement of the steel core and polymeric foam coincide at nodal points on shared interfaces has been briefly discussed by Vaziri et al. [104]. When implicit version (Abaqus/Standard) was used to analyse the deformation, the problems appeared with convergence difficulty, due to the complexity of the geometry and interaction between different material characteristics within the sandwich panel, resulting in a large number of iterations. Such analyses are expensive in Abaqus/Standard because each iteration requires a large set of linear equations to be solved. Abaqus/Explicit determines the solution without iterating by explicitly advancing the kinematic state from the previous increment. Therefore, foam-filled and unfilled cores were simulated using Abaqus/Explicit. It was found from the quasi-static simulation that the crushing resistance of the core structure was enhanced by contributing a support from polymeric foam.

The plastic collapse response of aluminium egg-box panels subjected to compression loading was measured and modelled [71]. It was found that the compressive strength and specific energy absorption are varied with different level of constraints. The

collapse mechanism consists of plastic buckling or by a travelling plastic knuckle. The drop weight impact tests were carried-out at velocities of up to 6 m/s, and an enhancement in peak load with impact velocity was clearly noticed. A 3D finite element shell model was utilised in order to validate the modelling. The finite element models confirm these mechanical improvements due to the strain-rate effect on aluminium sheet.

Quasi-static compression behaviour of aluminium egg-box structure at various stages of the collapse was studied by Nowpada et al. [9]. They observed that after an initial peak the load dropped gradually until the densification. Hence they concluded that to improve the crashworthiness of vehicles, the egg-box energy absorbers could play a vital role. Later, numerical methods were developed by the research group to investigate the deformation pattern of the egg-box geometry under quasi-static loading. HYPERMESH and LS-DYNA were successfully employed to validate the FE models against the experimental results. Comparing the energy absorption capacity of egg-box at different boundary conditions, it was concluded that the connectivity with surrounding cells provide a restraint within the egg-box panel which in turn enhance its energy absorption characteristics [75].

2.6 Modification from egg box to contour core structure for optimum energy absorption

Many attempts have been made by researchers and scientists to enhance the quality of design and manufacturing methods in order to find the optimal structures[105]. With the help of updated and established software packages, a wide range of possibilities can be tested and the goals can be rapidly obtained [106].

Understanding of deformational behaviour of a structure is essential before to design an optimal energy absorber. Harte et al. [107] explained that the force–displacement trace of an ideal energy absorber exhibits a smooth plateau at its plastic region. Structures such as tubes, shells and cellular solids satisfy this deformation pattern to different extents.

Gupta [108] also examined the energy absorption and deformation pattern of circular tubes under quasi static and dynamic impact loading, both experimentally and numerically. To understand the effect of geometrical parameters on energy absorption capacity, the wall thickness and diameter of tube were varied. It was found that the energy-absorption of circular tubes in dynamic tests is around 1.5 – 12% better than in quasi–static tests, whereas the initial peak load is 15 – 40 % higher than quasi–static one. Moreover, a significant conclusion was drawn that the energy absorption and crushing load capacity increase with increasing thickness and diameter values.

Nagel and Thambiratnam [57] stated that the tapered rectangular tube is as an ideal energy-absorbing structure in dynamic applications where combination of axial and oblique loads are present. The study draw an inference that below a defined limit of critical load angle, the energy absorption capacity of a tapered rectangular tube decreases with the rising in the load angle. Liu [109] also verified this approach.

Hou et al. [110] investigated the single and multi-objective optimisation of energy absorbers in general and thin-walled rectangular tubes specifically. The research group made a most effective use of the cross-sectional dimensions of multi-cell tubes to magnify their energy-absorbing behaviours. Their investigations marked that improvements implied to each objective would amplify the overall performance of the system to a certain extent, while at the same time it affects the other objectives

adversely. Research work was focused to develop an algorithm to achieve the most appropriate parameter to minimise the peak force and maximise the energy absorption. An inference is drawn by the research group that the former goal can be obtained by adding more cross-sectional cells.

Spagnoli and Chryssanthopoulos [111] defined a relationship between geometrical and material features and the critical buckling load of conical shells in a form of an equation, to visualise the effect of these features on the performance of the structure. Series of numerical modelling and experimental work were carried-out by many engineers and scientists, which added to explain the behaviours of an ideal conical shell [61, 62, 65, 108].

Although the egg-box cellular solids are appreciable energy-absorbing structures, a limited research work has been reported to investigate their development and mechanical performance .

Yoo et al. [18] conducted a set of quasi-static compression tests, at different materials and loading conditions, on foam-filled composite egg-box panels. A conclusion was drawn that the composite egg-box panels filled with foam can offer outstanding performance with a stable collapse mechanism, resembling an excellent energy absorbing system.

However, a very limited work is presented on the effect of geometrical adjustment variation of loading rate and material alteration, on the performance of egg box sandwich panels. Akisania and Fleck [112] defined that the egg-box is a square array of conical frusta. Gupta [61], mentioned that the alterations of geometrical parameters significantly affect the overall performance of the flat-roofed cones. Therefore, it is

concluded that an egg-box structure can be geometrically designed and modified to achieve an optimum solution of energy-absorbing structure.

Based on the above discussion, the current project also attempts to geometrically modify the egg-box structure, which is named as contoured structure, to enhance the mechanical performance and energy absorption of the designed geometries.

Summary of the chapter

This chapter has presented a review of relevant studies from past and current research work on sandwich structures subjected to quasi-static and dynamic compression loading. The review includes a brief explanation of the classification of cellular materials, such as foams and periodic cores. Here, a review of the mechanical response of related core structures under the quasi-static and dynamic loading is presented. Based on the literature, a periodic core structure using composite material offered good mechanical properties to be used as energy-absorbing engineering applications. Failure mode of the periodic structure mainly associated with buckling, delamination and compressive failure. A number of factor on their static and dynamic properties have been observed such as the material effect, cell wall thickness, angle of corrugation, relative density, strain-rate. Finally, procedures and techniques for modelling the response of honeycomb, corrugated and egg-box sandwich structures using commercially-available FE codes have been reviewed. The use of imperfection in a model can help to predict the structural response which is comparable to experimental work.

To date, very limited research works have been found on contoured core structures. This confirms the main contribution of the current research work to investigate a cost effective manufacturing process with modifications on contoured cores and evaluation of the mechanical properties of composite contoured-core sandwich structures.

Chapter 3 Experimental work

3.1 Introduction

This chapter focuses on the design of the core and experimental procedures used in this study to investigate the mechanical properties of the different types of materials and structures studied here. The methods used in this study include quasi-static compression, low velocity impact and uniform blast loading tests. All tests were conducted on structures based on a glass fibre reinforced plastic (GFRP) and a carbon fibre reinforced plastic (CFRP). Initial tests were carried out to investigate the influence of the number of unit cells on the fracture properties of the sandwich structure. Following this, tests were conducted on contoured parts with increasing cell wall thicknesses, at static and low velocity impact loading. The study also investigates the influence of filling the contoured-core structures with polyurethane foam core in order to increase their energy absorption capability. In addition, blast tests were undertaken on the contoured core materials subjected to very high strain rates. An overview of the materials and fabrication procedures of contour cores used in this project is also given in this chapter.

3.2 Surface design and mould machining

Initially, aluminium moulds shown in Figure 3.1 (a) were used to manufacture a series of flat-roof contoured cores. The cross section geometry of this contoured core mould is shown in Figure 3.1(b). The design of flat-roof contoured panels is based on the same geometry described as egg-box panel by Nowpada et al. [67] and Chung et al. [48].

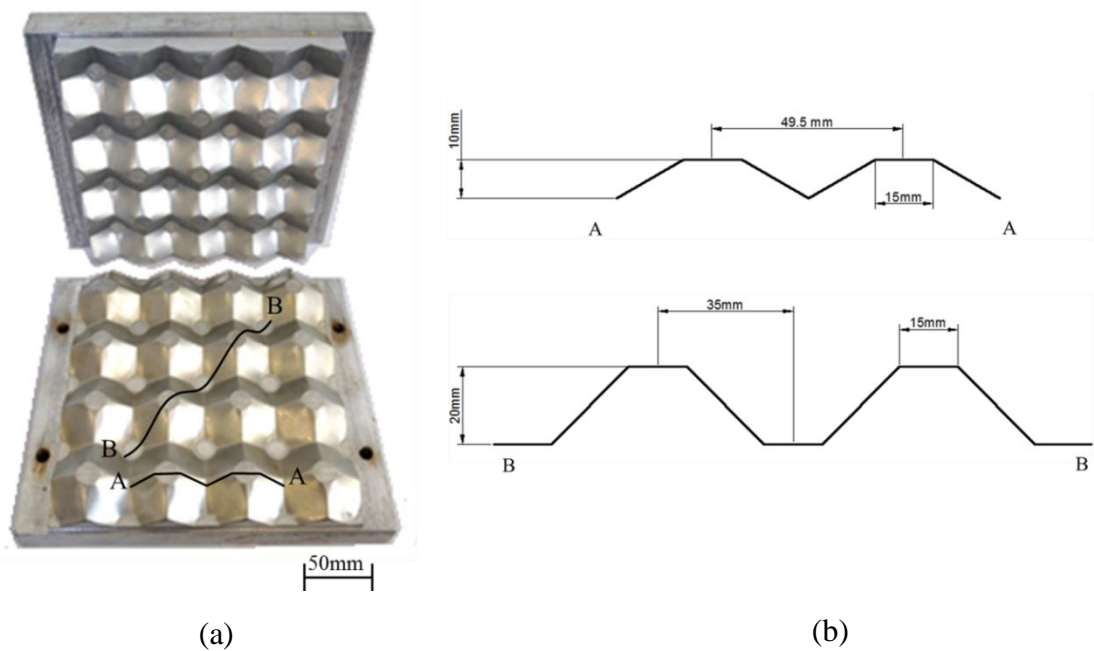


Figure 3.1. Photographs of the (a) aluminium flat-roof contoured moulds (egg box mould) (b) cross section of the geometry.

Chung et al [48] observed that initial cracking in egg-box (flat-roof contoured) panels occurred at the circular perimeters of the upper and lower surfaces that are in contact with the plates/skins, as a result of local stress concentrations. In order to avoid such regions of weakness and to improve energy absorption, an asymmetrical design was introduced by including a spherical dome. This is to reduce the inter-peak distance, cell diameter and an asymmetry between the top and the bottom dome to enhance the mechanical properties of the contoured core. This is to enhance the stiffness of the newly designed contoured core. The contoured mould was designed using the commercial CAD/CAM software and manufactured to a high precision using a computer-controlled numerical milling machine (CNC), which is composed of following steps:

- (1) A part model design by scoping the design parameters of the structure.

- (2) Create a part model Transfer the part model to triangulate surfaces in ProToolmaker (CAM) to create the CNC programme in G codes.
- (3) Set the raw materials in Haas CNC milling machine and manufacture the desired mould.

3.2.1 A part model design by scoping the design parameters of the structure

The proposed design is a combination of two different sectional profiles which is presented in Figure 3.2. The detailed design of the cell is displayed in Figure 3.3.

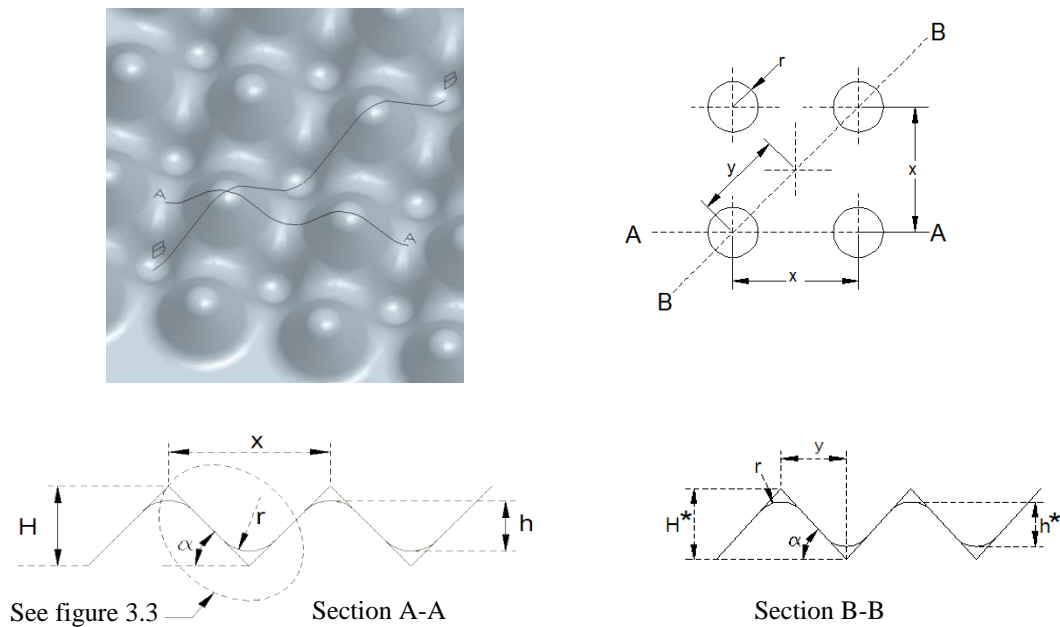


Figure 3.2 Plan view and section Geometry of contoured profile.

Section A-A of the spherical contour core design

In Figure 3.2, r refers to the radius of the curve, which is 4 mm for the proposed design, α is the base angle of the dome, which is 50° , h is the height of the contoured section.

As shown in Figure 3.3, the radius of the curvature can be calculated as:

$$r = q + s \quad (3.1)$$

where

$$q = r \cos \alpha$$

By substitution the value of q in equation (3.1), there is

$$s = r(1 - \cos \alpha) \quad (3.2)$$

The actual height h can be found from:

$$h = H - 2l \quad (3.3)$$

where

$$l = p \tan \alpha - s$$

$$p = r \sin \alpha$$

Therefore,

$$l = r \sin \alpha \tan \alpha - r(1 - \cos \alpha)$$

$$l = r \left(\frac{\sin^2 \alpha}{\cos \alpha} + \frac{\cos^2 \alpha}{\cos \alpha} - 1 \right)$$

$$l = r \left(\frac{1}{\cos \alpha} - 1 \right) \quad (3.4)$$

By substituting the value of $l = r \left(\frac{1}{\cos \alpha} - 1 \right)$ in Equation (3.3), the relation between the effective and actual heights can be described as:

$$h = H + 2r \left(1 - \frac{1}{\cos \alpha} \right) \quad (3.5)$$

Finally, by substituting the value of $H = \frac{x}{2} \tan \alpha$ Equation (3.5) in the actual height can be defined as:

$$h = x \frac{\tan \alpha}{2} + 2r \left(1 - \frac{1}{\cos \alpha} \right) \quad (3.6)$$

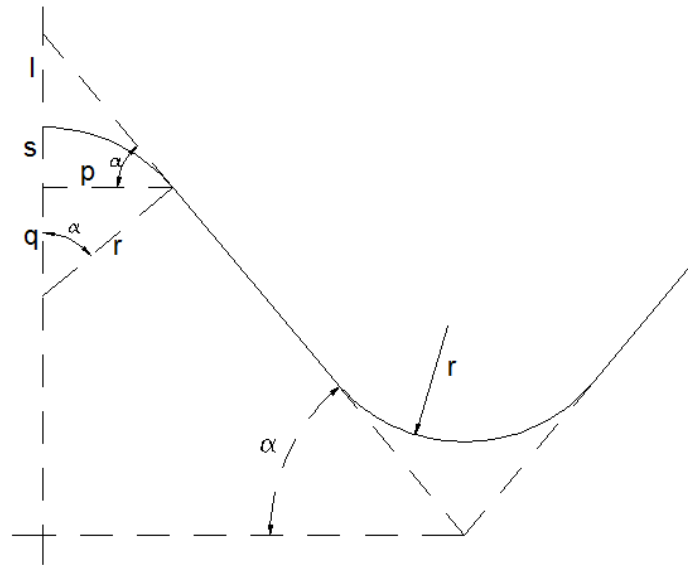


Figure 3.3 detail design of the cell.

Section B-B of the spherical contour core design

The radius and slope of the cell is same as in Section A-A. But the effective and actual heights are H^* and h^* respectively.

An important measure of the geometry can be calculated as:

$$y = \frac{x}{\sqrt{2}} \quad (3.7)$$

The effective height H^* can be defined as:

$$H^* = y \tan \alpha \quad (3.8)$$

The actual height h^* in section B-B, can be found as:

$$h^* = H^* - 2l \quad (3.9)$$

By substituting the value of l and H^* in equation (3.8), the actual height can be defined as:

$$h^* = x \frac{\tan \alpha}{\sqrt{2}} + 2r \left(1 - \frac{1}{\cos \alpha} \right) \quad (3.10)$$

3.2.2 Transfer the part model to triangulate surfaces in ProToolmaker(CAM) to create the CNC programme in G codes

In this section, the created part model was converted to IGES format and opened in ProToolmaker in order to create the manufacturing programme. ProToolmaker is a virtual manufacturing software, which could simulate and modify the manufacturing process in a digital environment. When the file was loaded in ProToolmaker, a graphics window was opened and started to triangulate the surfaces for viewing. Triangulation converts the geometric surfaces into triangles. These triangles were used to both, display on the screen and for the machining process. Initially a roughing

program was created to remove the bulk waste material from the work-piece with a toroidal carbide cutter, had 6 mm diameter and 1mm corner radius was used in CNC machining. Cutting speed and feed rate used for this operation were 130 m/min and 2 mm/rev respectively. A depth cut of 1 mm was used in each passes in z direction. In this stage final finishing was left, as shown in Figure 3.4.

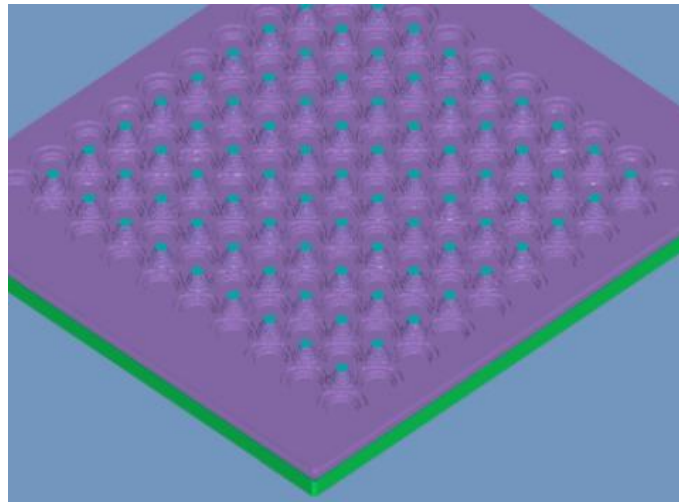


Figure 3.4 Material left for finishing is 0.5mm in x, y and z directions.

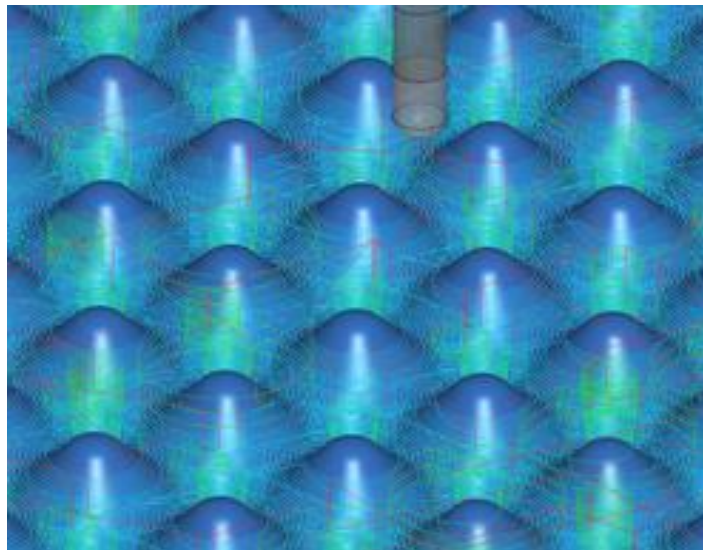


Figure 3.5 Milling cutter on smooth concave profile.

To get the final smooth profile as shown in Figure 3.5, a carbide ball end milling cutter with two cutting edges was used with a cutting speed of 150 m/min, a feed per tooth of 0.05 mm and depth cut of 0.1mm. The small concave radius of 4 mm was produced on final profile by using ball end mill cutter of 3 mm radius.

3.2.3 Set the raw materials in Haas CNC milling machine and manufacture the desired mould

A three axis Haas CNC milling machine was used to manufacture the mould. A milling machine is a machine tool that removes metal from work piece by feed against a rotating multipoint cutter. In the CNC system, operating instructions were given to the machine as G-codes. The work piece was clamped to the machine bed which can move horizontally in X and Y axis. The milling tool can move in Z axis which is perpendicular to the horizontal plane.

Initially, the surface roughing operation was done by toroid end-mill tool. The toroid end-mill has two cutting edges with a radius of 1mm, each cutting edge almost overlap at the centre line of the cutter. This design eliminates the unfavorable cutting action, where the cutting speed goes down to zero. Cutting speed and feed rate used for this operation were 130 m/min and 0.2 mm/rev respectively. A depth cut of 1 mm was used for the roughing operation.

A ball nose end-mill was used for the surface finishing operation. Ball nose end-mill has a semisphere at the tool end are ideal for machining three dimensional contoured shapes or work pieces with complex surfaces. The stepover value (along with the tool size) will determine whether the model has a smooth finish, or tooling marks are visible. Stepover is a displacement value, which moves over between subsequent

passes. Models with a smaller stepover take longer to cut. A ball nose end mill cutter with 6 mm diameter and 0.1mm stepover were used to finish the mould. The used Cutting speed and feed for this operation were 150m/min and .05mm/rev respectively.

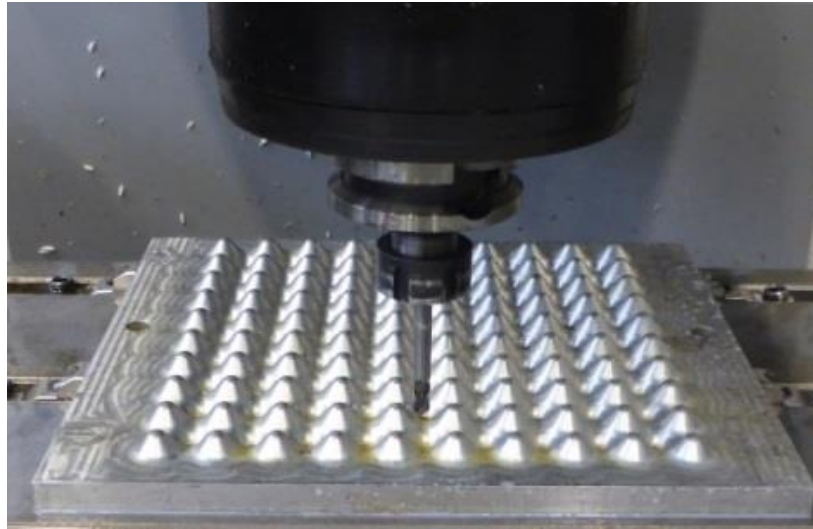


Figure 3.6 Milling cutter and work piece in Haas CNC milling machine

Finally, the spherical roof contoured core mould was achieved after CNC milling process as shown in Figure 3.7.



Figure 3.7 Spherical roof countoured mould.

The current design of the mould lacks alignment guide for a closing of the top and bottom pieces of the mould during moulding and spacer to control the desired thickness of contoured cores. Because of these, there might be a slight variation of the laminate thickness of contoured cores.

3.3 Composite materials used in present work

The glass fibre reinforced plastic (GFRP) used here was supplied by Gurit AG (Stesapreg EP127-44-40). Note that the density of a laminated GFRP is 1750 kg/m^3 . Prior to manufacture, the woven prepreg (four harness satin or Crowfoot) was cut to dimensions of 240 mm x 240 mm and then layed up, to give the required thickness. A woven carbon fibre reinforced plastic (CFRP), supplied by Gurit AG (EP121-C15-53), was also used in the study. Note that density of a laminated CFRP is 1390 kg/m^3 . During the manufacturing process, the plain woven prepreg was cut into dimensions 240 mm x 240 mm.

3.4 Specimen Preparation

3.4.1 Fabrication of the contoured core

A precise fabrication procedure was followed to control the quality of the contoured-core specimens. A roll of composite prepreg was taken out from the freezer and then placed on a clean flat surface as shown in Figure 3.8. The prepreg was cut according to 240 mm x 240 mm in warp and weft directions, respectively. Both GFRP and CFRP were used to manufacture the core parts. Details of these prepreges are given in Table 3.1.

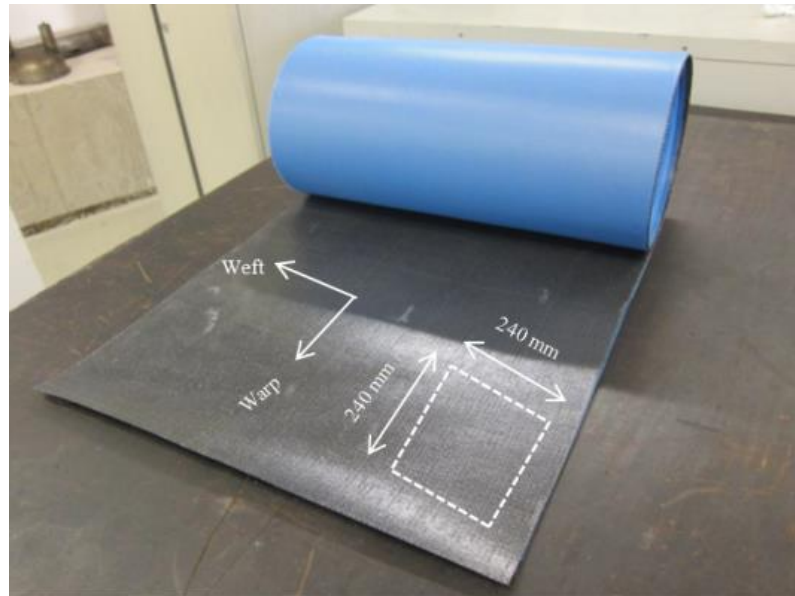


Figure 3.8 A roll of composite prepreg in the as-received condition before cutting to a size of 240 mm x240 mm.

Table 3.1. Details of the raw materials Glass Fibre and Carbon Fibre Reinforced.

Prepreg	GFRP	CFRP
Resin type	Thermoset Triazine resin	Epoxy
Resin content (% wt)	40.0 +/- 3	53.0 +/- 3
Fibre Material	E-Glass	3k HTA
Weave Style	Four Harness Satin	Plain
Laminate Density (kg/m ³)	1750	1390
Thickness of one ply cured (mm)	0.1	0.25
Curing temperature (degree centigrate)	145	120
Dwell time (Min)	90	90

The preparation of the core began with prepreg films, which were cut and placed between the upper and lower aluminium moulds. The prepreg plies were then stacked by maintaining the same fibre orientation. In this study, the GFRP cores were manufactured by stacking 5, 10 and 15 prepreg sheets in the mould, the thicknesses of the resulting cores were $0.5(\pm 0.05)$, $1.0(\pm 0.06)$ and $1.5(\pm 0.08)$ mm. CFRP cores having similar thicknesses were produced by stacking 2, 4 and 6 prepreg sheets in the mould.

Before covering the stacks by putting in-between the moulds, an aerosol releasing agent (CILRelease 1711E, supplied by Cilchem) was sprayed on both sides of the mould ensuring easy demoulding at the end of the curing cycle. The aluminium mould, shown in Figures 3.1 and 3.7, was then placed in a hot press machine. A thermocouple was also positioned to measure the temperature of the system accurately. Figure 3.9 shows the Meyer hot press machine arranged with the thermocouple, used for manufacturing the test specimens.



Figure 3.9 Photograph of the Meyer hot press machine.

The processing cycle for the prepreg curing is defined according to the manufacturer's specifications for the curing temperature (T_c) and dwell time (t), as shown in Figure 3.10. Once the thermocouple reached the required temperature, pressure was gradually increased to approximately 3.5 bar. When the temperature increased up to 145°C for GFRP or 120°C for CFRP, the chronometer was set to specify 1 hour and 30 minutes for the curing process. By the end of the curing time the production was finished, so the pressing machine was turned off. After it was cooled down, the plattens were opened and the product was removed as shown in **Figure 3.11**.

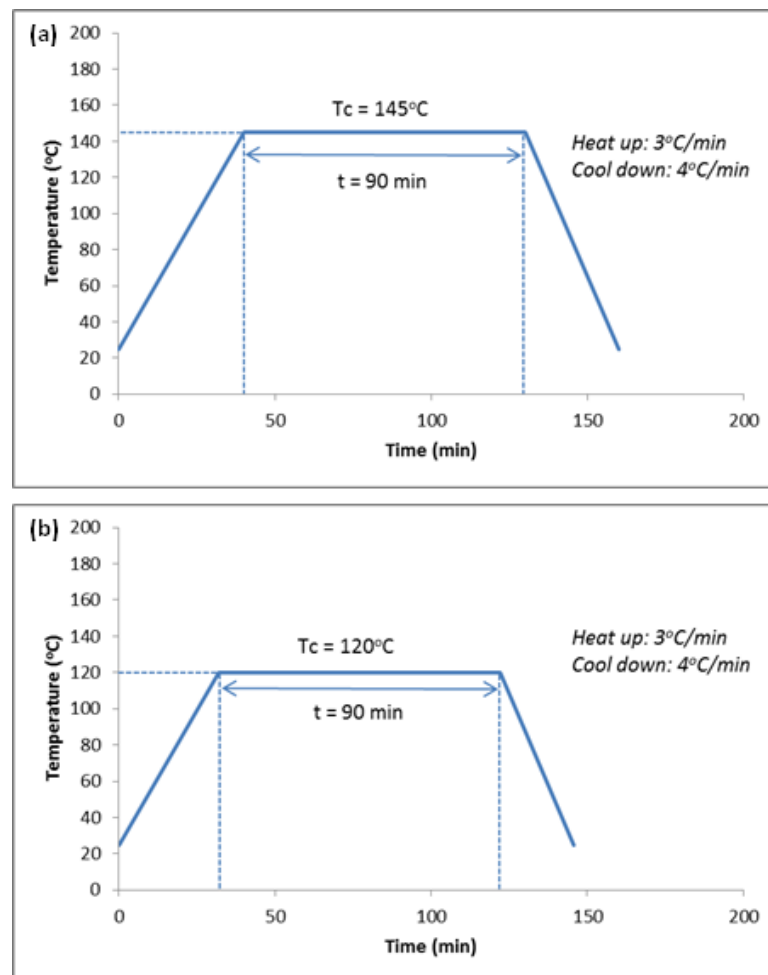


Figure 3.10 Heating cycle for the curing of (a) Glass fibre and (b) Carbon fibre prepreps.

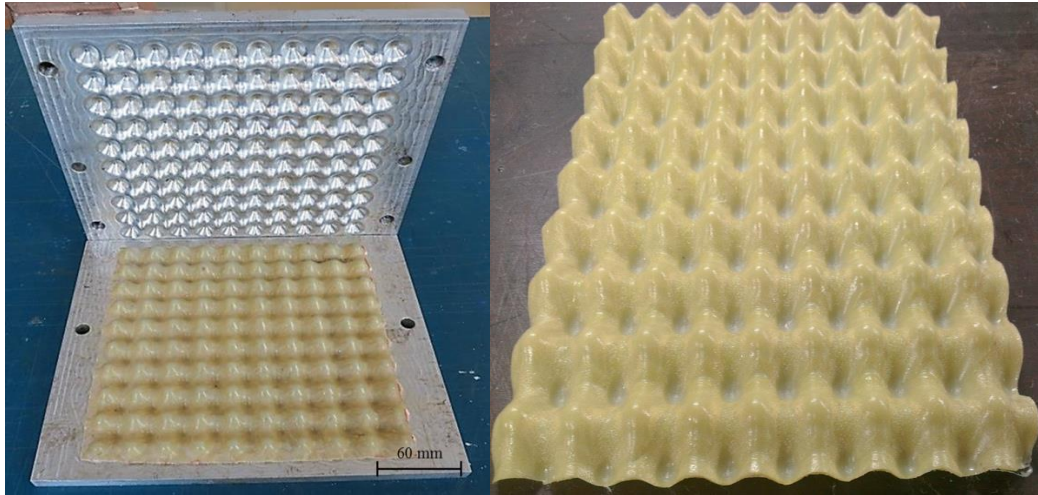


Figure 3.11 Photograph of spherical roof contoured core specimens following removal from the mould.

Finally, the spherical roof contoured cores were cut in three different geometries: unit cells, 2x2 and 3x3 structures, and flat roof contoured core were cut into 1x1 and 2x2 unit cells as shown in Figure 3.12, each of them to be bonded and tested. Hence, besides the investigation of the influence of the cell wall thickness on the energy absorption and impact response of the samples, the effects of the number of unit cells was also studied in this present work.

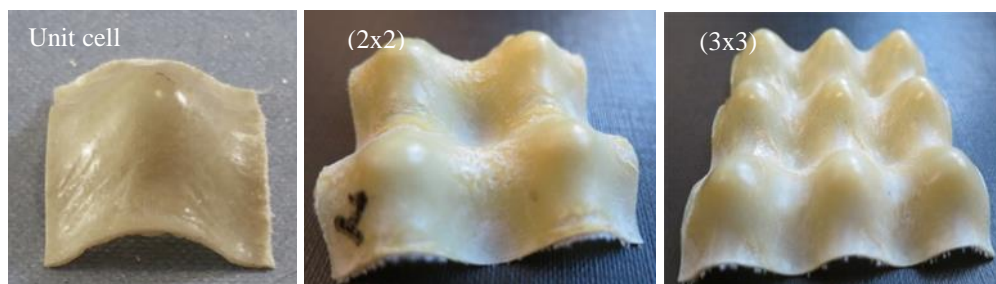


Figure 3.12 Spherical roof contour core specimens

3.4.2 Skin manufacturing

The skin preparation procedure is basically the same as that of the core, except the suppression steps for the mould preparation, where the skin mould is already covered with a Teflon tape. The hot press settings are also slightly different, starting with the pressure, maintained as 2.0 bar during all the curing process. The skin moulds with composite plies are only placed on the plattens when the temperature is already at the desired value. In this study, the GFRP skins were manufactured by stacking 5 prepreg sheets in the mould, the thickness of the resulting skin was 0.5 mm. CFRP skins having similar thickness was produced by stacking 2 prepreg sheets in the mould.

3.4.3 Bonding between skin and core

Initially, the adhesive was prepared by mixing a two-part epoxy resin (Araldite 420 A/B) in the ratio of 10:4. The calculations for the amount of glue needed to bond the flat roof top to the skins is based on the surface area of the roof, which is a circle with radius $r_b = 7.5\text{mm}$ [67]. Hence the volume of glue can be expressed by the surface area (πr_b^2) of the flat circle multiplied by 1mm, which is the estimated high for the layer of adhesive applied.

For the novel spherical roof contoured panels, the same calculations were based on the filling of a cylindrical surface, as shown in Figure 3.13.

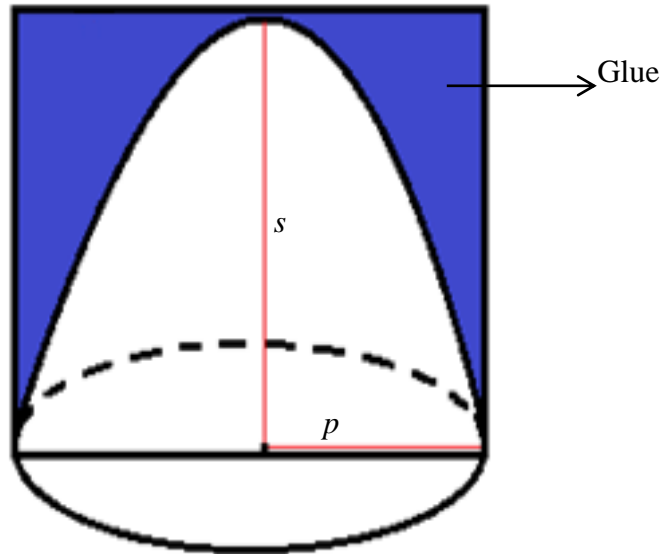


Figure 3.13 Schematic diagram of a spherical top dome covered with glue until the filling of an imaginary cylinder.

Approximating the shape of the dome to a spherical cap, the volume contained on it can be calculated through Equation 3.11, having “ s ” as the height of the dome, which is 0.75 mm, and “ p ” as the radius of its basis, equal to 0.1mm. $V_{CYLINDER} = \pi p^2 s$ represents the volume of a cylinder and $V_{DOME} = \frac{\pi h}{6} (3p^2 + s^2)$ represents the volume of spherical roof. Therefore, the amount of glue required to bond one dome is given by Equation 3.11.

$$V_{DOME} = \frac{\pi h}{6} (3p^2 - s^2) \quad (3.11)$$

The glue was then applied using a syringe, as exhibited in Figure 3.14, which allowed the necessary precision concerning the position of the glue spot and its quantity. After bonding, the panels were cured in an oven at 120°C for approximately one hour. All core parts were bonded with the 0.50 mm thick skin.

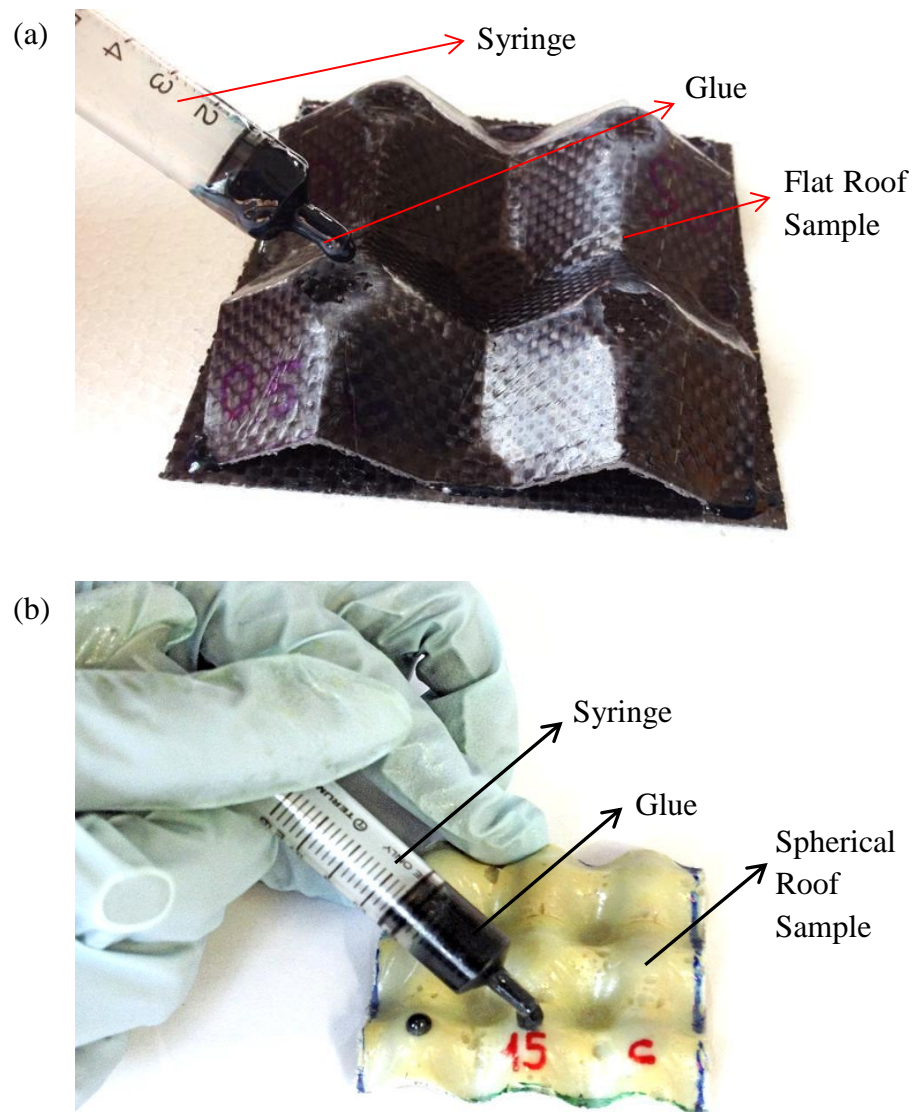


Figure 3.14 Adhesive been applied to (a) Flat-roof sample; (b) Spherical-roof sample.

3.5 Foam filled contoured sandwich panels

To investigate the influence of filling the contoured core sandwich panel with foam, a liquid polyurethane (PU) rigid foam, LDP40 supplied by Polycraft Ltd., was introduced into the core. Two chemical components were used to manufacture the foam. Component A is termed an apolyol blend (clear liquid) and component B is called Isocyanate (brown liquid). Both the chemical components were mixed manually to pour into the contoured sandwich panels. Here, the three sides (edges) of the panel were closed by sello tape and one side of the panel was kept open to pour the liquid into the bonded sandwich panel. To avoid the damage bonding between skins and contoured core due to the free expansion of liquid foam, a minimum pressure was given on the top surfaces of the skins. Figure 3.15 shows a conventional contoured core sandwich panels with fully-filled PU foam.

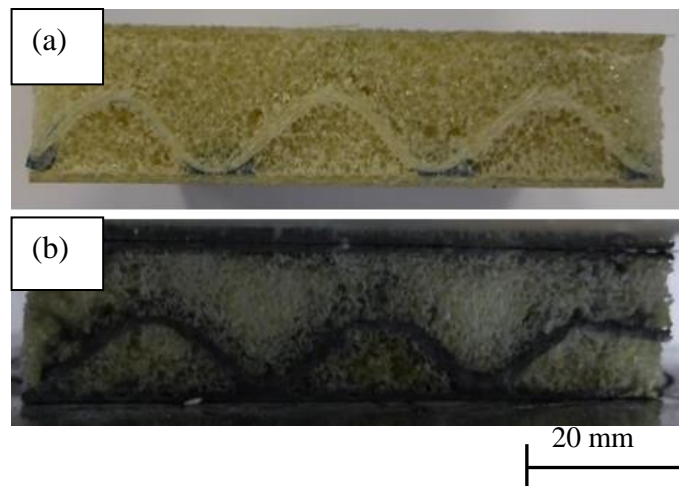


Figure 3.15 Foam filled spherical roof contoured panels (a) GFRP (b) CFRP

In order to investigate the properties of the PU foam, the foam was cut into 25 mm cubes. The density of the foam was measured according to the ASTM D1622 standard [113]. Figure 3.17 shows the free-rise rigid PU foam following manufacture and also a cube-shaped specimen with a measured density of $40 \pm 5 \text{ kg/m}^3$.

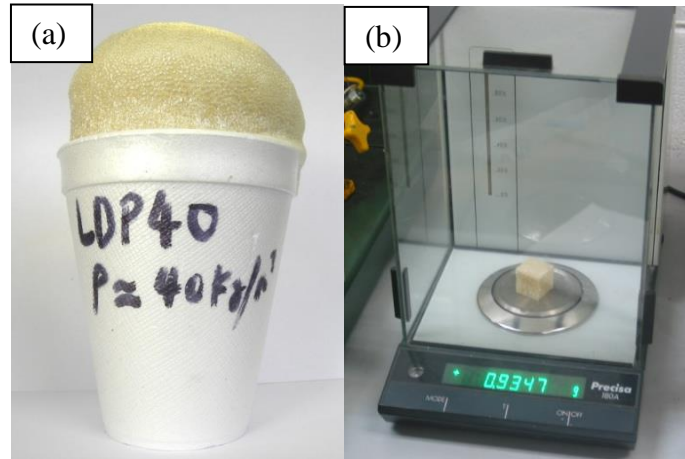


Figure 3.16 (a) Free-rise in the rigid PU foam and (b) a cube-shaped foam block on the weight scale.

3.6 Mechanical Properties of Materials

The material properties of the constituent materials are one of the most important factors in determining the deformation characteristics of a structure. The material properties of composites are commonly obtained from a standard tensile and compression tests. This type of test generally involves axially loading a specimen at both ends at a constant strain rate. In the present study, all of the static tests were conducted on an Instron 4505 testing machine. This machine is an electromechanical universal testing machine in which the forces are applied by a moving crosshead movement driven by a screw mechanism. Load-displacement traces are directly plotted from the measured loads and displacements.

3.6.1 Tensile tests on the GFRP and CFRP composites

Tensile tests were conducted on the GFRP and CFRP composite laminates in accordance with the standard BS 527-4[113]. The specimens were prepared by bonding aluminium end-tabs as shown in schematic Figure 3.18.

A minimum of three test specimens (dimensions: 250mm length x 25 mm width x 1 mm thick) were used for the tensile tests. The tensile tests were performed using an Instron 4505 testing machine. Again an extensometer with a gauge length, $GL = 50$ mm was attached to the specimen in the longitudinal direction. Tests were undertaken at a constant crosshead speed of 1 mm/minute.

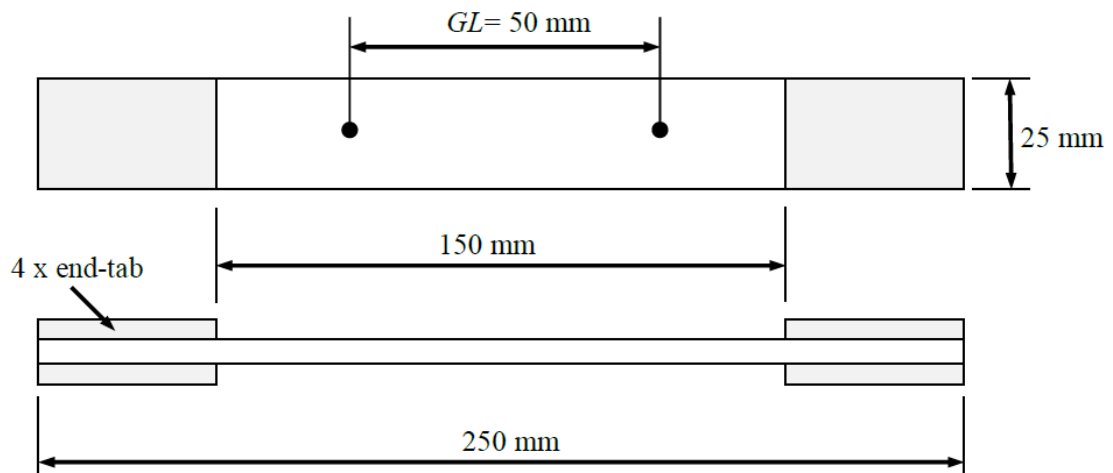


Figure 3.17 Tensile test geometry for a composite specimen.

3.6.2 Compression tests on rigid PU foam

Compression tests on the rigid PU foam were conducted using an Instron 4505 testing machine according to the ASTM D1621 standard [114]. All specimens were cubic in form with overall dimensions of 25 mm x 25 mm x 25 mm. Figure 3.19 shows a

typical specimen placed between the platens of the test machine. The specimens were deformed at a static loading rate of 1 mm/minute.

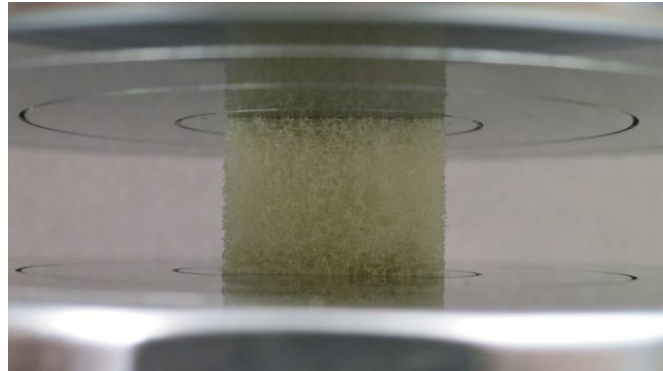


Figure 3.18 The rigid PU foam under compression loading.

3.7 Static compression tests of contoured-core sandwich structures

The static compression tests on the contoured-core sandwich structures were conducted using an Instron 4505 testing machine. All of the test specimens were prepared in a square form, being based on different numbers of unit cells and thicknesses.

The specimen was placed between the platens of the machine as shown in Figure 3.20 and was deformed by applying a uniform cross head movement at a quasi-static rate of 1 mm per minute. At least three tests were carried out on each specimen type. The energy absorbed by the specimen during deformation was calculated by integrating the area under the force vs. displacement curve, by using Microsoft Excel. The resultant values for energy absorbed are then used as a parameter for the execution of the low velocity impact test, since this result is equivalent to the energy needed to completely fracture the sample. Engineering compression stress-strain curves were

calculated from the applied force (normalised by the planar area of the samples) and the crosshead displacement (normalised by the original height of the samples). The use of nominal strain is purely for the convenience of comparison.



Figure 3.19 A specimen under compression loading using Universal Testing Machine INSTRON 4505.

3.8 Low velocity impact tests

The impact tests were conducted using a drop-weight impact rig as presented in Figure 3.21. A certain amount of energy was transferred by a travelling free fall of a known mass to the specimens which were loaded axially. The mass and height of the impactor were adjusted to obtain desired impact energy, E , based on test requirement. This can be calculated by $E = mgh$.

Here, m is the mass [kg], g is the gravitational constant [9.81 m/s^2] and h is the height. Prior to testing, the test specimens were placed on the impact plate and positioned parallel to the direction of the impactor as shown in Figure 3.19. To begin with, a flat rectangular impactor, with dimensions of 120 mm x 80 mm was raised to a predefined level depending upon the speed and impact energy. The movement of the impactor was guided by two greased steel rails with a $\pm 0.5 \text{ mm}$ clearance. Therefore, the contact between the impactor and rails was presumed to be frictionless. The impactor was released once the entire test configuration was ready. The dynamic compression tests were stopped when the specimens had been completely crushed. Data were collected from the computer corresponds to the impact loading while the high speed camera represents the displacement of the crush.

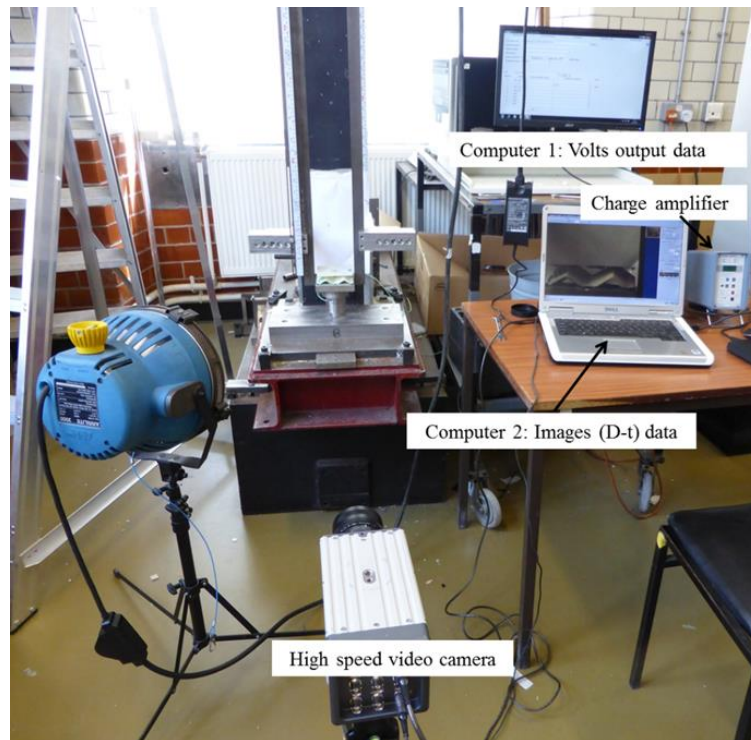


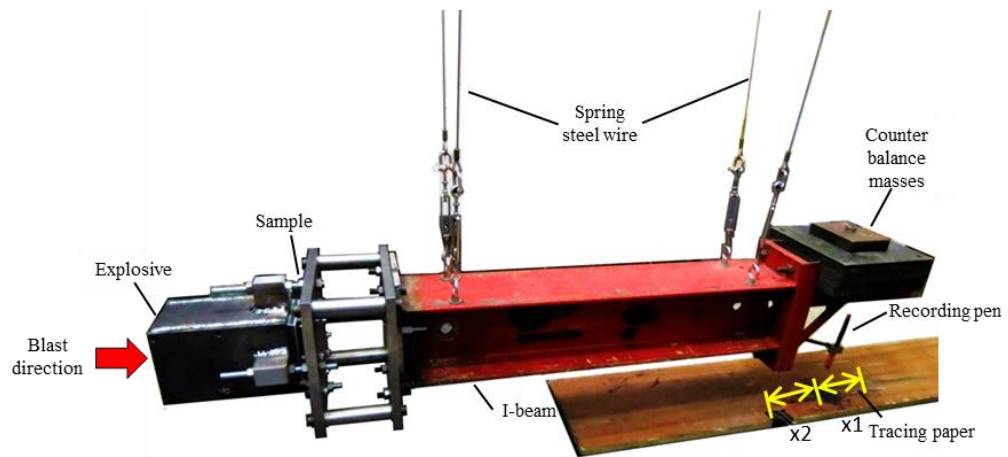
Figure 3.20 The instrumented drop-weight impact test set-up adopted for testing the contoured-core sandwich structures.

A Load cell mounted beneath the impact plate was used to measure the voltage-time histories during the impact events. The Kistler type 9363A load cell with measuring range of 120 kN was connected to a charge amplifier using an insulated co-axial cable. During impact, the mechanical force was sensed by a pressure sensor in the load cell and converted to an electrical signal. As the electrical signal output is in order of millivolts, amplification of the signal was done by a charge amplifier. A digitiser device was used to convert the analog signals generated into digital signals and they were recorded using a computer. Finally, the force (N) readings were obtained by converting the voltage using a scaling factor of 12,000 N/V which was found by conducting a static calibration on INSTRON Machine.

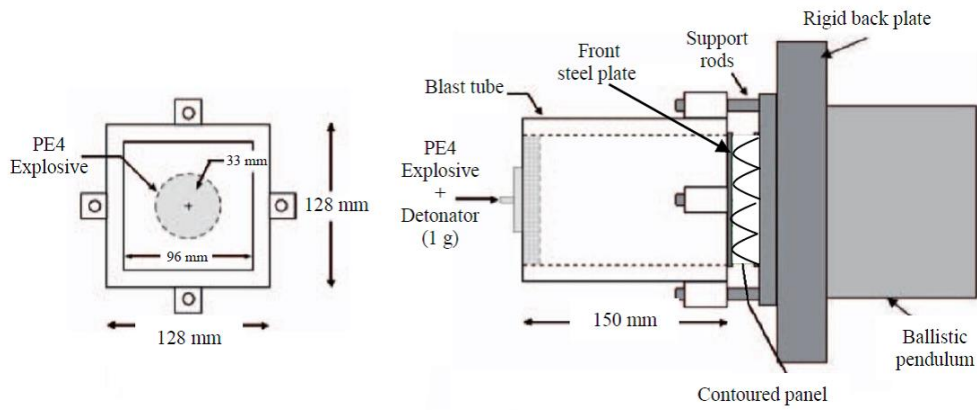
The motion of the impactor was captured using a high speed video MotionPro X4, model no. X4CU-U-4 with a standard F/0.95-50 mm lens positioned in front of the impact rig. For all impact tests, the frequency of the high speed video was set to be 10,000 frames per second. Before conducting the test, a target with 15 mm scale was placed on the surface of impactor in order for the high speed video to track the motion. The video file was captured and processed using the MotionPro software, Version 2.30.0. This video file was then analysed and calibrated with the 15 mm scale using the motion analysis software, ProAnalyst, to produce the displacement data. A further analysis using Matlab 2012a software was required to calibrate the force data to the displacement.

3.9 Blast tests

Blast tests were also undertaken on the spherical roof contoured parts, using a ballistic pendulum at the University of Cape Town. These tests were carried out to evaluate the dynamic response of the cladded core parts subjected to one of the most severe forms of loading (blast). Here, tests were conducted on (5x5) or (i.e.100mm x 100mm) unit cells with a core cell wall thickness of 0.5 mm on CFRP and GFRP respectively. Two millimetre thick aluminium plates were bonded to the cores create a sandwich structure using epoxy adhesive (Araldite 420 A/B), which in turn was bolted to a ballistic pendulum. A steel plate, with dimensions similar to those of the skins of the sandwich structure was attached to the front of the panel using double-sided adhesive tape. The cladding is used to maximize the energy absorption of the panel and limit the force transfer to the main structure to be protected. This in turn distributes the loading across the cladding structure, enabling the core to deform uniformly under the blast impulse [115]. The sandwich structures were then attached to the ballistic pendulum and a square cross-section steel tube was mounted in the front of the sandwich structure to guide the blast load. Plastic explosive (PE4) was mounted into a flat disc of 33 mm in diameter and located at the open end of the tube. The detonator was attached to the centre of the disc using 1 gm of explosive. The explosive charges (varied from 6 gm to 12 gm) were located at the open end of square blast tube at a distance of 150 mm from the front aluminium plate, as shown in Figure 3.22.



(a)



(b)

Figure 3.21 (a) Photograph of the ballistic pendulum used for conducting the blast tests and (b) schematic of the detonator and blast tube arrangement

The damping constant β of the periodic motion of blast pendulum can be calculated by equation (3.12) below [116]:

$$\beta = \frac{2}{T} \ln \left(\frac{x_1}{x_2} \right) \quad (3.12)$$

where x_1 and x_2 are found from measurements taken from several pendulum oscillations in which the pendulum was drawn back and released respectively. The natural period T is simply determined by averaging a number of measured pendulum oscillations which was found to be about 3.413 seconds.

Also the initial velocity of the pendulum \dot{x}_0 can be calculated by the following equation.

$$\dot{x}_0 = \frac{2\pi}{T} .x_1 .e^{0.25\beta.T} \quad (3.13)$$

Finally, the impulse I can therefore be calculated as.

$$I = M .\dot{x}_0 \quad (3.14)$$

where M is the total mass of the pendulum, including the test rig, I-beam, and the counter mass, which is overall 101.28 kg.

Summary of the chapter

Chapter III has presented details of the design and fabrication of the flat-roof and spherical-roof contoured profiles of aluminium mould. The contoured moulds were designed using the commercial CAD/CAM software and manufactured to a high precision using a computer-controlled numerical milling machine (CNC). The manufacturing process of contoured-core sandwich structures using hot press compression has also been explained. The contoured core structures were fabricated from woven GFRP and CFRP. Here, the processing cycles for the prepreg curing were defined according to the manufacturer's specifications. The fabrication processes of bonded flat-roof and spherical-roof samples were also described. Araldite 420 (A/B) adhesive was used to bond the samples. Here, the calculations to precisely determine the amount of glue to bond the core and skins have been elaborated. In this chapter, the experimental set-up as well as the testing procedures for the quasi-static, dynamic and blast tests were explained in detail. The tensile test specimens, made from GFRP and CFRP materials, were manufactured to obtain the basic properties via tensile tests.

Finally, the contoured sandwich structures were filled with low density rigid PU foam in order to investigate the effect of applying an additional internal support (i.e. the foam) on the compression response of these novel contoured sandwich panels.

Chapter 4 Results and discussion

4.1 Introduction

In this chapter, detailed results from the experiments conducted on the contour cores will be presented. These include those from a series of quasi-static tensile tests, quasi-static compression tests, impact crush tests and blast tests. The results on sandwich structures under quasi-static and dynamic loading will also be presented and discussed. Finally, the failure mechanisms observed in the structures during and after the tests will be characterised.

4.2 Mechanical properties of the materials

This section discusses the results obtained from a series of tensile tests on the GFRP and CFRP laminates. This section also explains the properties of PU foam following compression tests.

4.2.1 Tensile tests on the composites

Stress-strain curves for the GFRP and CFRP are given in

Figure 4.1. Here, except for the initial engagement, GFRP composite laminates exhibit an almost linear response, whilst the CFRP laminates show a bi-linear response up to the maximum stress value. At this point, the composite failed in a catastrophic manner across the width of the sample, as shown in Figure 4.2, provoking a rapid drop in the stress-strain curve. For both materials, fracture occurred approximately at the middle of the gauge length and the orientation of the fracture surface was observed to be perpendicular to the tensile axis. The CFRP specimens exhibited a higher tensile strength (550 MPa) than the (GFRP 320 MPa) with failure strains of 0.026 and 0.022 in the carbon and glass based systems respectively.

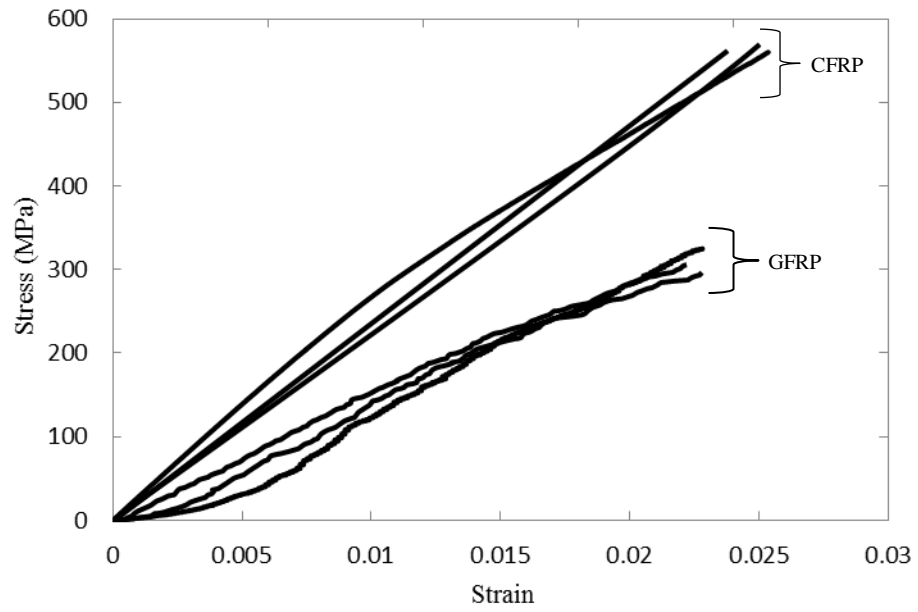
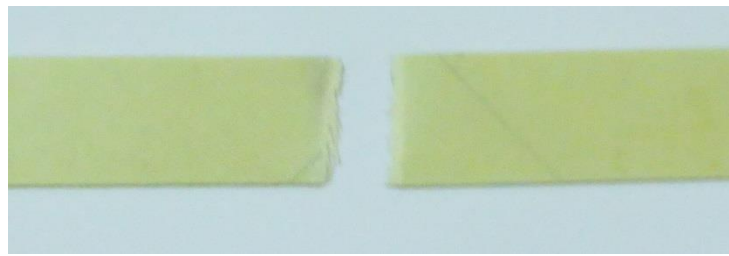
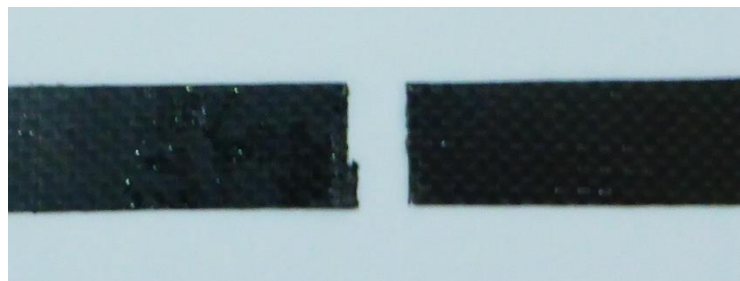


Figure 4.1 Tensile stress-strain curves for the GFRP and CFRP specimens.



(a) GFRP



(b) CFRP

20 mm

Figure 4.2 Failed composite samples.

4.2.2 Compression tests on the rigid polyurethane foam

Here, the behaviour of the rigid polyurethane (PU) foam includes its modulus of elasticity, compressive strength and energy absorption characteristics. Figure 4.3 shows the mechanical response during a quasi-static compression test. Compression in the rigid PU foam gives rise to the three phases of response, each corresponding to distinct deformation mechanisms. Following these phases, for compression strains less than 5 %, the foam obeys Hooke's law, where the engineering strain is directly proportional to the applied stress. The modulus of elasticity was determined directly from the slope of this curve, with an average value of 4.7 MPa being recorded. When the compression strain reaches 6 %, the stress-strain plot exhibits a peak at a plastic collapse stress of approximately 0.14 MPa. The initial linear elastic response is controlled by elastic axial compression and bending of the cell edges, stretching of cell faces and compression of the gas within closed cells [21]. The second phase, occurring between strains of 7 % and 43 %, is characterised by a relatively constant plateau stress, with an average value of approximately 0.13 MPa. This progressive crush causes the cells to crumple in the compressive direction and the foam to become thin. The final deformation phase involves densification of the foam, where the majority of cell walls collapse and opposing cell walls touch with each other. The energy absorption characteristics can be calculated from the area under the curve up to the point of densification, typically at 60 % of strain.

Anisotropy can sometimes be very significant in some types of foam. Mines et al. [117] reported that the compression yield values varied slightly, but the elastic modulus remained almost constant in the three different principal directions. In this

study, it is assumed that the rigid PU foam behaves as an isotropic material and therefore, the compression response is uniform in all principle directions.

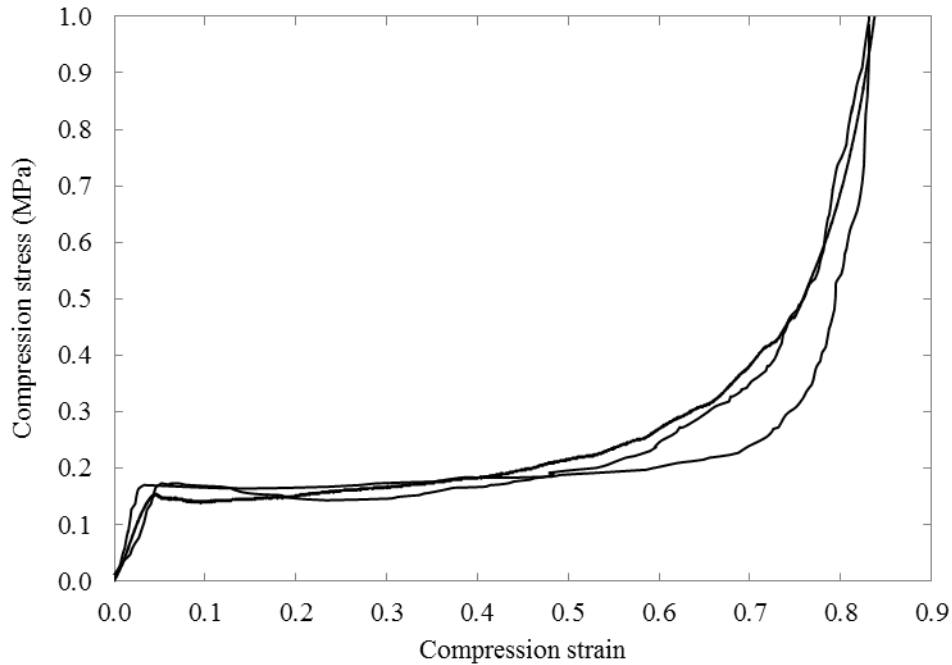


Figure 4.3 Compression stress-strain behaviour of the rigid PU foam.

4.3 Static compression tests on contoured cores

Quasi-static compression tests were carried out to determine the compression strength and stiffness as well as energy absorption capacity of the specimens under compression loading.

4.3.1 The compression behaviour of the flat roof contoured core

Initially, crushing tests were conducted on 2x2 flat-roofed contoured core components, made from GFRP and CFRP. A cell wall thickness of 0.50 mm was chosen for these core components. Stress-strain curves for the GFRP and CFRP are shown in Figure 4.4. Here, the initial response was similar up to the peak in the trace.

After the maximum, the cell wall collapses and a drop occur in the stress-strain traces for both the CFRP and GFRP. However, the plateau stress was much higher in CFRP than in the GFRP. This plateau stress is associated with the mechanical properties of CFRP material. With further loading, densification occurs and rapid rise in stress is observed for both type of material.

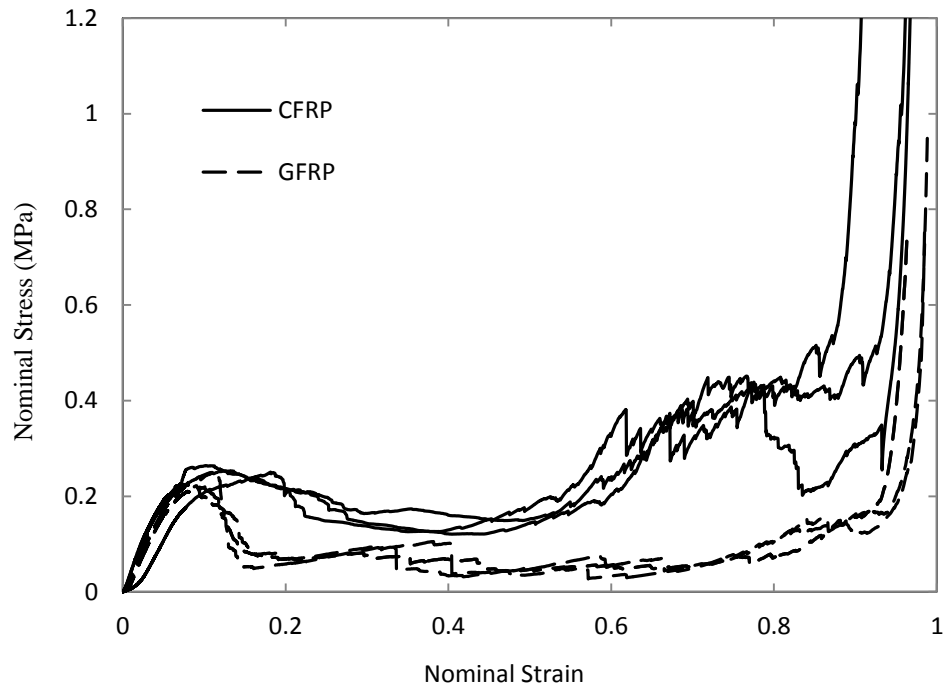
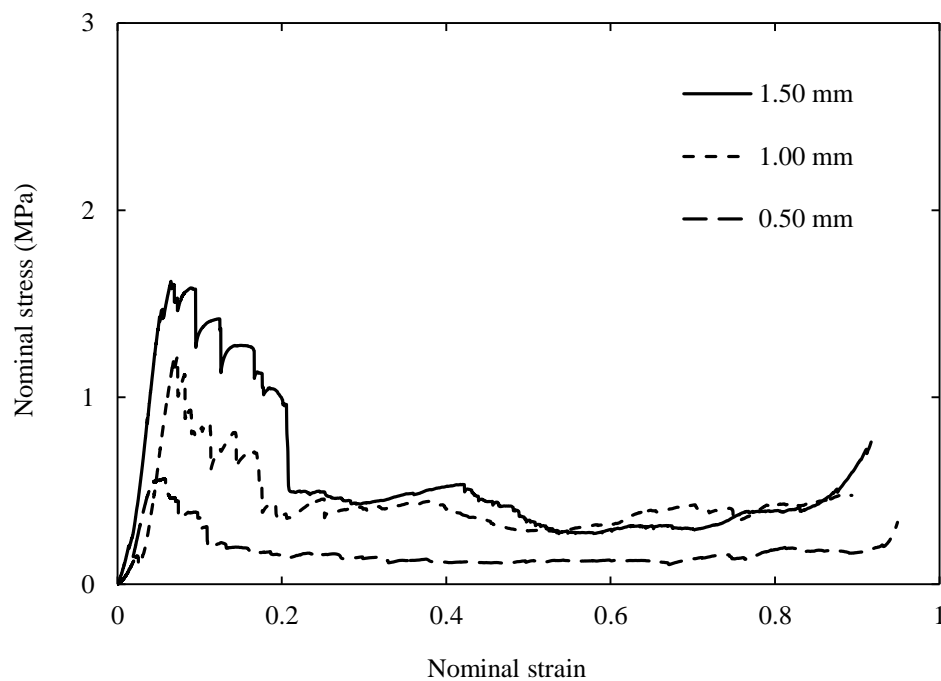


Figure 4.4 Quasi-static stress-strain traces for unbonded (without skin) 2x2 flat roof contoured cores.

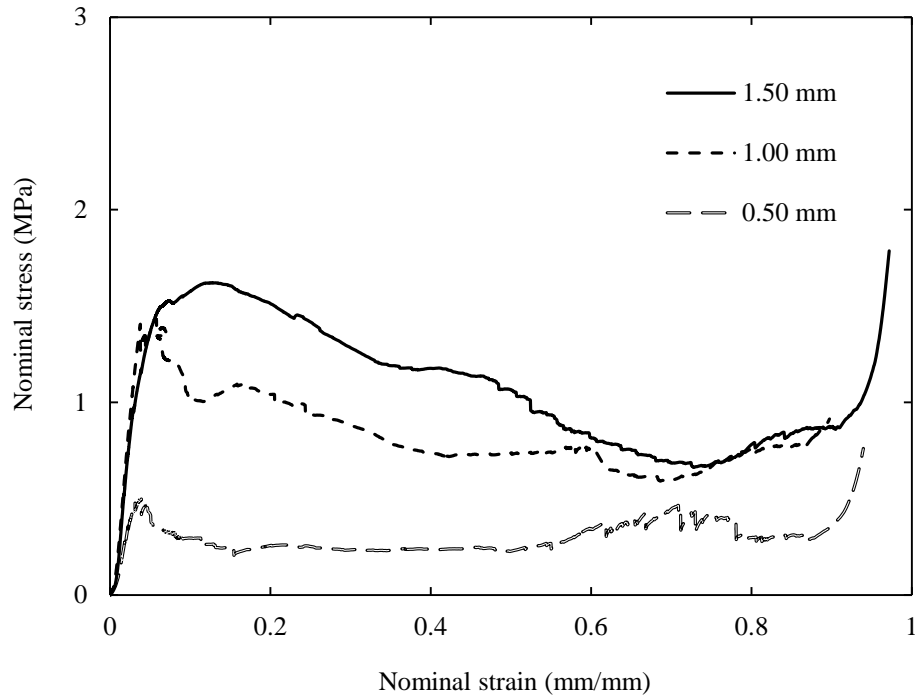
4.3.2 The compression behaviour of the flat-roof contoured core sandwich structures

Following the above experiments on unbonded samples (i.e. without skins), the tests were also conducted on bonded samples (i.e. with skins). Three thicknesses of cell wall, as previously mentioned in Chapter 3, were used for both carbon and glass fibre prepregs to understand the effect of varying the cell wall thicknesses. Figure 4.5 (a)

and (b) show nominal stress-strain traces of the cores with cell wall thicknesses of 0.50, 1.00 and 1.50 mm for GFRP and CFRP, respectively. The traces for the responses of GFRP materials exhibit a brittle failure with a peak stress increasing with cell wall thickness, as indicated in Figure 4.5(a). After the initial peak stress, a crack was initiated which propagated under the continued loading to causing a reduction in structural stiffness. As a result, the cone wall started to buckle, leading to a sudden drop in stress. The cell walls subsequently debonded from the skin, resulting a plateau regime in the curves between strains of 0.1 and 0.5. During the later stages, the sample was completely crushed beyond the densification threshold. These stages of deformation are shown in Figure 4.6. Densification initiated at strains of between 0.6 and 0.8. The experimental results indicate that the CFRP panels were crushed in a ductile manner, resulting in a smooth and progressive drop in the stress-strain trace, as shown in Figure 4.5 (b).



(a) GFRP



(b) CFRP

Figure 4.5 Quasi-static stress-strain traces on bonded 2x2 flat roof contoured core panels, the wall thicknesses are indicated in the figure.

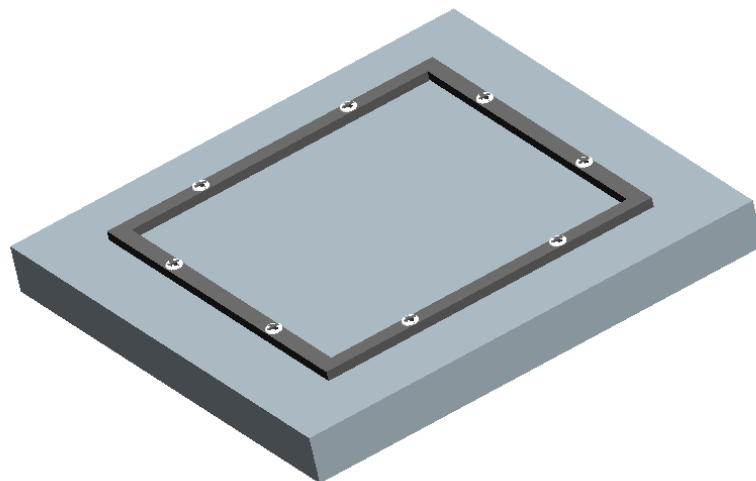
Figure 4.5 shows that an increase in cell wall thickness results in an increased compressive strength and plateau stress. The static compressive strength of the GFRP samples with the wall thicknesses of 0.5 mm and 1.5 mm were found to be 0.50 MPa and 1.59 MPa respectively. Almost a similar initial compressive strength was observed for CFRP as compared with the GFRP, with varying thicknesses. However, the CFRP samples exhibit a much higher plateau stress than the GFRP, for all thicknesses of the panels. For example, the average value of plateau stress for CFRP is three to four times higher than that for their GFRP counterparts.



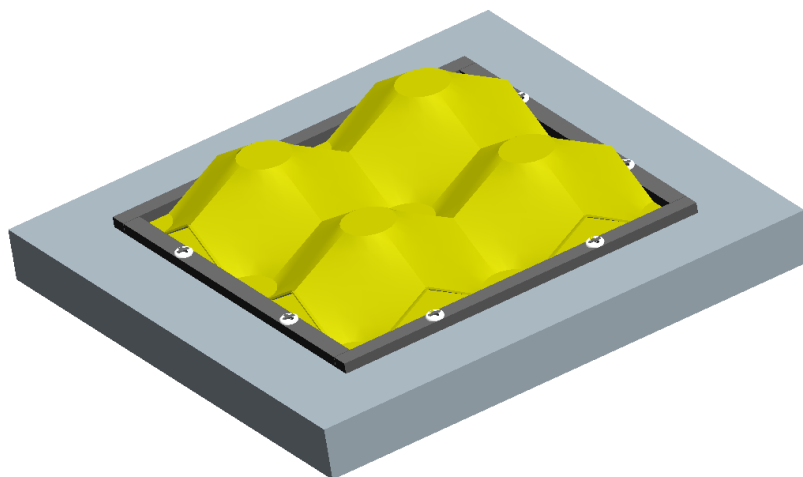
Figure 4.6 Progressive crushing of the flat roof glass fiber contoured panel during a compression test.

4.3.3 The Effect of edge constraint on contoured cores

It is evident that the selection of a suitable energy-absorbing structure for a specific application will depend upon both the geometry and material, where the collapse is restricted to a well-defined crush zone. Therefore, the lateral movement of the flat roof contoured core was restricted to understand the response of these core parts under a well-defined crushing area, as shown in Figure 4.7.



(a) Base platten



(b) Base platten with specimen

Figure 4.7 The platten arrangement used to restrict the deformation of the specimen during compression testing.

Here, quasi-static compression tests were carried out on 0.5 mm thick contoured cells of GFRP and CFRP, under an arrangement which restricts the lateral displacement of the specimen, as shown in Figure 4.7. Typical stress-strain curves produced by these arrangements are shown in Figure 4.8, for both the GFRP and CFRP. The associated images during the deformation process are shown in Figure 4.9 (a) and (b). The GFRP

exhibits four phases of deformation, i.e. an initial elastic region, yielding, followed by a plateau region due to crack propagation, fiber breaking and buckling of the cell wall leading to densification and a rapid rise in stress, as shown in Figure 4.8.

The response of the CFRP sample becomes progressively non-linear during continuous loading, where the flat bottom face of the CFRP-core takes on a triangular shape under crushing and the applied load starts to increase further due to interactions between the triangular surfaces of the cell walls and the upper platen. Finally, the CFRP-core is completely densified.

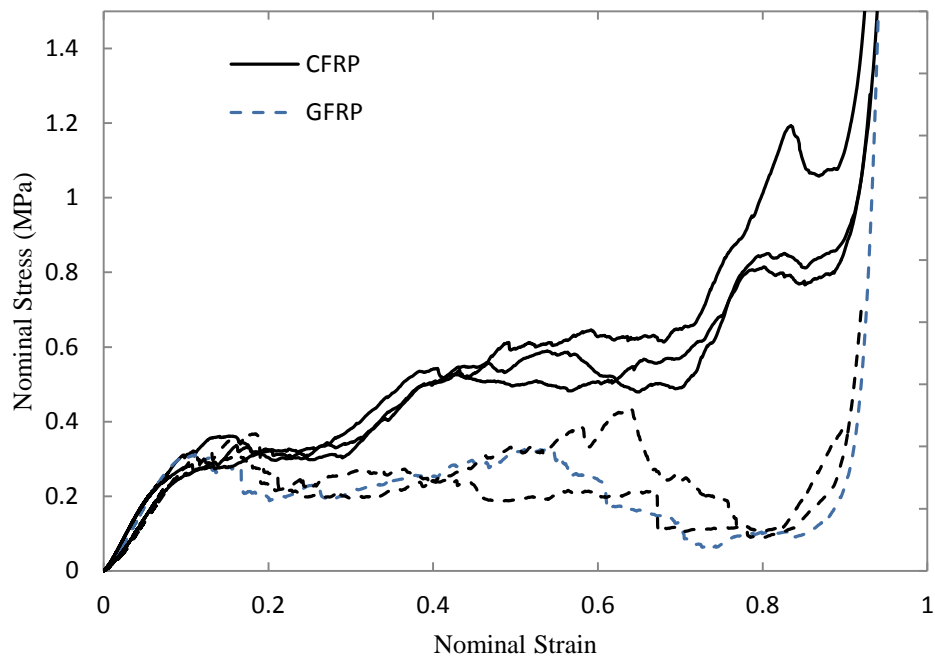


Figure 4.8 Quasi-static stress-strain curves of constrained 2x2 flat-roof contoured GFRP and CFRP cores.

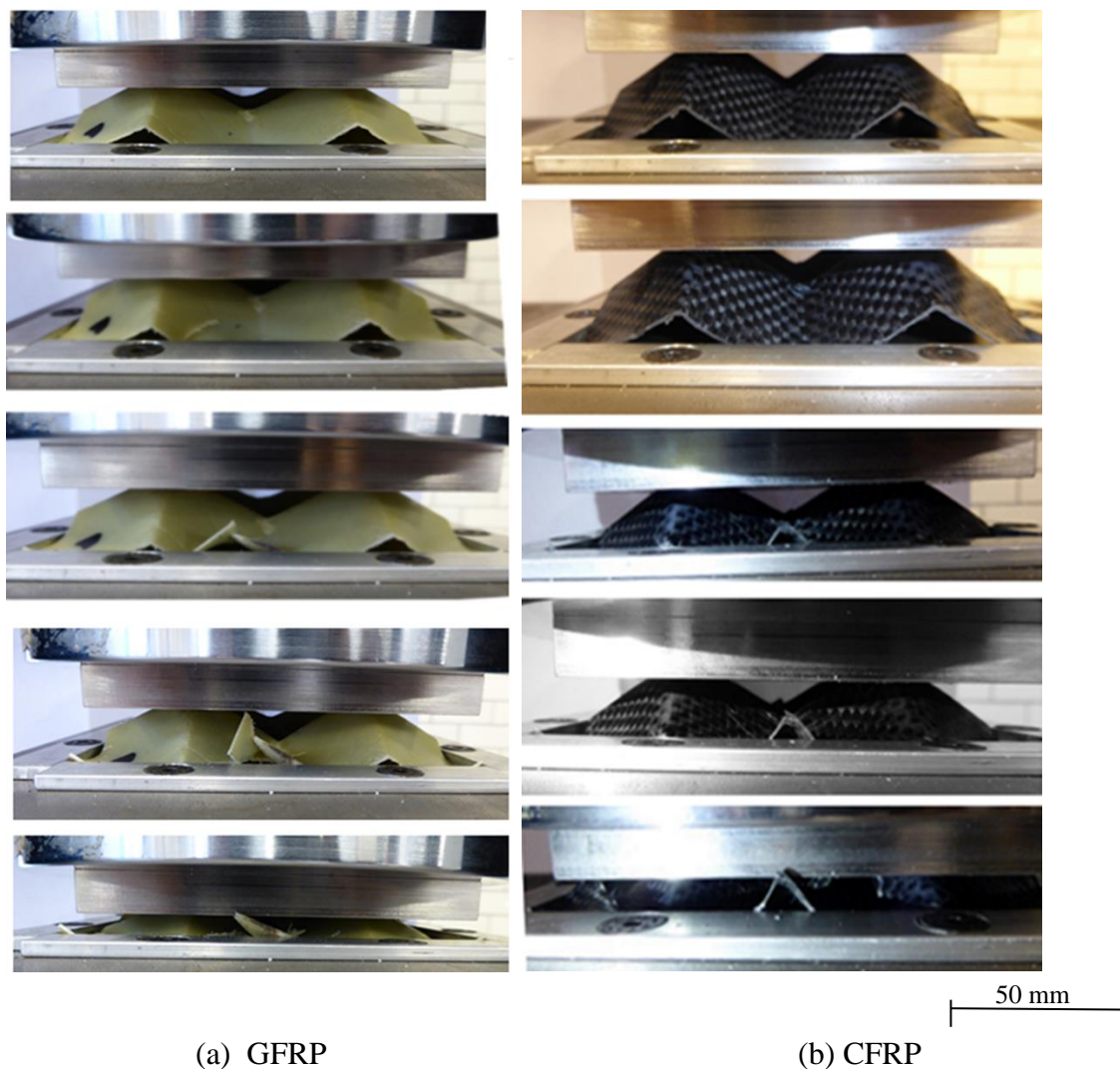
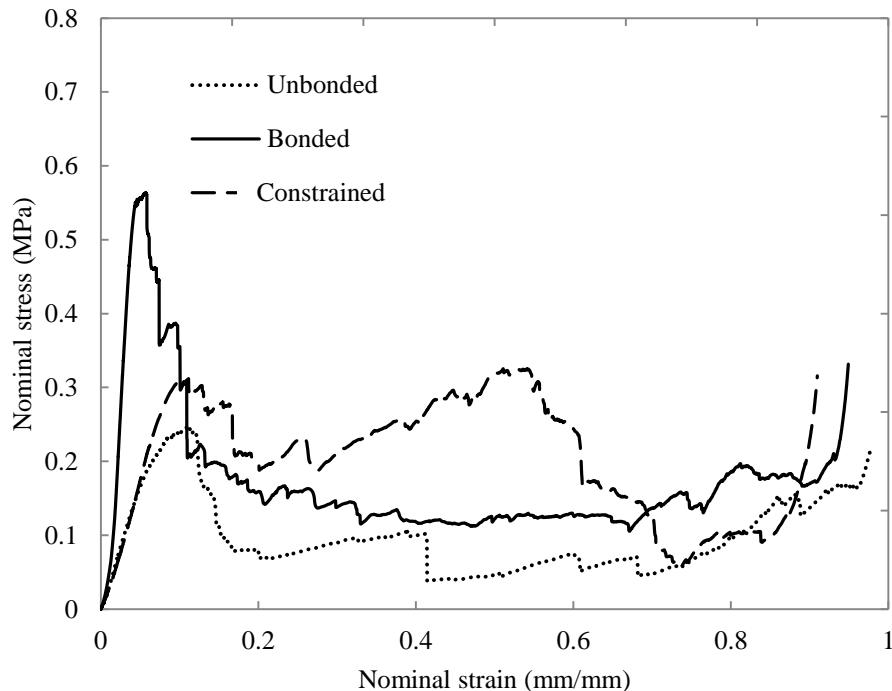


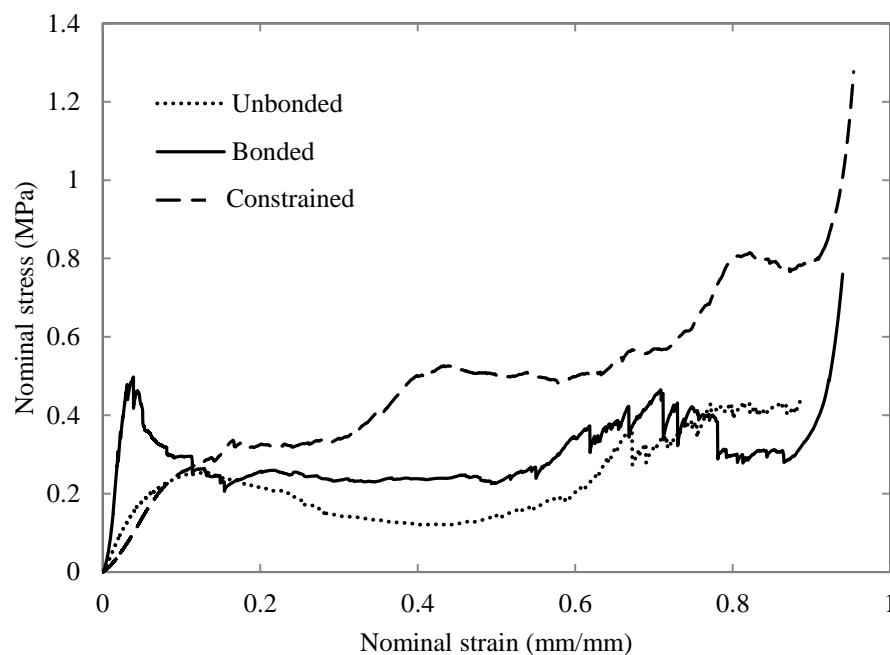
Figure 4.9 Images of progressive damage development in the constrained flat-roof contoured systems.

The experimental traces obtained following the quasi-static tests on the unbonded, bonded and constrained structures are summarised in Figure 4.10 (a). In general, a significant increase in initial peak and modulus of elasticity was observed in the bonded samples for both GFRP and CFRP respectively. These properties highlight the presence of the stronger and stiffer cell structure in the bonded condition. After an initial peak, the stress in the GFRP samples suddenly dropped, whereas the reductions were more gradual after the first peak in the CFRP samples. There is no significant

difference in initial peak and modulus of elasticity between the unbonded and constrained samples. However, there is a significant difference in the plateau stresses between the bonded, unbonded and restricted flat roof contoured samples. It was found that the plateau stress continuously increased in the constrained samples. This increase in load capacity is associated with the restriction of the lateral displacement associated with the restricted boundary walls of the platen, Figure 4.7(b). This restriction results in extensive folding and buckling of the contoured walls under quasi-static loading. Figure 4.10 also shows a significant difference in the plateau stresses for the bonded and unbonded structures, where the plateau stresses for unbonded GFRP samples are between 20% and 50% lower than those for bonded GFRP. A similar trend in plateau stress is also obtained for the bonded and unbonded CFRP samples, with the stress values between 0.2 and 0.4 MPa.



(a) GFRP



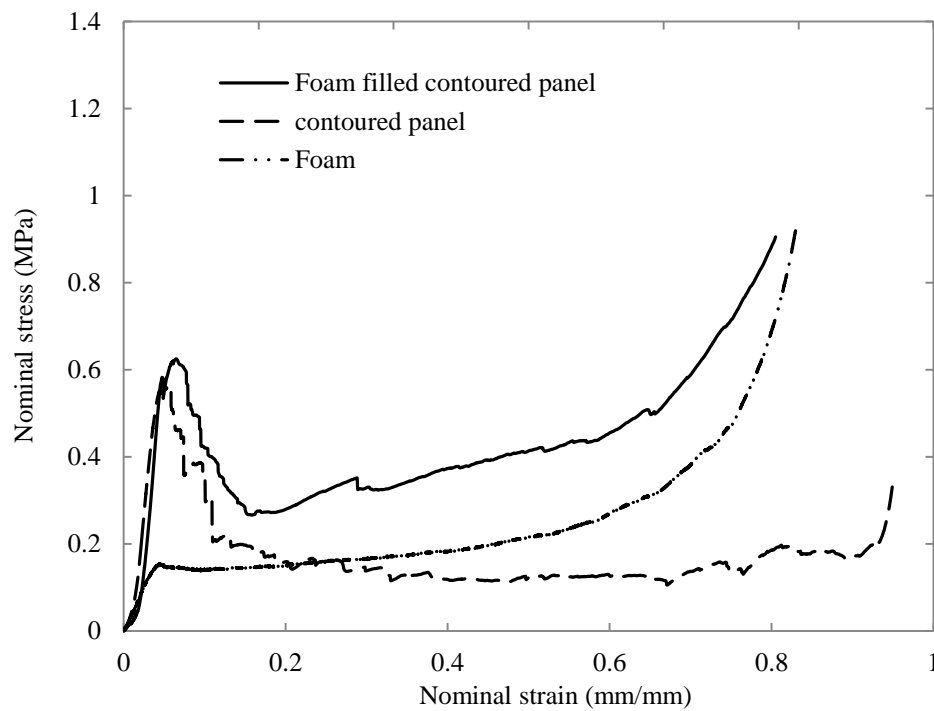
(b) CFRP

Figure 4.10 A comparison of the bonded, unbonded and constrained 2x2 flat-roof contoured structures under quasi-static load.

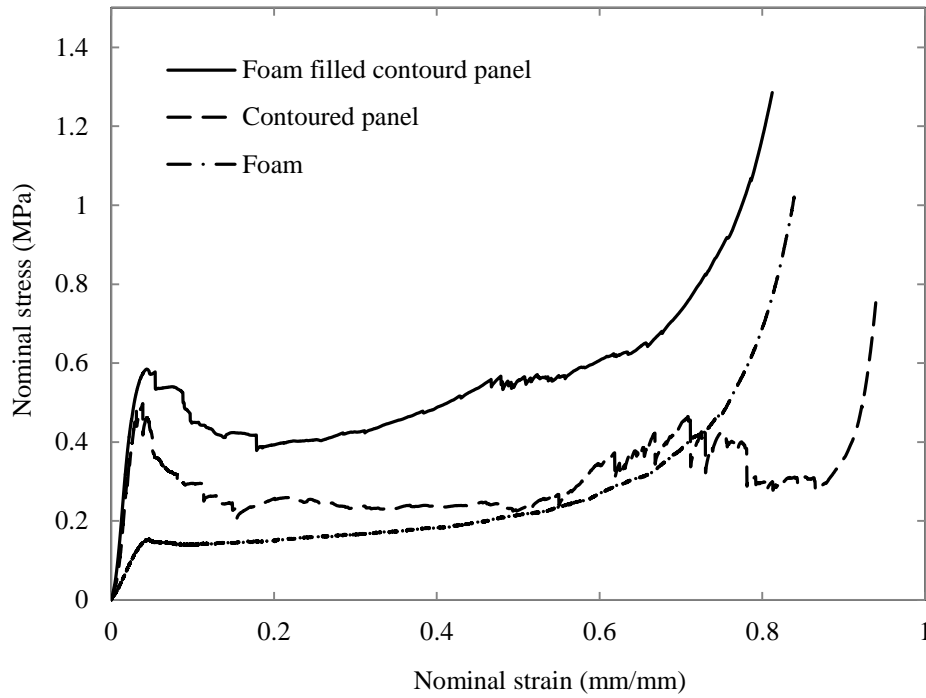
4.3.4 Compression on foam-filled flat roof contoured panels

In the next stage of this research, the mechanical behaviour of core panels filled with foam was investigated. Here, 0.5 mm thick cell wall CFRP and GFRP panels were filled with a PU foam. Figure 4.11(a) and (b) show stress-strain traces following quasi-static tests on the foam filled GFRP and CFRP panels, respectively. These figures also include the corresponding traces for the PU foam and the unfilled panels. From the figures, it is clear that the GFRP and CFRP sandwich structures filled with foam exhibit a higher compression strength and plateau stress compared to the conventional contoured panels. Being similar to thin walled honeycomb sandwich structures, the unfilled composite contoured panels also had stress oscillations in the stress-strain curves by successive brittle fracture and bending of the cell wall. Here, the stress oscillations were suppressed by the supporting action of the PU foam, which leads to a

stable collapse behaviour. However, for the glass/epoxy core filled with the PU foam, there is a relatively steep drop in stress after the initial peak. Following a large drop in peak stress from 0.6 to 0.28 MPa, the plateau occurs between strains of 0.2 and 0.6, before the densification. For the foam-filled carbon/epoxy core, the specimens exhibit a smooth plateau regime with stress increment. Here, after an initial peak of 0.55 MPa the stress dropped by only 10 to 15% and continued before the panel begins to densify. This resembles the collapsing behaviour of an ideal absorber.



(a) GFRP



(b) CFRP

Figure 4.11 Stress-strain traces following tests on the foam filled 2x2 flat-roof panels.

4.4 Compressive behaviour of the flat roof contoured panels subjected to impact loading

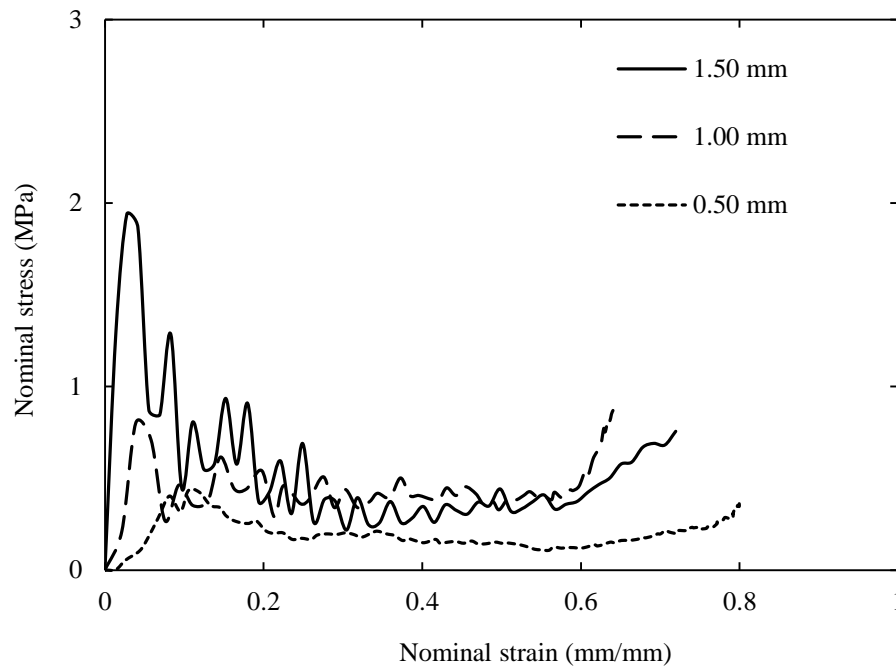
Crush tests at a high strain rate were performed using a drop-weight impact tower. A flat rectangular impactor, with dimensions of 120 mm x 80 mm, was raised to a predefined height to obtain the required impact energy. Table 4.1 summarises the test parameters used to evaluate the flat roof contoured panels.

Table 4.1 Test values used to test the flat roof contoured panels.

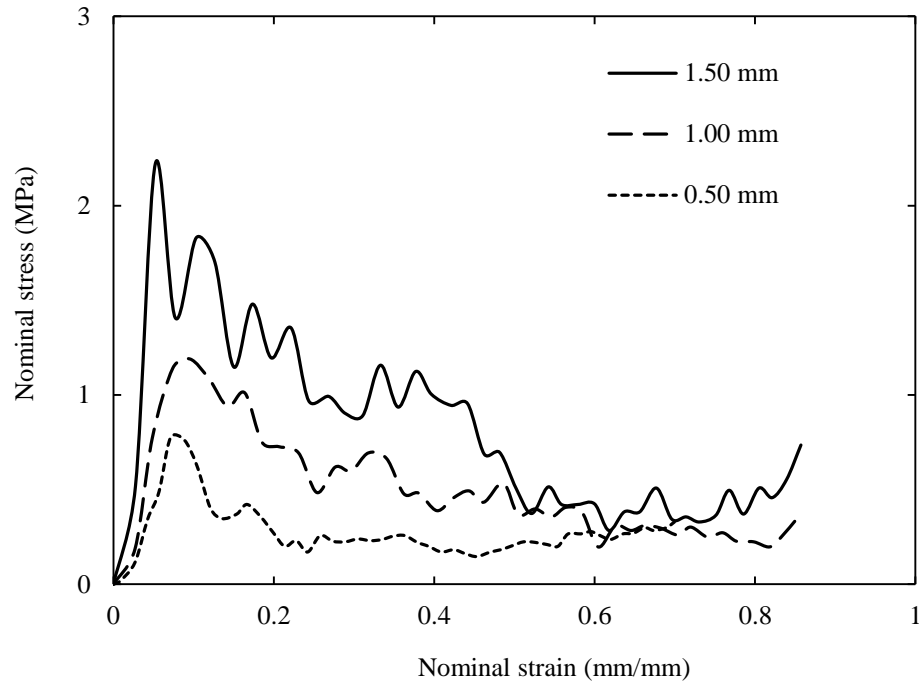
Material	Specimen cell wall thickness (mm)	Drop height (m)	Impactor mass (kg)	Impact energy (Joule)
CFRP	0.5	0.50	15.70	77.00
	1.0	1.10	15.70	169.41
	1.5	1.45	15.70	223.32
GFRP	0.5	0.40	8.43	33.00
	1.0	0.85	8.43	70.30
	1.5	1.40	8.43	119.91

Figure 4.12(a) and (b) shows stress-strain traces following drop-weight impact tests on the GFRP and CFRP flat roof contoured sandwich panels as a function of cell wall thickness. The results shown here are based on the average value of three repeated tests. The response curves are represented in terms of the nominal stress (equal to the applied load divided by projected area of the specimen) and nominal strain (equal to the displacement divided by the original specimen height). The energy absorption of the panel was determined from the area under the load-displacement trace up to the densification point. In general, the experimental traces display similar trends, i.e. linearly up to the peak stress followed by a sharp drop in GFRP or a relatively gradual drop of the resistance in CFRP, followed by a plateau stage due to the crushing of cell wall. The stress oscillates until the densification. Such oscillatory behaviour is likely due to dynamic effects in the load-cell and drop-weight carriage, as well as

instabilities during the fracture of the cell. It has been noticed that some of those traces exhibit an initial non-linear response, which is likely to be associated with the initial engagement between the specimen and the impactor. The structural stiffness and the peak stress are increased nonlinearly with increasing thickness. For example, the peak stress of the 1.5mm thick GFRP panel is 1.94 MPa, whereas it is only 0.4 MPa for 0.5 mm thick GFRP panel, i.e. almost a fivefold increase. A similar effect was observed in the CFRP panels with varying cell wall thicknesses.



(a) GFRP



(b) CFRP

Figure 4.12 The stress-strain relationship from low velocity impact tests on 2x2 flat roof contoured panels.

A comparison of the nominal stress-strain traces in Figure 4.5 and Figure 4.12 indicates that the average crush stresses are higher at dynamic rates of loading, which in turn gives a slightly higher energy absorption. The specific energy absorption (SEA) characteristics of the flat roof composite contour core structures were calculated by the integration of the load-displacement curve and dividing by the mass of the panel. The resulting values of specific energy absorption related to the dynamic loading are compared with their quasi-static counterparts in Figure 4.13. It is indeed clear that the dynamic values of specific energy absorption are higher than those of the quasi-static ones, suggesting a pronounced rate-sensitivity.

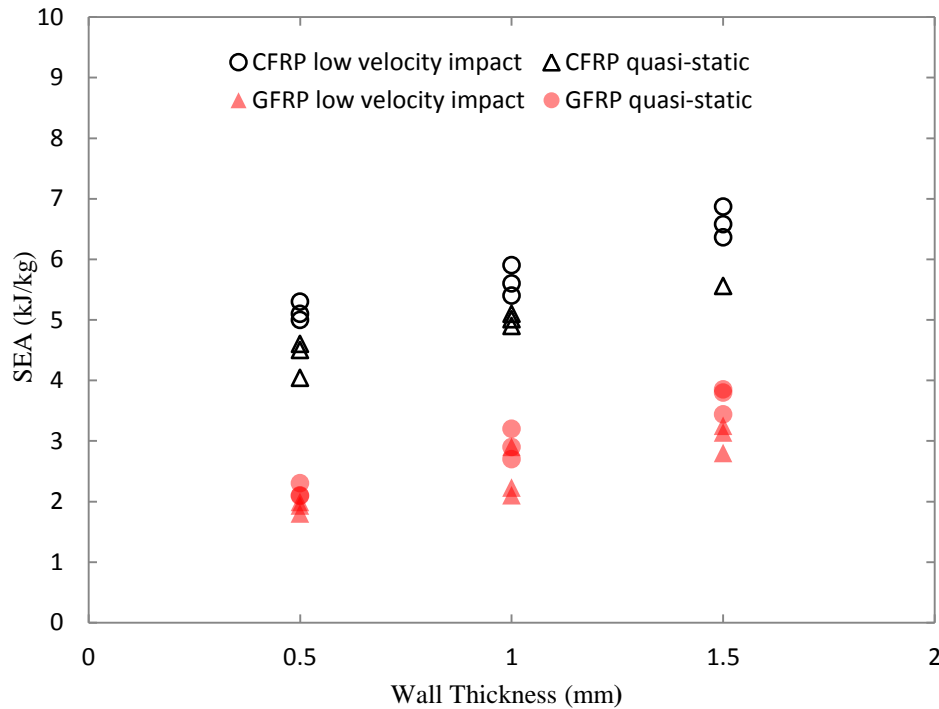


Figure 4.13 Specific energy absorption of 2x2 flat-roof contoured panels made of CFRP and GFRP.

4.5 Novel spherical roof contoured structures under quasi-static compression

Following the mechanical tests on the flat roof contoured core panels, a series of compression tests were performed on spherical roof contoured panels. In this part of the research, the main focus is to identify the influence of the number of unit cells, constraint and wall thickness in determining the overall deformation and collapse behaviour. Compression testing on the core structures highlight significant differences and their respective responses, which are summarised below.

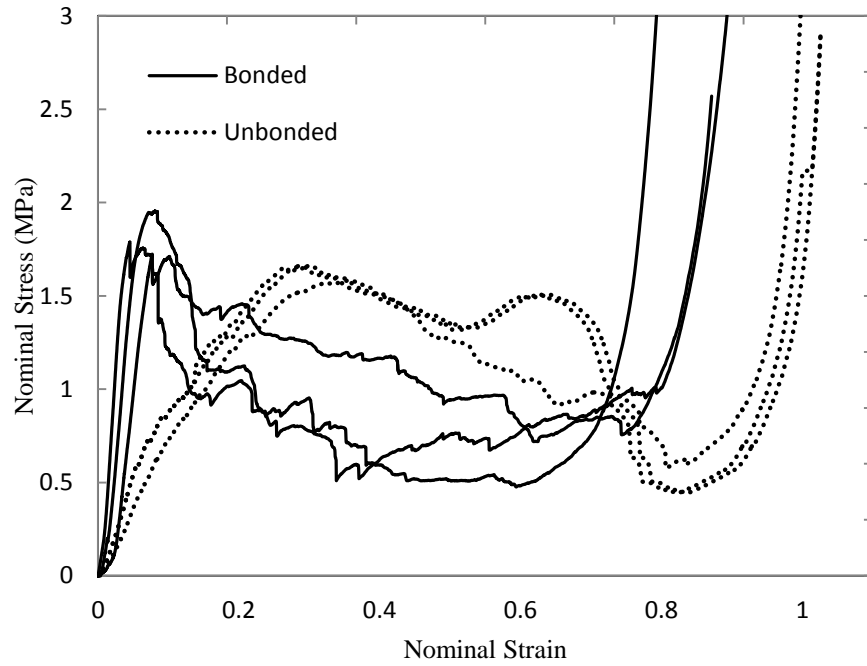
4.5.1 Compressive response of the GFRP spherical roof contoured structures

Figure 4.14 (a) show stress-strain curves for the GFRP contour core structures, including the core (unbounded) and sandwich structures (bonded) samples. Typically,

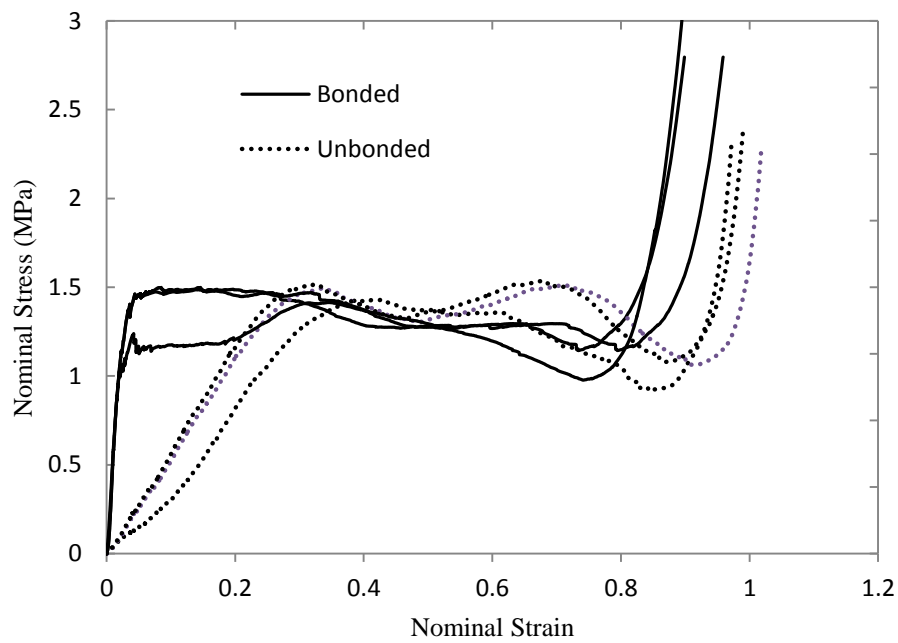
the GFRP samples exhibited a more brittle type of behaviour, involving extensive crushing and matrix cracking with fibre fracture, as shown in Figure 4.15. The response of the bonded GFRP sample differs significantly from that of the unbonded samples. A significant increase in the modulus of elasticity was observed in the bonded samples for the GFRP. These bounded contoured cores showed a higher structural stiffness than the unbounded core, whereas the initial softening takes place on unbonded samples which reduces the initial structural stiffness. This was caused by the bonded skin restraining the core from sliding horizontally during compression. The stress then progressively decreased as the fibres began to fracture. In the unbonded core, after an initial rise in stress up to 1.5 MPa, the structural response constantly decreased until the final densification threshold.

4.5.2 Compressive response of the CFRP spherical roof contoured structures

Stress-strain traces following compression tests on the CFRP core structures are presented in Figure 4.14 (b). In the first stage, the compression response seems to be linear up to the peak stress. The response then becomes nonlinear and the stress begins to decrease progressively as the specimen flattens between platens. Densification starts at a nominal strain between 0.8 to 0.9. However, for the sandwich structure, the peak stress was slightly higher than the plain core. The stiffness of the sandwich sample is much greater than its plain counterpart, which is attributed to the constraint offered by the skins.



(a) GFRP



(b) CFRP

Figure 4.14. Mechanical response of the 3x3 bounded and unbonded contoured structures subjected to compression.

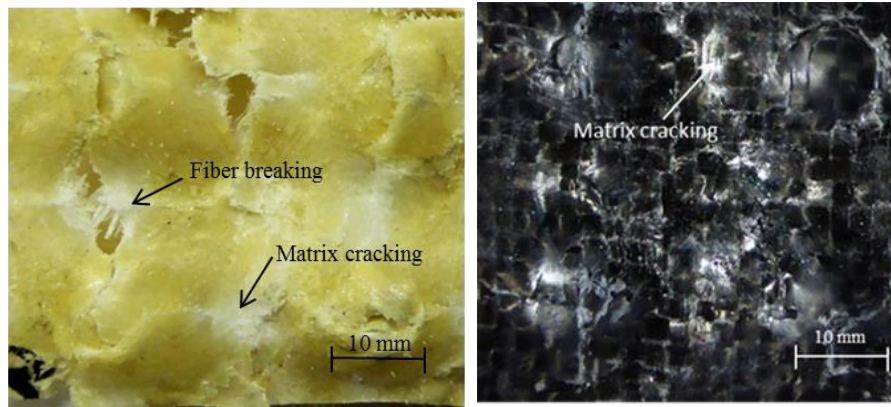


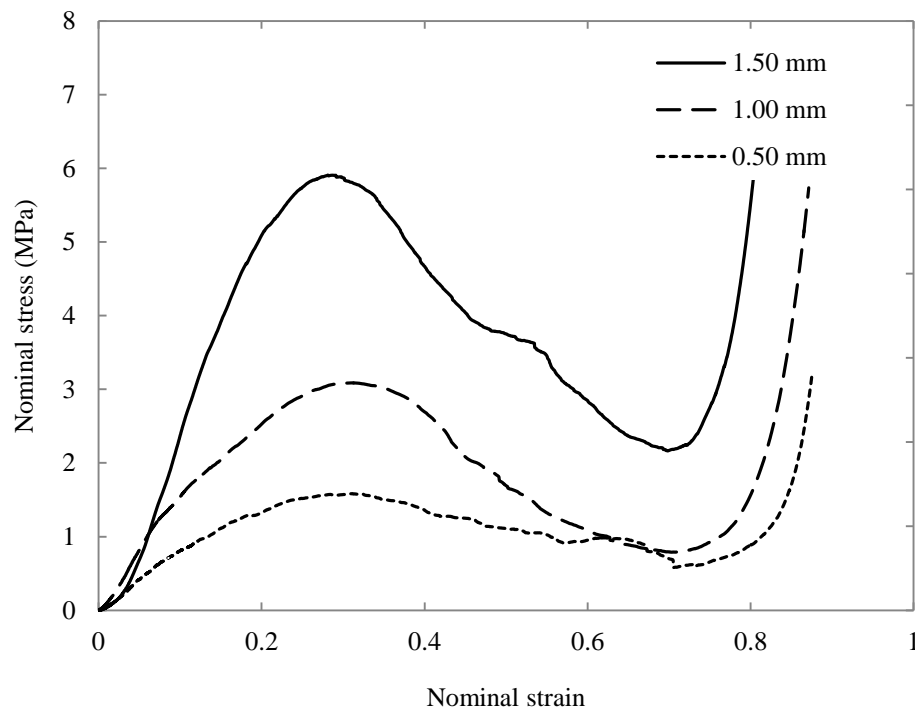
Figure 4.15 Fractured surfaces of GFRP and CFRP.

4.5.3 Compression response of composite contoured structures as a function of cell wall thicknesses

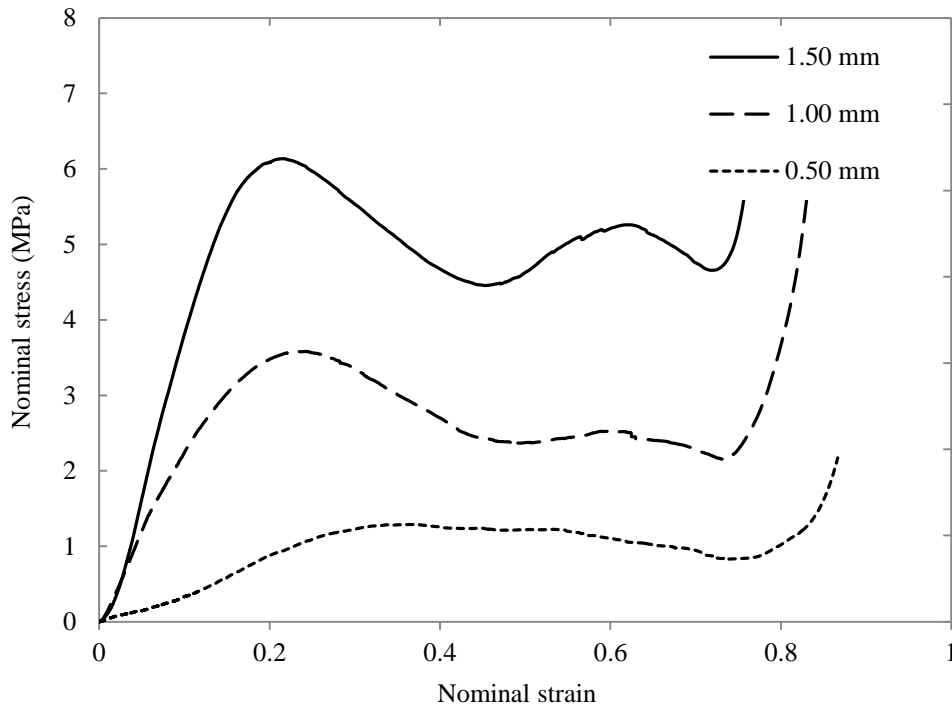
Compression tests were then carried out on the (3x3) spherical roof contoured cores as a function of cell wall thickness. The GFRP and CFRP panels respond in a roughly linear manner up to the peak stress, as shown in Figure 4.17(a) and Figure 4.17(b). Based on observations, it was evident that just after the first peak stress, the fibre starts to fracture and the crushing process continues until densification occurs, as shown in step-wise crushing images, Figure 4.16 . With increasing cell wall thickness, the compressive stress rises significantly by 50 percent. Clearly, the core based on a 1.5 mm thickness has a compressive strength of 6 MPa, whereas the 1.0 mm thickness only has a compressive strength of 3 MPa. It is also clear that the stress-strain plot of the GFRP drops more rapidly after the initial peak than the CFRP structures for all the thicknesses. This sudden drop in the traces may be associated with brittle failure in the GFRP than its counterparts.



Figure 4.16 Crushing process in the GFRP spherical roof contoured core.



(a) GFRP

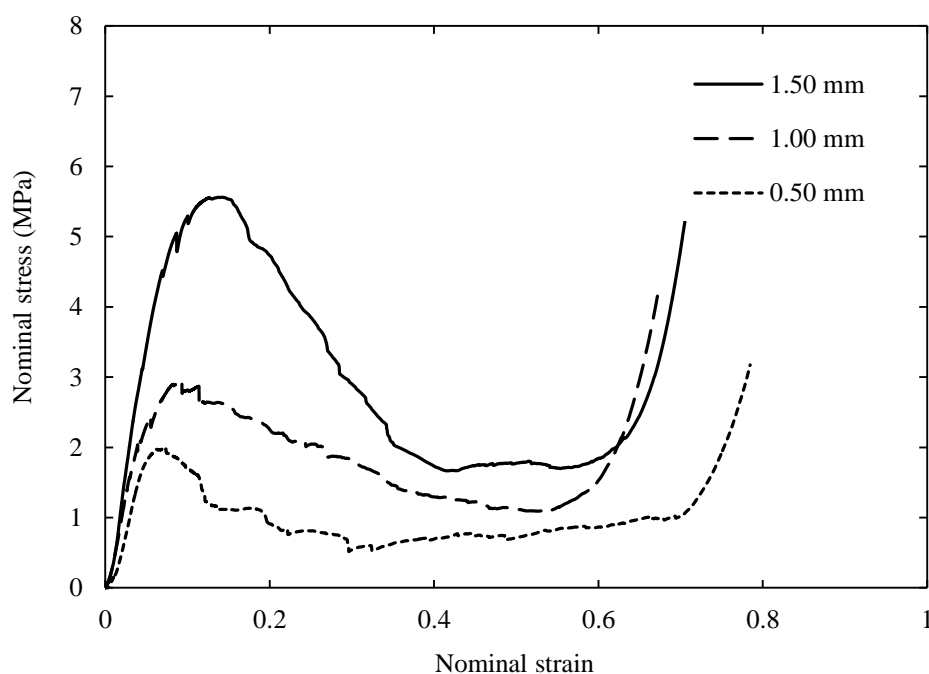


(b) CFRP

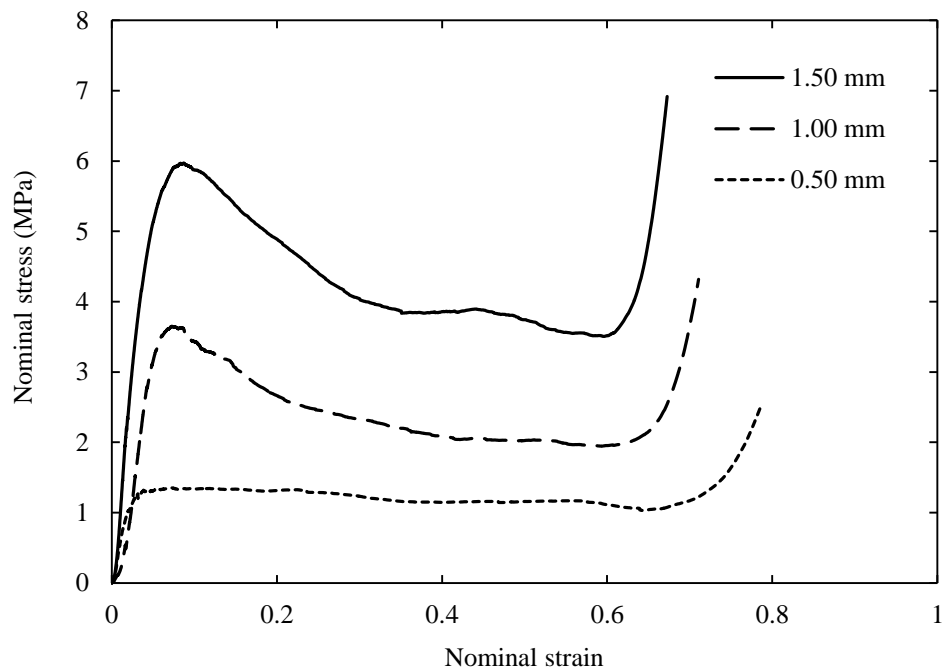
Figure 4.17 Quasi-static stress-strain traces for the 3x3 unbonded spherical roof contoured structures.

Further, compression tests were performed on the (3x3) spherical roof contoured bonded panels as a function of cell wall thickness. Similar to the unbonded cores, both the GFRP and CFRP panels respond in a linear manner up to the peak stress, as shown in Figure 4.18(a) and Figure 4.18(b). The response then becomes nonlinear and the load begins to decrease progressively as the specimen flattens between the plattens, with cracks and fibre fracture occurring within the structure. Similar to the flat roof contoured panels, the compression load rapidly increased in the spherical-roof contoured panels with increasing cell wall thickness. For example, the compressive load of the 1.5 mm GFRP contoured sandwich panel is roughly three times that of the 0.5 mm thick panel, as expected. The traces of the CFRP panels drop

slowly, with a significantly higher plateau level, except for the 0.5 mm thick cell wall panel, which contains only two plies that may contribute to the absence of peak. However, the GFRP panel with the same thickness was made from five plies. Although the peak stress in the 0.5 mm panel was higher than that of the CFRP counterpart, the subsequent plateau stress was much lower. This may be attributed to brittle failure and delamination between the plies. An observation of Figure 4.5 and Figure 4.18 indicates that the spherical roof contoured structures are at least two times stronger than the flat roof counterparts.



(a) GFRP

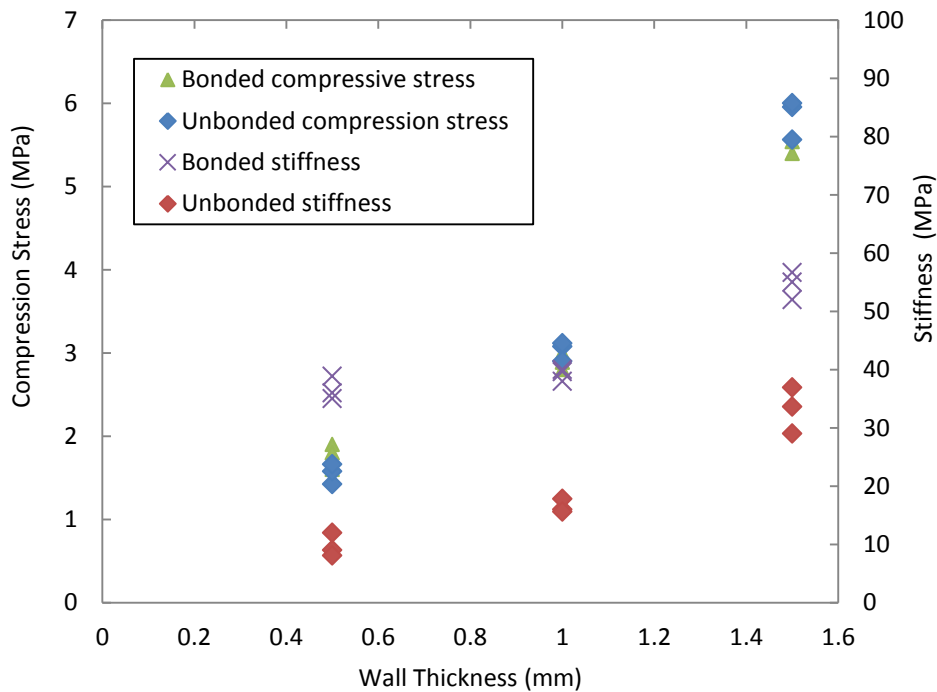


(b) CFRP

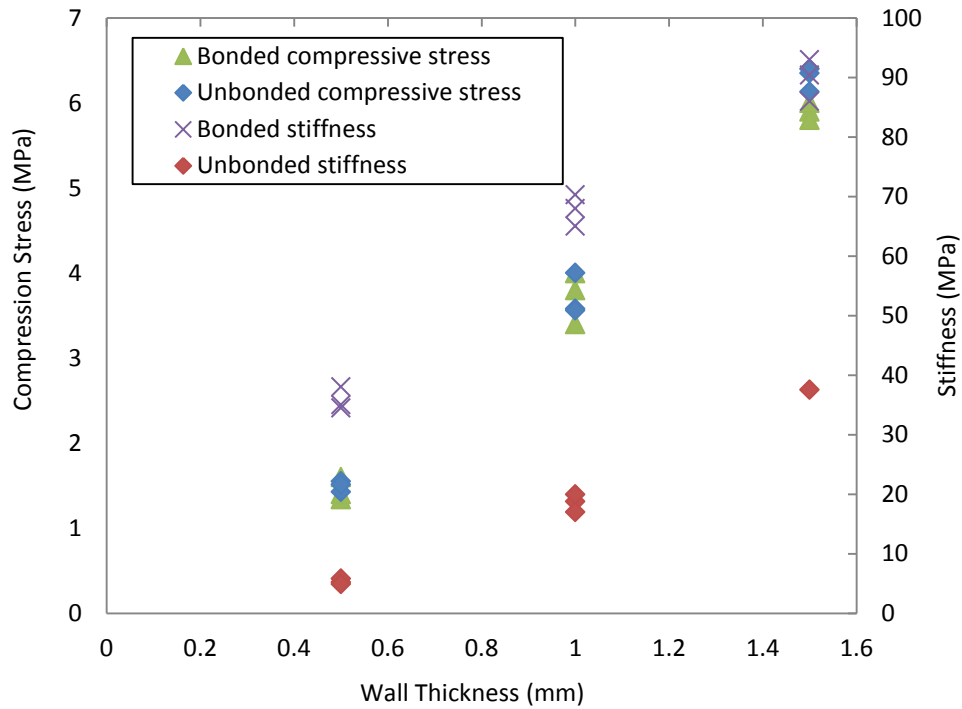
Figure 4.18 Quasi-static stress-strain traces of 3x3 bonded spherical roof contoured panels.

A summary of the mechanical properties of bonded and unbonded samples is presented in Figure 4.19. This part of study investigates the influence of varying the thickness of the cell wall on the crushing behaviour of bonded and unbonded contour core structures. Figure 4.19(a) & (b) shows the variation of strength and stiffness of the GFRP and CFRP contoured cores as a function of wall thickness. An examination of the figure indicates that the specific strength increases rapidly with wall thickness. The specific strength of the 1.5 mm contoured core being roughly four times that of the 0.5 mm thick structure. Similarly to Rejab and Cantwell [7] a comparison was carried out between the bonded and unbonded samples. These comparisons indicate that there is a negligible effect of bonding on the compression strength of the structure. Whereas, the stiffness is much higher for the bonded sample as compared to

the unbonded one. For example, the stiffness of the unbonded CFRP contoured panel with a cell wall thickness of 1.5 mm is 40 MPa, whereas that for its bonded counterpart is almost 95 MPa. These stiffnesses were calculated from the gradient of the linear part of stress-strain traces. This increment in stiffness is associated with the structural stability, which is related to the bonding between the core and skins during the crushing process.



(a) GFRP



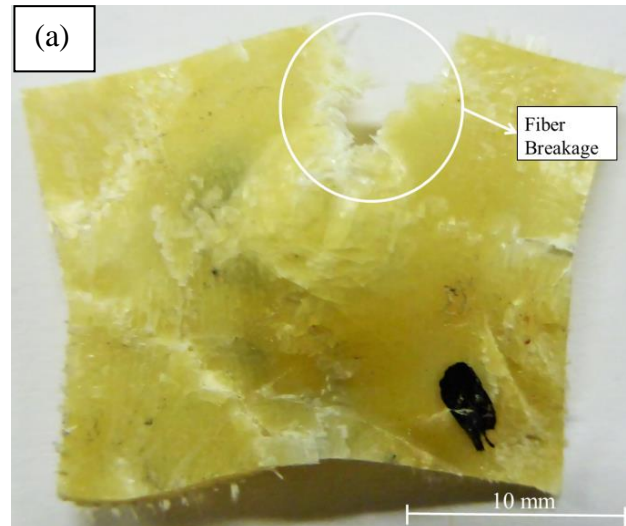
(b) CFRP

Figure 4.19 Comparison of the compression strength and stiffness properties as a function of cell wall thicknesses of the 3x3 spherical roof contoured panels.

4.6 The effect of varying the number of unit cells

It is expected that the performance of the multiple unit cells should reflect a more accurate response than a single cell system. In order to investigate this, tests were undertaken on samples based on (1x1), (2x2) and (3x3) cells on bonded and unbonded samples. During compression of a (1x1) unit cell, the collapse process was initiated by sliding of the bottom edges of the unit cell on the platen. This is due to the fact that the unit cell is cut and separated from a contoured sheet, and is free to stretch on platen. The unit cell was flattened with fibre fracture, as shown in Figure 4.20 (a). Fibre fracture was also observed during the compression response of the (2x2) and (3x3) cells. From the experimental observations of the GFRP structures, the matrix

was cracked with fibre splitting on dome region and in the area between the unit cells. Similar damage was observed in the CFRP core, Figure 4.21 (a) and (b). This damage behaviour is attributed to the restraining effect, which increases the structural rigidity due to the presence of the neighbouring cells connected to each other in the (2x2) or (3x3) cells. The effect of varying the number of unit cells on the compression strength of the CFRP and GFRP cores is shown in Figure 4.22 (a) and (b). These results highlight the influence of the connected neighbourhood cells on the collapse properties. An examination of the figure indicates that the compression strength increases rapidly with increasing number of unit cells, with the compression strength of the (3x3) core being roughly three times that of the (1x1) unbonded core parts. This difference decreases for the bonded counterparts.



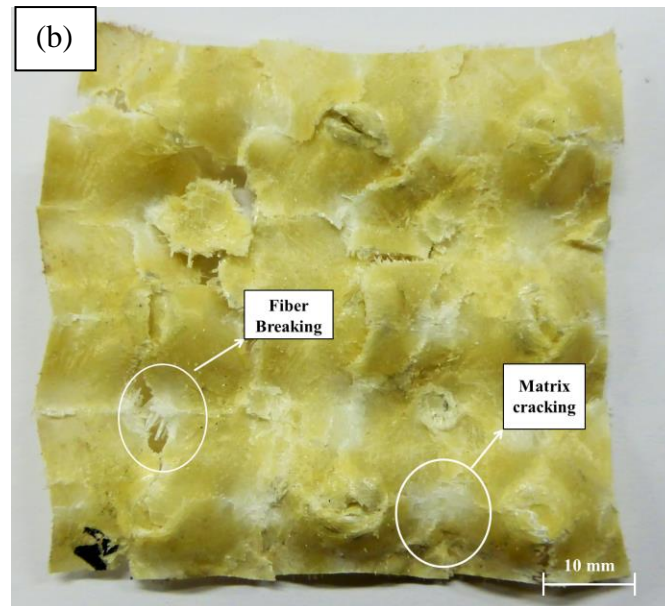
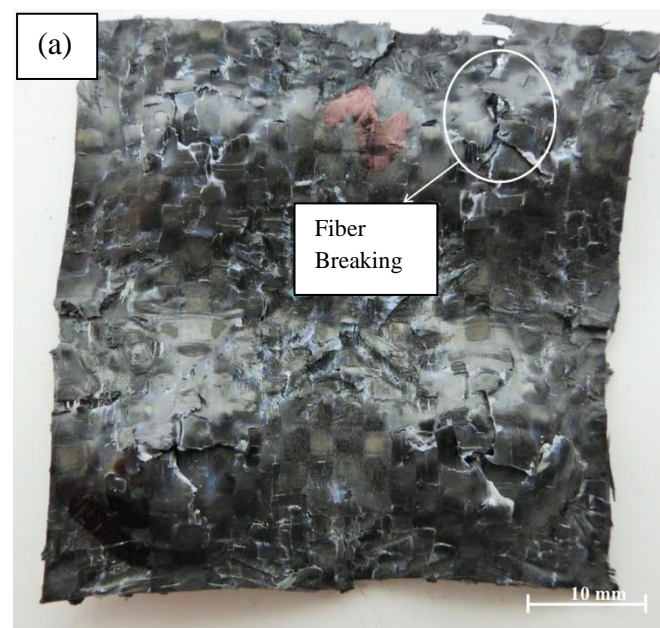


Figure 4.20 Photograph of damage in GFRP samples based on (a) (1x1) and (b) (3x3) unit cells.



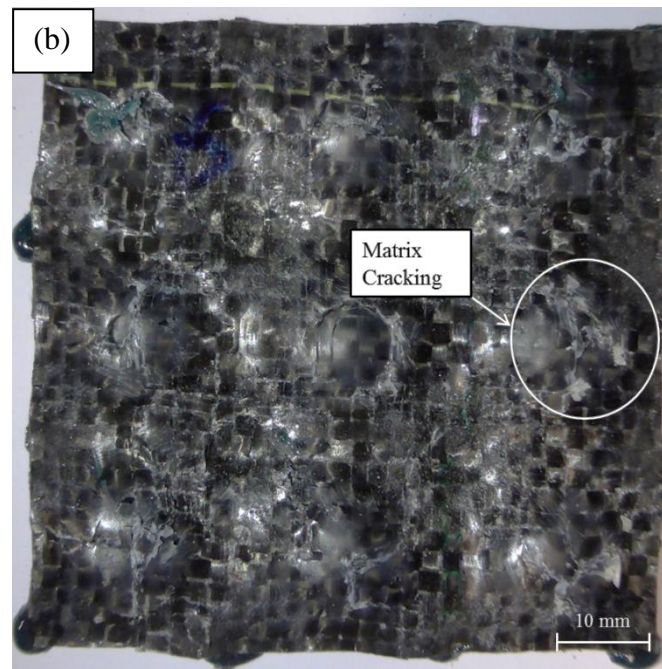
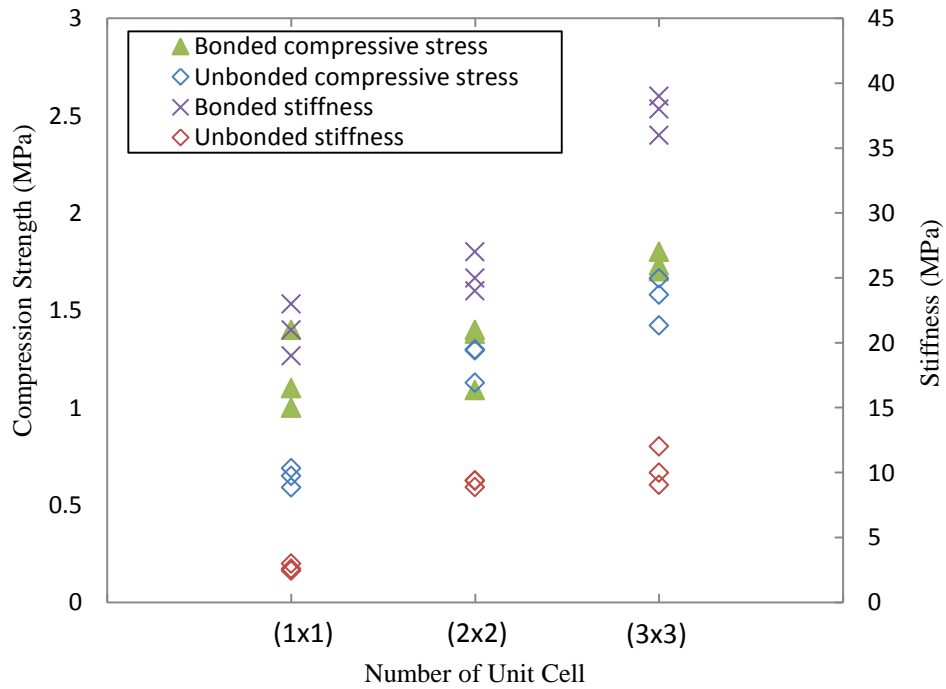
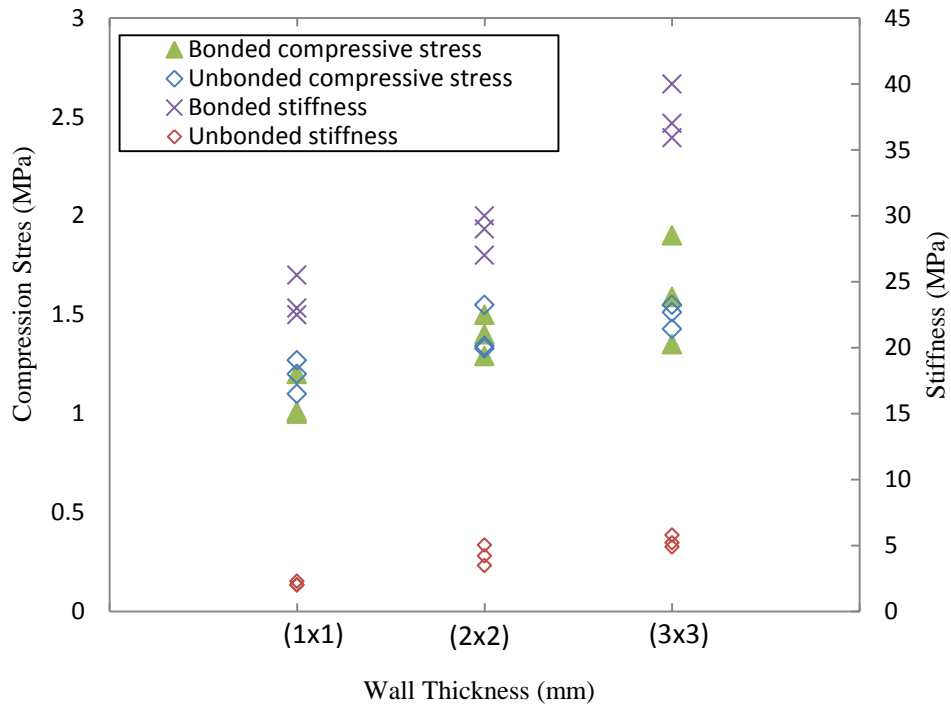


Figure 4.21 Photograph of damage in CFRP samples based on (a) (2x2) and (b) (3x3) unit cells.



(a)



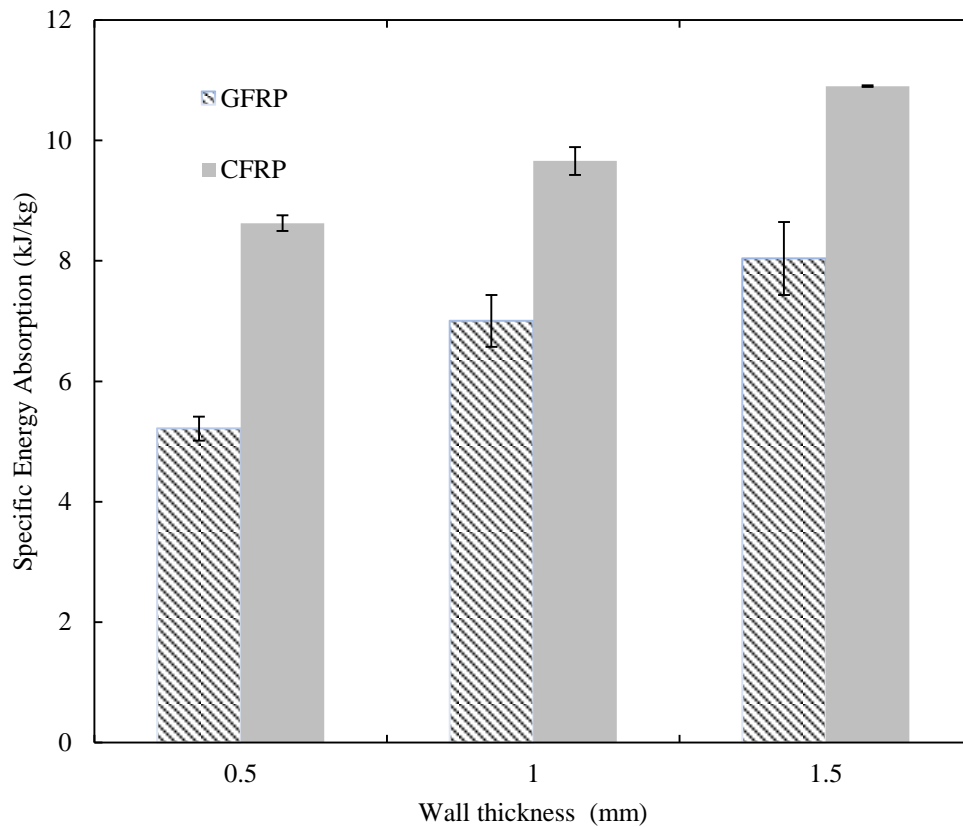
(b)

Figure 4.22 Compression strength and stiffness responses to the different number of unit cells for (a) GFRP (b) CFRP.

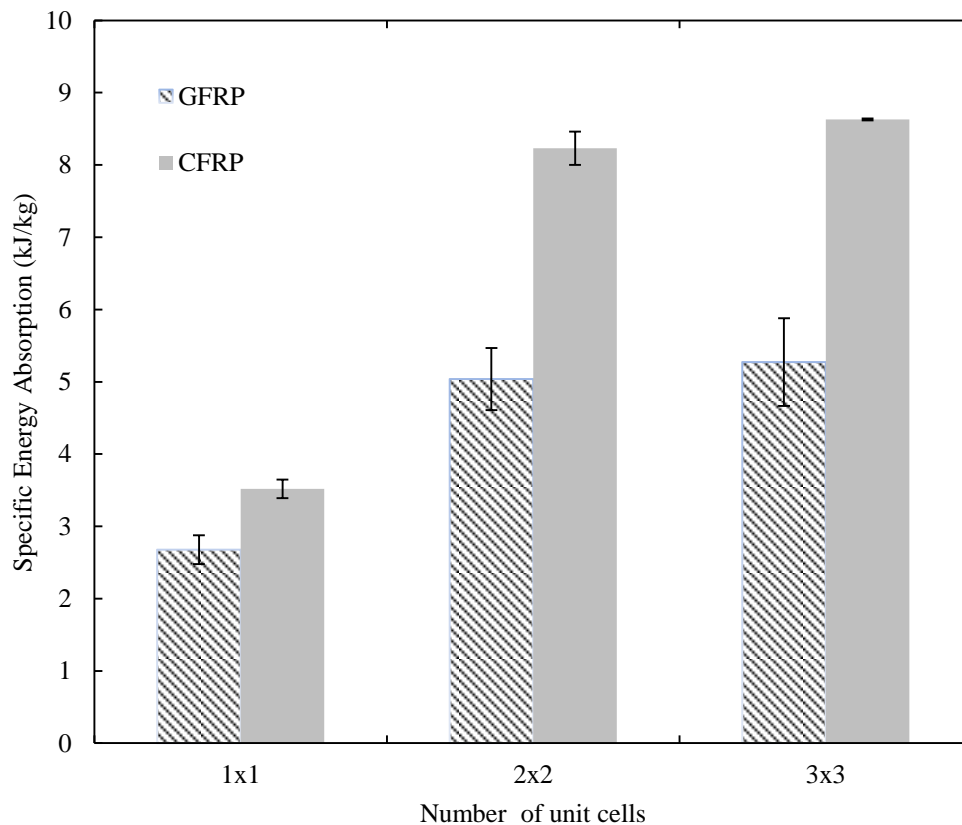
4.7 Energy absorption

The calculated energy absorption per unit mass of the CFRP and GFRP contoured structures are listed in Table 4.2, taking the average of three tests for each configuration. Figure 4.23 (a) and (b) show the variation of the specific energy absorption (SEA) capacity with the number of unit cells and cell wall thicknesses for both the CFRP and GFRP samples respectively. The specific energy absorption increases with the unit cell wall thickness and the number of unit cells as expected. However the former shows an almost linear increase, whereas the latter increases in a non-linear manner, i.e. there is a significant increase on SEA from 1x1 to 2x2 unit cells, but from 2x2 to 3x3 unit cells the increase is insignificant. It is observed that the SEA was almost 20 to 30 % greater in the CFRP than that in the GFRP with increased

number of unit cells. It is also clear that the CFRP outperforms its GFRP contour core structure by approximately thirty five percent. For example, the average SEA value of the 1.5mm CFRP wall thickness is 10.90 kJ/kg, whereas that for the equivalent GFRP is 8.04 kJ/kg. The fractured specimens were observed under a microscope in Figure 4.24 (a) and (b), where cracks and surface translucent effects were observed in both the GFRP and CFRP cores. The progressive crack growth absorbs energy, contributing to energy absorption in these structures.



(a)



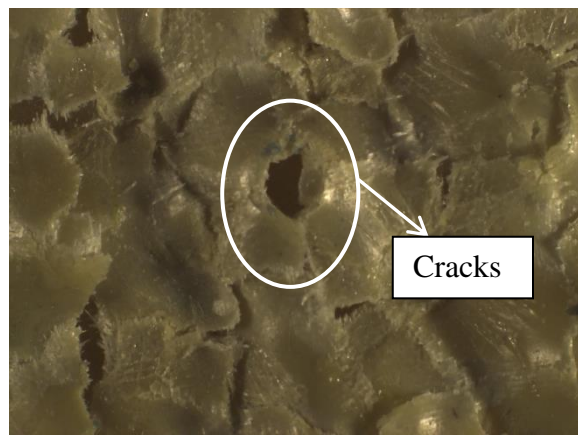
(b)

Figure 4.23 Comparison of Energy absorption of GFRP and CFRP as a function of (a) Cell wall thicknesses and (b) Number of unit cells.

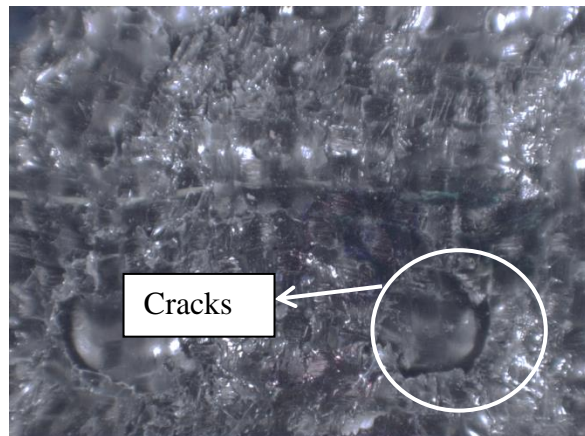
Table 4.2 Properties and characteristics of the contour core structures.

Material	No. of Unit Cell	No. of plies	Average wall thickness (mm)	Mass (g)	Average SEA (kJ/kg)
GFRP	1x1	5	0.50	0.60	2.64
	2x2	5	0.50	2.23	5.03
	3x3	5	0.50	5.19	5.27
	3x3	10	1.00	10.30	7.08
	3x3	15	1.50	14.30	8.04

CFRP	1x1	2	0.50	0.51	3.72
	2x2	2	0.50	1.70	8.40
	3x3	2	0.50	4.26	8.80
	3x3	4	0.50	8.60	9.60
	3x3	6	1.50	12.50	10.90



(a)



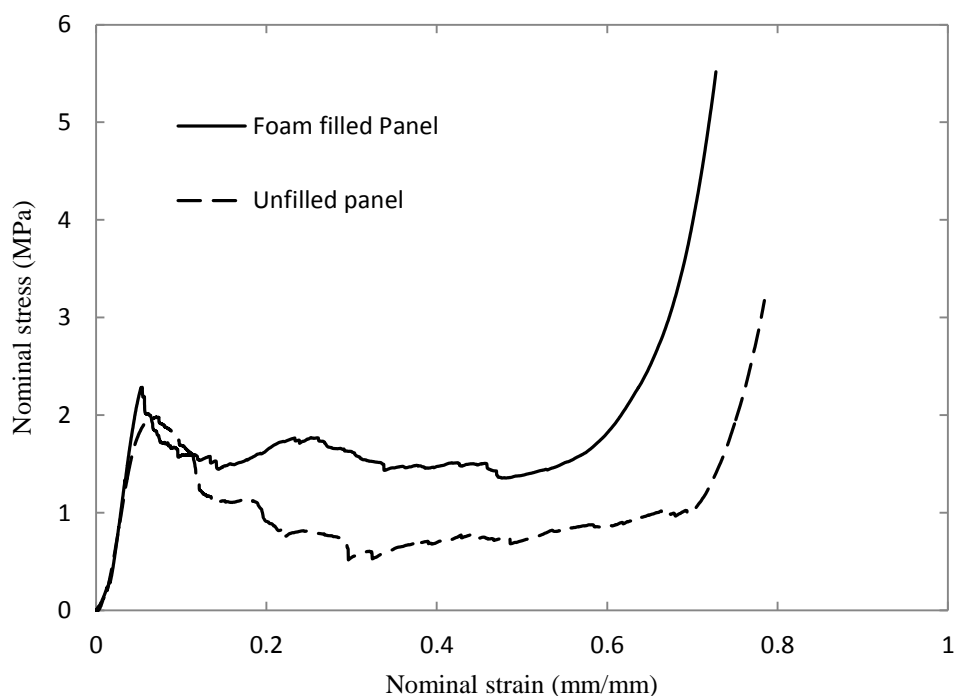
(b)

5 mm

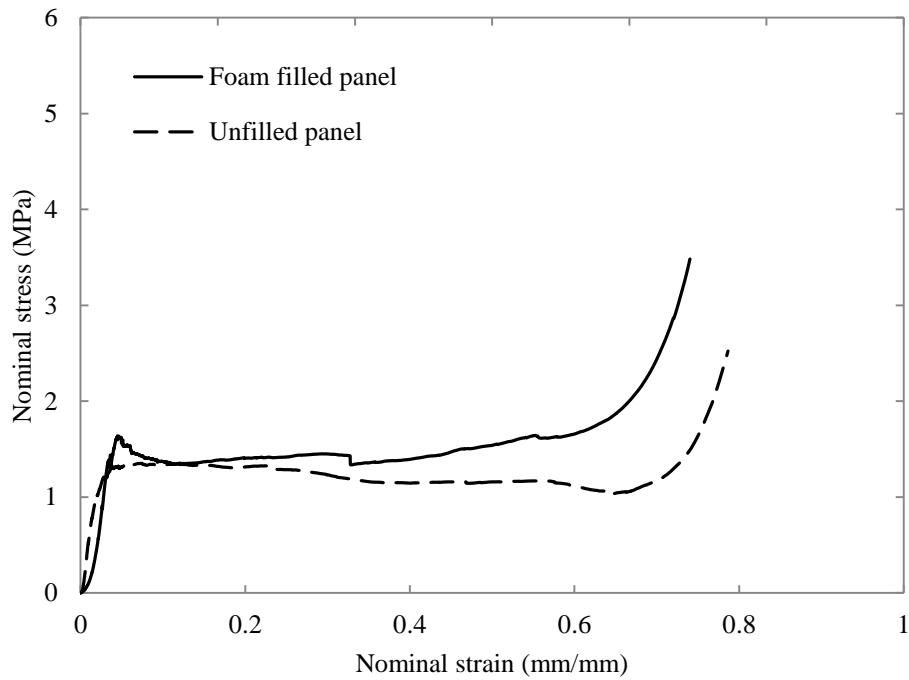
Figure 4.24 Stereo-microscopic images of the fractured surfaces of (a) GFRP (b) CFRP.

4.8 Compression on the foam filled spherical roof contoured panels

The stress-strain traces for the foam-filled and unfilled GFRP and CFRP spherical roof contoured panel for the cell wall thickness of 0.5 mm are presented in Figure 4.25(a) and (b) respectively. From those figures, it is clear that the contoured core sandwich structures filled with foam exhibit a slightly higher compression strength than their unfilled counterparts for both the GFRP and CFRP respectively. Similar to the flat roof panels, once again these spherical roof panels filled with foam offer a plateau stress that is double than unfilled GFRP counterparts, as shown in Figure 4.25 (a). The difference in these values was insignificant for the CFRP system, Figure 4.25. Following the plateau stage, all of the contoured panels finally reached the densification threshold, however a delayed densification point was observed in the unfilled panels.



(a) GFRP



(b) CFRP

Figure 4.25 Stress-strain traces on foam filled 3x3 spherical roof contoured panels.

4.9 Fracture modes

To correlate the collapse response with the failure mechanisms in the cores, interrupted compression tests were carried out on 1.0 mm thick cell wall of CFRP and GFRP spherical cores with a 3 x 3 cell number. The tests were interrupted at key places, where a significant deformation of the collapse curve was visible.

4.9.1 Failure of the CFRP core

As explained before, the testing process was interrupted to observe the crack initiation and propagation mechanism in the compressed specimen. The core that was tested had nine uniform spherical top domes, with the same number of spherical bottom domes.

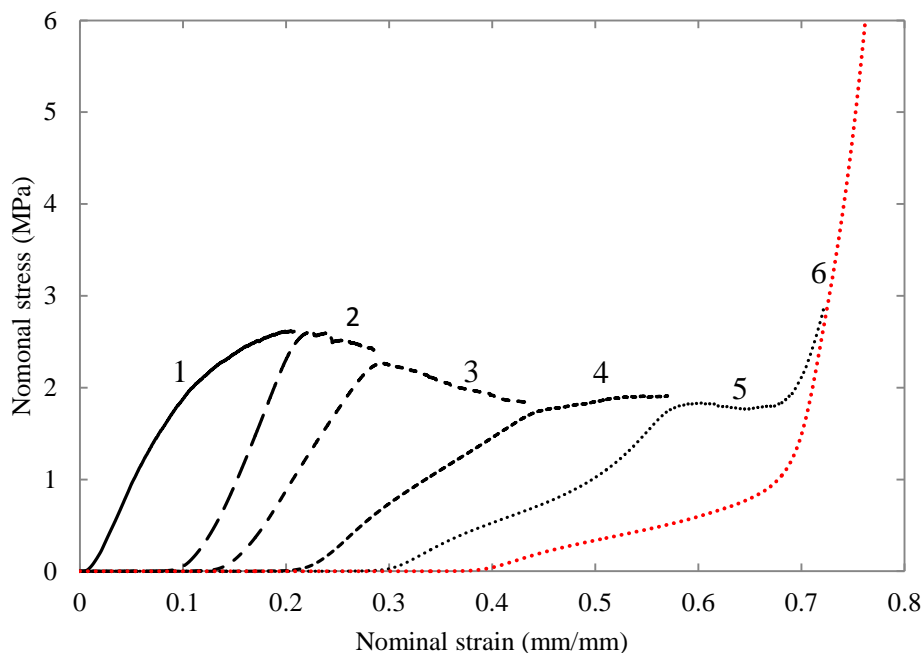


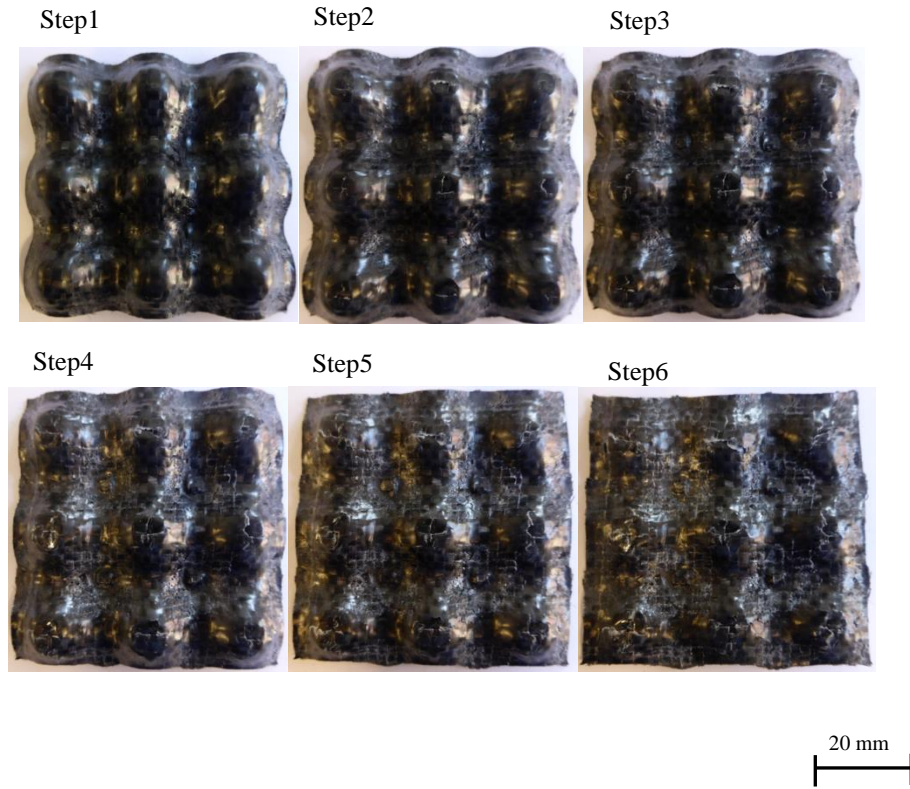
Figure 4.26 Step-wise collapse response of the 3x3 CFRP spherical core.

During the compression process, the aluminium platens of the compression machine first came into contact with the top domes and start to crush the core. The traces in Figure 4.26 and the fracture surfaces in Figure 4.27 suggest that a large initial stress started to flatten the top and the bottom domes at the same time.

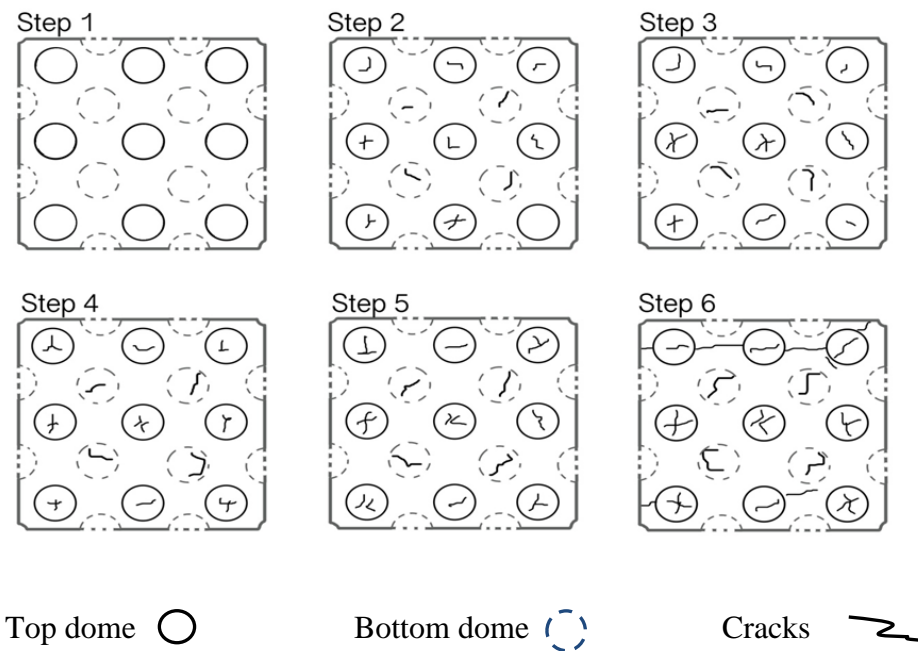
In Step 2, it was shown that crack formation (mainly fibre breakage and matrix cracking) occurred only in the dome regions. These cracks propagated along the curved areas between the domes on the next step of compression process. Similar crack formation in composite domes is discussed in [118] for a thin-walled hemispherical shell. The Stress-strain trace begins to drop after the initial peak in Step 2. Here, cracks were visible that propagated slightly.

After the 2nd interruption (Step 2), there was a reduction in the peak stress and visual inspection showed that the cracks grew from the flattened dome to the curved region.

After the strain of 0.3 (Step3), the stress value dropped 25% of peak stress. At the strain of 0.4, the middle top dome showed a larger flattened diameter than the previous steps. This may have resulted from the rigidity of the mid-dome caused by the neighbouring unit cells, which did not allow it to stretch freely like the domes on the edges. Since the movement of the mid-dome was restricted by the adjacent unit cells and that caused extra stress in the mid-dome. The remaining tops showed cracks propagating in the transverse direction towards the curved region. Finally, the collapse curve reached the densification threshold.



(a) Images of CFRP



(b) Schematic diagram

Figure 4.27 Summary on the fractured surfaces of spherical-roof core.

4.9.2 Failure of the GFRP core

The Specimen used in this compression test was similar to the CFRP specimen. It also contained nine tops and bottoms. It was loaded in the same manner to identify any similarities between the two samples. The test was interrupted at different points to identify visual failure within the specimen.

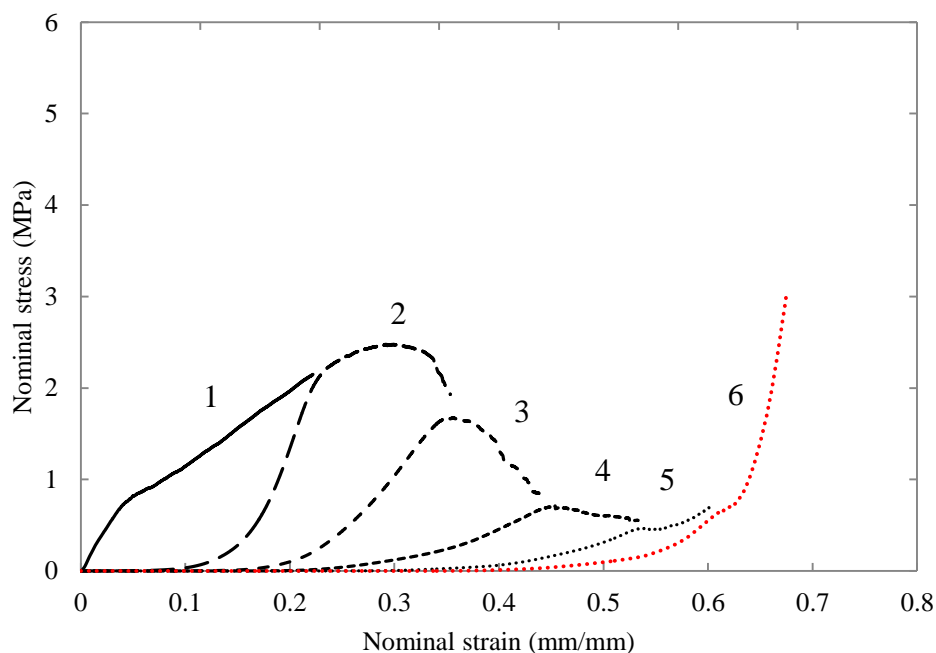
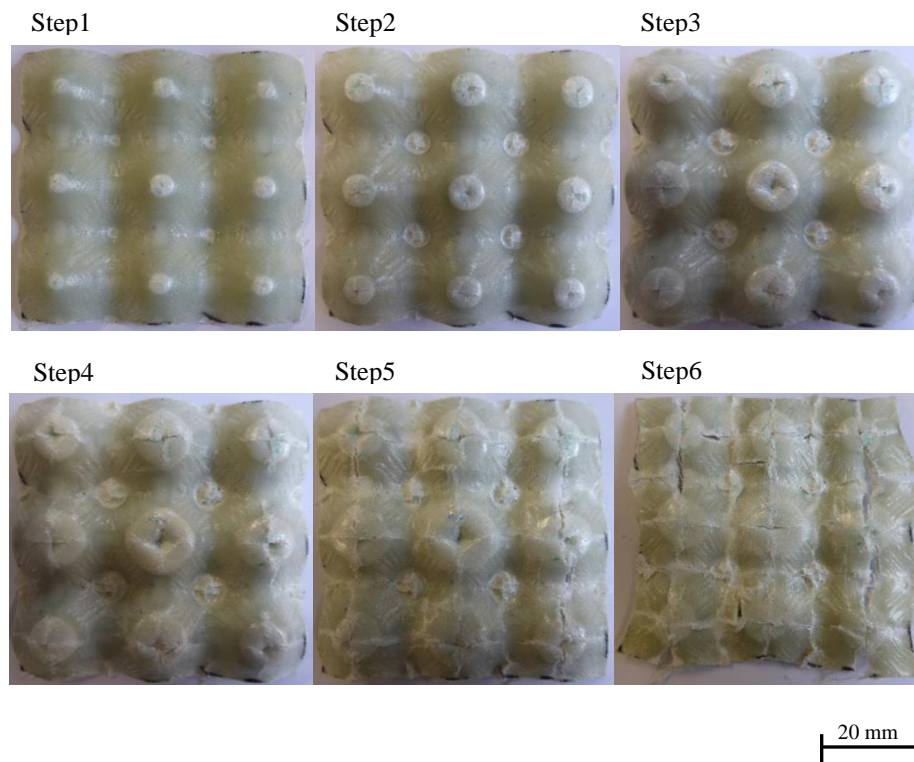


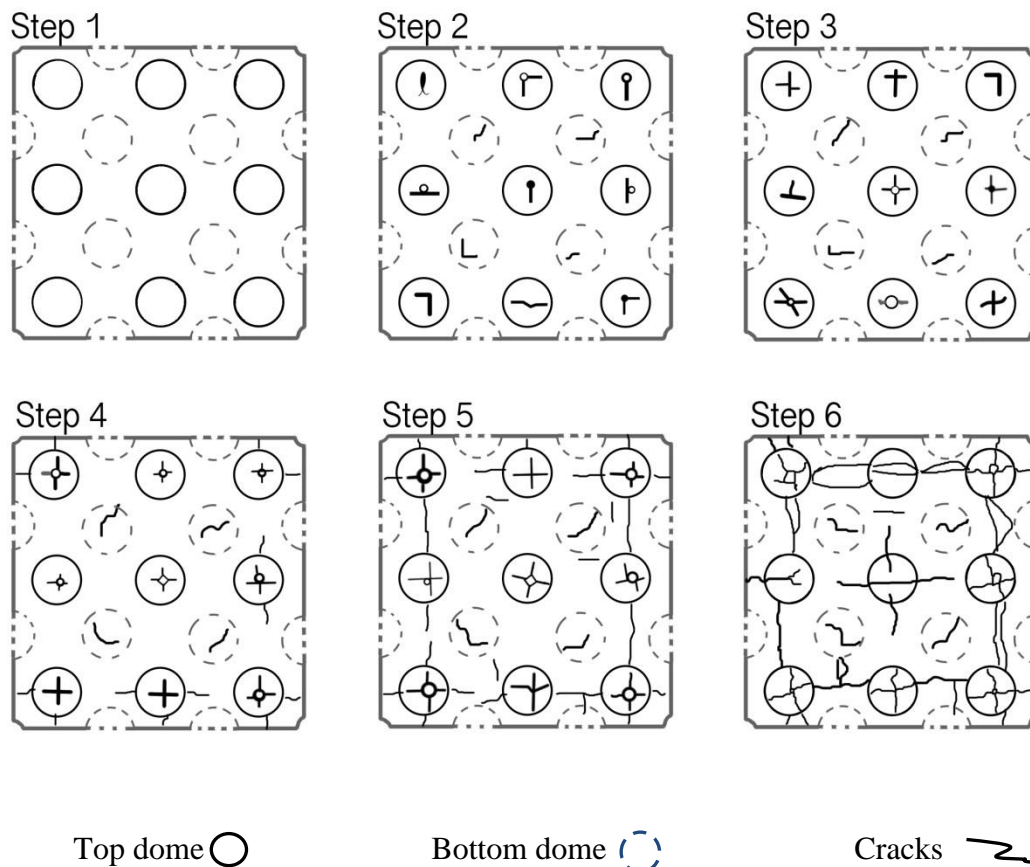
Figure 4.28 Step-wise collapse response of 3x3 GFRP spherical core.

At the first interruption of the displacement shown in Figure 4.28, it is evident in Figure 4.29 that the tops and bottoms were flattened along with cracks on its surface. However, with further loading it was observed that the failure mode is similar to the CFRP specimens, which is shown schematically in Figure 4.29. The next interruption clearly indicated that the cracks progressively grew in the same direction as before, but it showed a much larger flattened area on mid-dome. This scenario may be due to the movement restriction by the neighbourhood unit cells.

As explained before, the initial interruption did not show any cracks other than the flattened domes. The second interruption showed small cracks as it would appear to be the early stage of the failure process. After the 3rd interruption (Step 3) the cracks were clearly visible, which propagated throughout the spherical domes. After this peak, it drops rapidly which was caused by the failure of the curved region of the structure, Figure 4.28. However, in the stage of failure corresponding to the Step 5, the middle dome was experienced with a hole caused by the inward material dimpling due to continuous failure of the structure. Finally, the curve exhibits a densification threshold, where the structure is completely failed along with matrix cracking and fibre breakage.



(a) Images of GFRP



(b) Schematic diagram of GFRP

Figure 4.29 Summary on fractured surface of spherical roof core.

4.10 The Compressive behaviour of spherical roof contoured panels at high strain rates

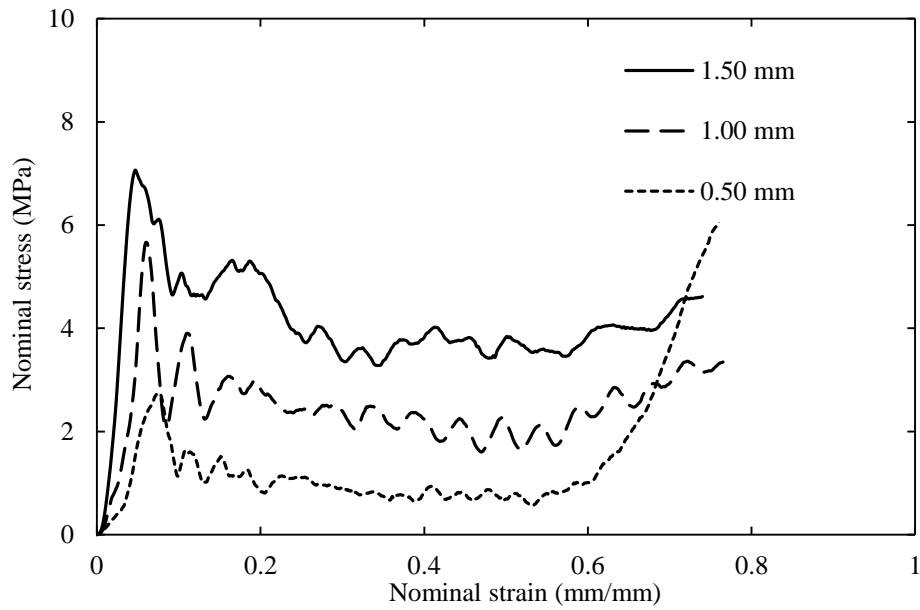
Crush tests at a high strain rate were performed using a drop-weight impact tower. A flat rectangular impactor, with dimensions of 120 mm x 80 mm was raised to a predefined height to obtain the required impact energy. Table 4.3 shows the setup-parameters used to test the spherical roof contoured panels.

Table 4.3 Test values used to test the spherical roof contoured panels.

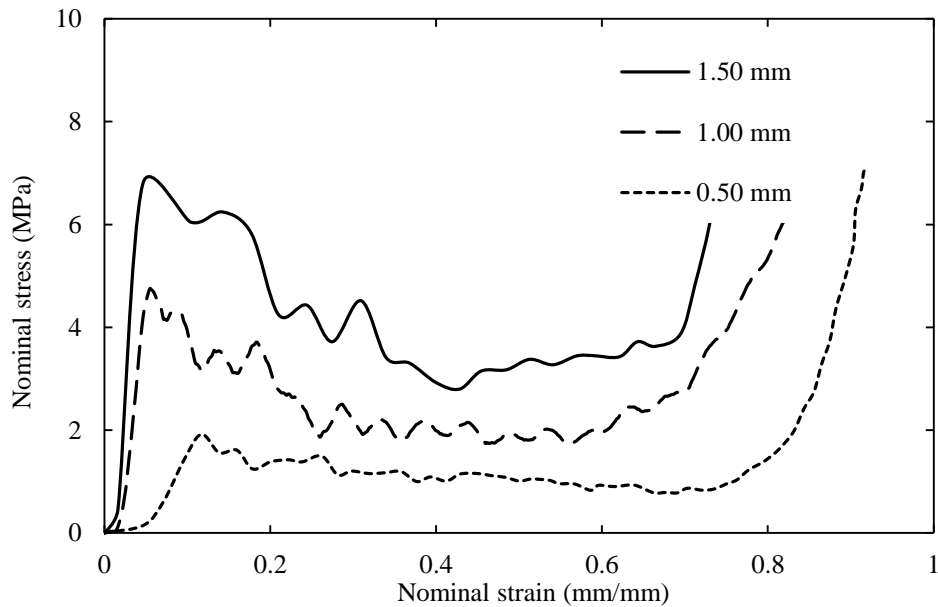
Material	Specimen cell wall thickness (mm)	Drop height (m)	Impactor mass (kg)
CFRP	0.5	0.30	15.70
	1.0	0.71	13.62
	1.5	1.07	15.70
GFRP	0.5	0.30	13.62
	1.0	0.67	13.62
	1.5	1.00	13.62

Figure 4.30 shows stress-strain traces following drop-weight impact tests on the spherical contoured sandwich panels as a function of cell wall thickness. Similar to flat roof structure, in the spherical panels the stress oscillates until the densification point for all the panels. However, this oscillation becomes more pronounced in the GFRP panels. The compressive stress and plateau stress of 1.5 mm thick GFRP panel was about three times that of the 0.5 mm thick cell wall sample. This difference is even more pronounced in the CFRP panels, e.g. the compressive strength of the 0.5 mm cell wall panel is 1.9 MPa, whereas it is 6.7 MPa for the 1.5mm thick cell wall. Figure 4.30 (a) and (b) indicate that the GFRP spherical roof panels exhibit slightly higher initial peaks than their CFRP counterparts. This difference may be associated with the lower fibre volume fraction of CFRP (nominally 47% and 60% for GFRP), though carbon fibres are stronger and stiffer, which may cause an initial strengthening of the structure, resulting a relatively high initial peak than that in the CFRP traces. Moreover, after an initial rise, the stress drops rapidly, before continuing on a roughly

constant plateau (between strains of 0.1 and 0.8) between the first peak and the densification threshold.



(a) GFRP



(b) CFRP

Figure 4.30 Dynamic compression tests on 3x3 spherical roofed panels.

The SEA of the spherical roof core structures was determined and the resulting values of dynamic specific energy absorption are compared with the quasi-static values in Figure 4.31. Here, it is clear that the dynamic SEA values are higher than the quasi-static data, highlighting a rate-sensitive response. For example, the average SEA value for the 1.5 mm thick CFRP panel under dynamic loading was approximately 11.28 kJ/kg, compared to 10.90 kJ/kg in the quasi-static test. These differences are even greater for the GFRP structures, with a dynamic value of 9.7 kJ/kg which is over twenty percent greater than its quasi-static counterpart.

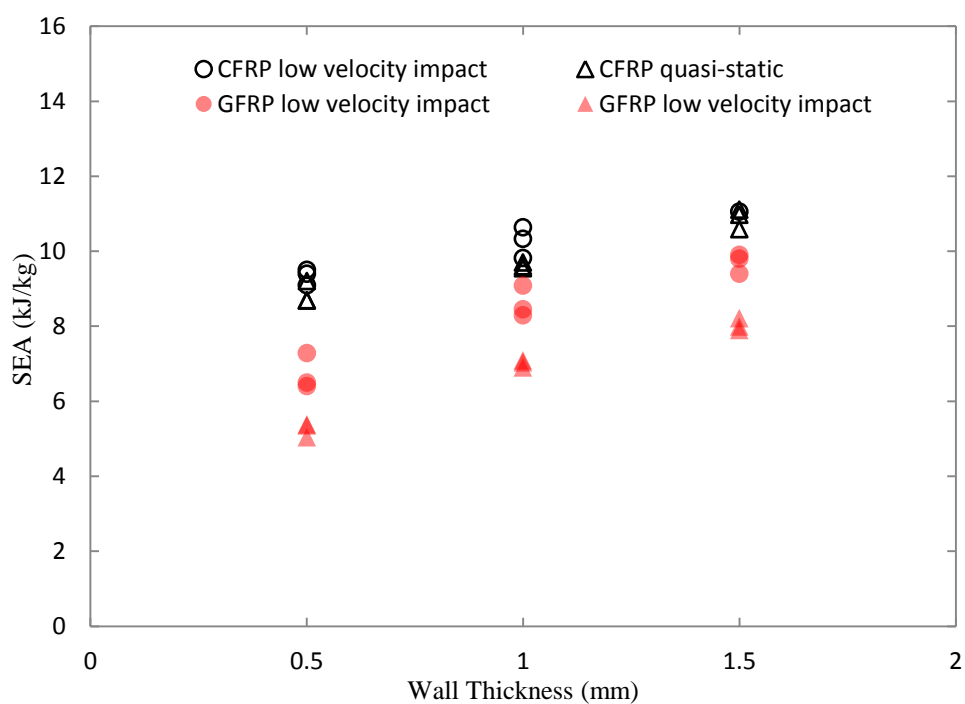


Figure 4.31 Specific energy absorption of the 3x3 spherical roof contoured structures made of CFRP and GFRP.

4.11 Blast tests

Blast tests were conducted on sandwich panels based on the CFRP and the GFRP spherical roof contoured cores with aluminium alloy face sheets. The impulse was obtained from the measured swing of the blast pendulum, typically ranging from 13 to 27 Ns, depending upon the charge mass. Table 4.4 shows the calculated parameters related to blast loading. The level of crush in the contoured parts increases with applied impulse. Figure 4.32 shows the degree of crushing with applied impulse, for both the CFRP and the GFRP panels. A similar explanation is presented on lattice sandwich panels [119]. The level of crush increases nonlinearly with increasing impulse. It is clear that a higher impulse is required to generate a given level of crush in the CFRP panels. For example, the impulse required to achieve 50% crush in CFRP contour is 22.9 Ns, whereas the equivalent impulse resulted in 70% crush in its GFRP counterpart. Following blast testing, dimpling was observed on the individual spherical caps of the GFRP panel, whereas only fibre fracture was observed in the CFRP counterparts. It is believed that the aforementioned dimpling on the spherical-roof GFRP panels occurred due to the local buckling and post-buckling deformation mechanisms. The failure strain in the CFRP system was lower and failure therefore occurred before significant buckling and the spherical caps of the core were punched-out, Figure 4.33(b). Similar failure modes were also observed in the other panels subjected to different levels of impulse.

Table 4.4 Details of blast pendulum.

Mass of explosive (gram)	Pendulum horizontal swinging measurements (x_1, x_2)(meter)	Damping constant (β)	Initial velocity of the pendulum \dot{x}_0 (m/s)	Impulse (Ns)
6	(0.069, 0.065)	0.0287	0.129	13.12
8	(0.092, 0.083)	0.055	0.177	18.02
10	(0.118, 0.113)	0.029	0.224	22.75
12	(0.136, 0.124)	0.054	0.263	26.68

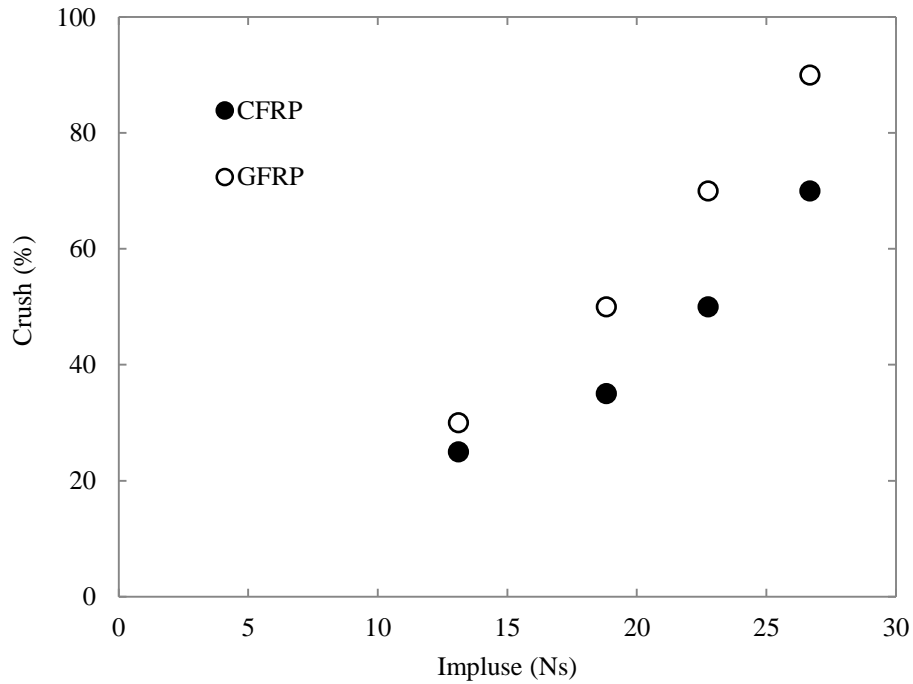
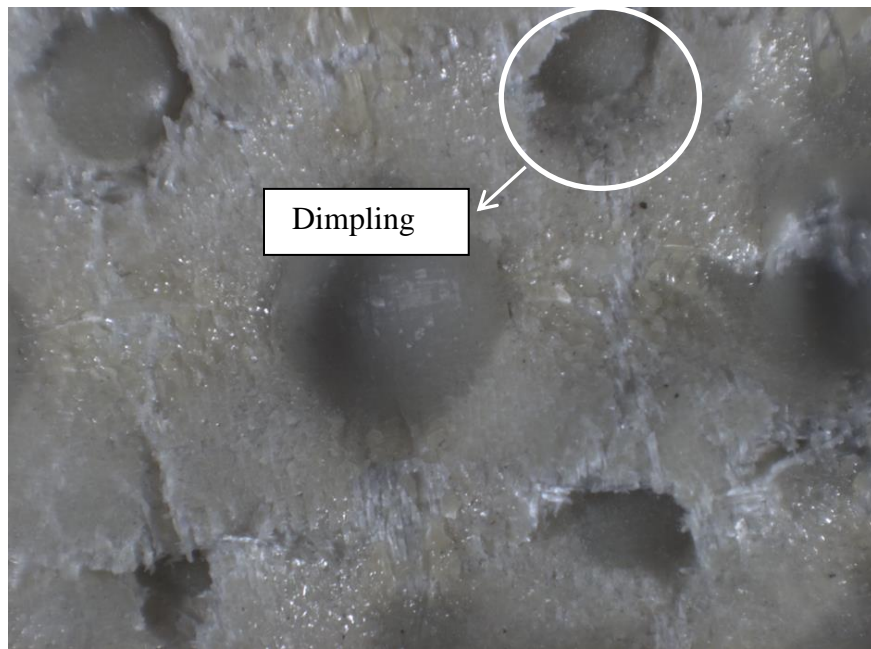
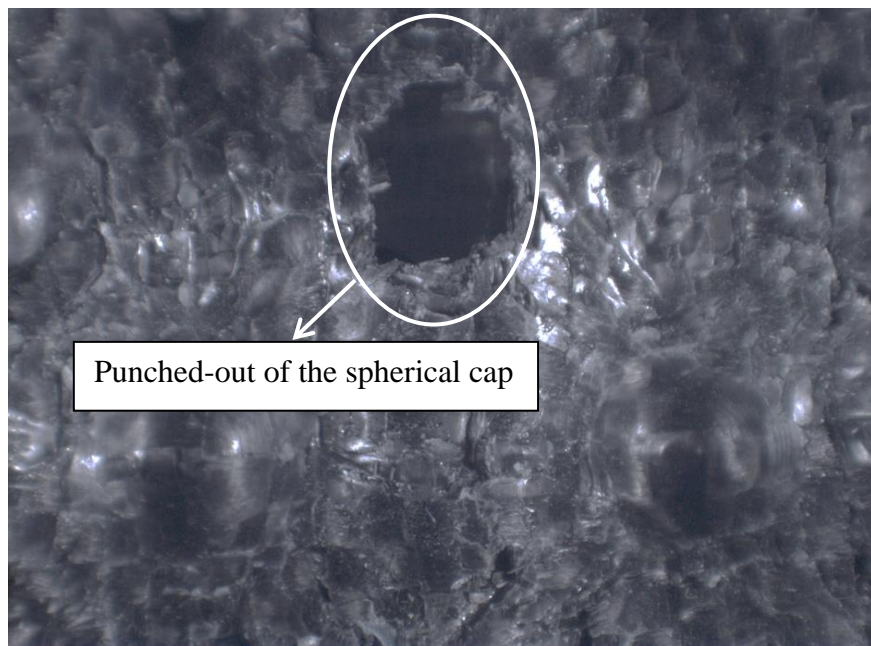


Figure 4.32 Percent crush versus applied impulse for the spherical roof contoured sandwich panels.



(a)



(b)

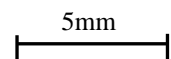


Figure 4.33 Blast load deformation on 10 gram mass of explosives (a) GFRP and (b) CFRP.

4.12 Comparison of the current contoured core panels with other energy-absorbing cores

The egg-box panels presented in references [18] and [71] are the same in geometric design and dimension as in flat-roof contoured core panels. The properties of composite materials used in composite egg-box panels [18] are almost similar as used in current research work. Therefore, the SEA of the current contoured panels was compared with bonded aluminium egg-box [71] and the best energy absorbing systems from the reference [18], and the results are summarised as a function of mass in Figure 4.34. In general, the spherical-roof panels offer excellent energy absorbing capacities, with values being up to ten times greater than the corresponding aluminium egg-box panels. Further, the spherical-roof panels are 50 to 60 percent better than the existing composite egg box panels in terms of SEA. As expected, the SEA values of the flat-roof contoured panels are almost close to the ones obtained from composite egg-box panels [18].

Relative to the other panels, the higher energy absorption capacities of these spherical-roof contoured panels are likely to be associated with the progressive failure mechanisms of the fibre and matrix in the cap region. Chung et al [48] observed that initial cracking in egg-box panels occurred at the circular perimeters of the upper and lower surfaces that are in contact with the plates/skins, as a result of local stress concentrations. However, no such regions of weakness exist in the spherical-roof, which may explain the great improvement in structural performance. In addition, reducing the inner peak distance and the cell diameter gives a high density of cones throughout the structure which results in an increased stiffness, hence, a higher stress

level, which in turn improves the energy absorption capability of the spherical-roof contoured panels.

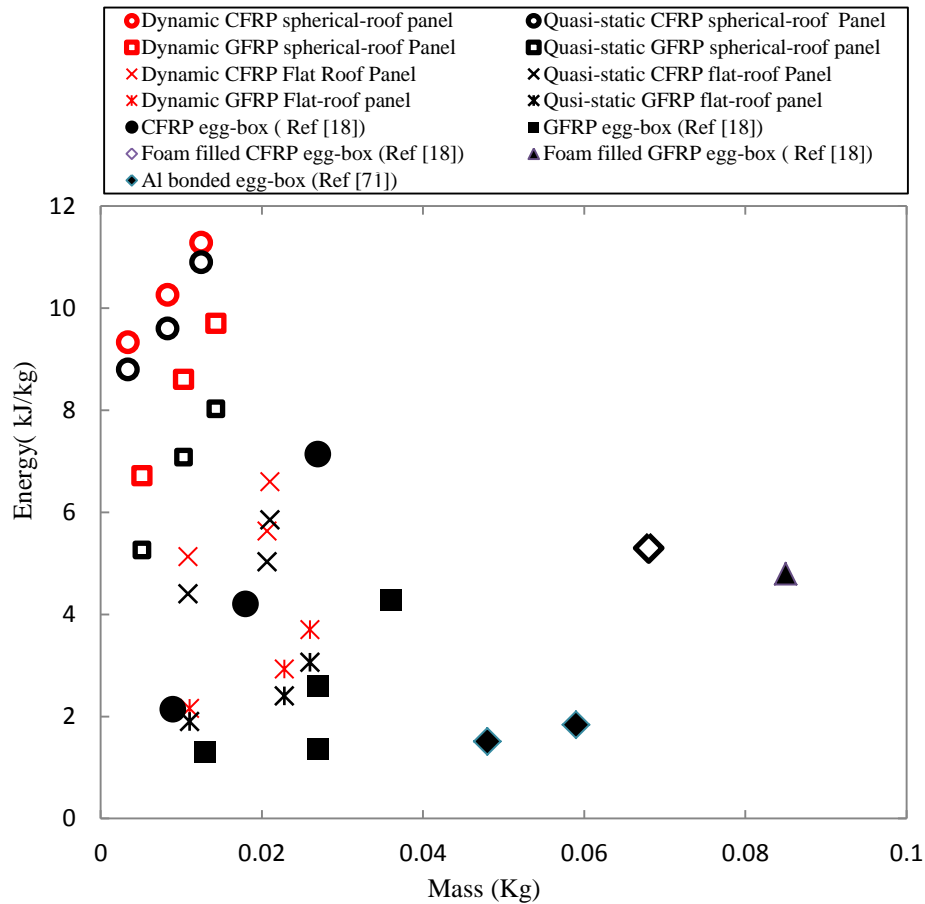


Figure 4.34 Energy absorption per unit mass of the current panels and data from the literature.

Figure 4.35 compares the energy absorption per unit mass, but in this situation as a function of the peak stress of contoured panels. This determines the performance of contoured panels, where not just the amount of energy to be absorbed is shown, but also a peak stress. Again a similar outcome has been shown with the superior performance of spherical-roof contoured core in terms of peak stress vs SEA. It is clear from the figure that increasing thickness reflects an increment in both SEA and peak stress, so that the choice of the optimum core depends on the commercial requirements between these two parameters of contoured cores.

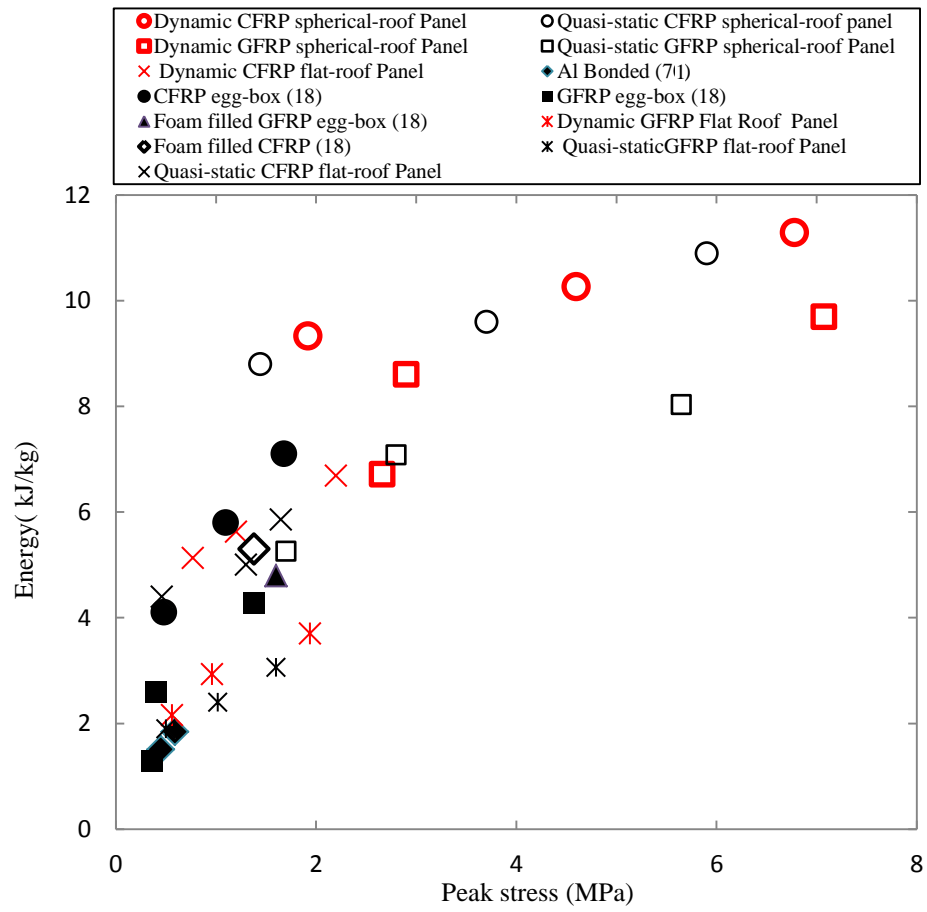


Figure 4.35 Energy absorption per unit mass as a function of peak stress.

Summary of the chapter

The experimental results of the GFRP and CFRP contoured-core materials have been presented and discussed in Chapter 4. Initially, the mechanical properties of the materials under tension were characterised. The responses of the flat roof contoured specimen under quasi-static compression and low impact loading were examined and explained. A number of factors on their static and dynamic properties have been observed on flat-roof structures, such as the material effect, cell wall thickness, edge constraint, and strain-rate as well the skins effect. Thereafter, the data for the spherical contoured-core sandwich specimens under quasi-static, low velocity impact and blast loading were given and the failure mechanisms were discussed in detail. Here, with increasing cell wall thickness, the compressive stress increased significantly. It was evident that stress-strain plot of the GFRP dropped more rapidly after the initial peak than the CFRP structures for all the thicknesses. This sudden drop in the traces was associated with brittle failure in the GFRP in comparison to its counterparts. The effects of bonded skins have also been examined, where the stiffness was much higher for the bonded sample as compared to the unbonded one.

Energy absorption of those structures was also calculated under quasi-static and dynamic loading. The specific energy absorption was increased with the unit cell wall thickness and the number of unit cells, as expected. Following blast testing, dimpling and fibre fracture was observed on the individual spherical caps in the GFRP roof structure and its CFRP counterparts. The performance of these panels was compared with similar existing designs such as egg box panels based on aluminium, GFRP and CFRP. It was shown that the current composite designs offer excellent levels of energy absorption per unit mass, in relation to other types of egg box structures.

Chapter 5. Finite element modelling

5.1 Introduction:

The finite element (FE) analysis and techniques considered in modelling the response of contoured structures subjected to quasi-static compression and low velocity impact loading are presented. The FE modelling results are verified and compared with the experimental results previously presented in Chapter 4. A summary is placed at the end of this chapter to highlight the main findings.

5.2 Constitutive model

Various constitutive models were employed to simulate the mechanical response of the novel contoured core structures. Here, two composite materials are considered, these being GFRP and CFRP. The contoured cores exhibit fibre and matrix fracturing modes, during compression. Given these responses, constitutive models are required to predict their respective behaviour. The material models described below were implemented in ABAQUS/Explicit and the stress-strain responses and the associated failure modes were predicted.

5.2.1 Contoured composite

Modelling the failure behaviour of composite materials is a very complex process due to factors such as the variation of fibres and matrices, types of ply for instance unidirectional or fabrics and orientation ply angle [120]. Thus, currently there are no universally accepted material constitutive models for crash simulations of composite materials. A comprehensive literature review on the classification of composite crushing models is explained in Chapter 2.

In this study, the composite cores are based on 5, 10 and 15 plies, consisting of all composite layers with the core thicknesses of 0.5mm, 1.0mm and 1.5 mm, for GFRP model.

CFRP cores having similar thicknesses were modelled by placing 2, 4 and 6 woven sheets. The composite response is dependent on the number of layers and loading direction applied. With reference to this information, it is required to model contoured core layers of carbon and glass fiber prepreg in order to simulate the overall response of the contoured cores subjected to compression. Table 5.1 presents the elastic properties of carbon fibre/epoxy and glass fibre/epoxy composite used in the FE analysis.

The cores were modelled as orthotropic elastic materials up to the on-set of failure, followed by damage evolution described by Hashin's failure criteria for laminate [121]. The failure model is related to brittle properties which degraded by fracture and cracking. A key assumption here is that the material properties were based on carbon and glass prepreg laminates, where the fibre and resin constituents were not considered separately.

Table 5.1 Summary of the elasticity properties of the carbon and glass fibre/epoxy materials [7, 122, 123].

Symbol	Carbon fibre/epoxy	Glass fibre/epoxy	Parameters
ρ [kg/m ³]	1390	1750	Density
E_1 [GPa]	48	23	Young's modulus in fibre direction
E_2 [GPa]	48	23	Young's modulus in transverse to fiber direction
E_3 [GPa]	5	1	Young's modulus in thickness direction
G_{12} [GPa]	9	5	In-plane shear modulus
G_{13} [GPa]	9	5	Interlaminar shear modulus
G_{23} [GPa]	3.7	3.5	Interlaminar shear modulus
ν_{12}	0.15	0.1	Major in-plane Poisson's ratio
ν_{13}	0.15	0.1	Interlaminar Poisson's ratio
ν_{23}	0.27	0.28	Interlaminar Poisson's ratio

5.2.2 Damage model for the fibre-reinforced composites

The progressive damage models for composites are based on combination models from the degradation of the stiffness matrix coefficients [124] before failure at a material point based on four damage initiation mechanisms [121, 125]. This is followed by damage propagation in the post-damage phase, based on the evolution law of the damage variable [126].

Prior to damage initiation, the material stiffness is given by:

$$\sigma = C_d \varepsilon \quad (5.1)$$

where C_d is the damaged elasticity matrix, which has the form of:

$$C_d = \frac{1}{D} \begin{pmatrix} (1-d_f)E_1 & (1-d_f)(1-d_m)v_{21}E_1 & 0 \\ (1-d_f)(1-d_m)v_{12}E_2 & (1-d_m)E_2 & 0 \\ 0 & 0 & (1-d_s)D \end{pmatrix} \quad (5.2)$$

where $D = 1 - (1 - d_f)(1 - d_m) v_{12} v_{21}$, E_1 is the Young's modulus in the fibre direction, E_2 is the Young's modulus perpendicular to the fibre direction, d_f is the current state of fibre damage, d_m is the current state of matrix damage and d_s reflects the current state of shear damage.

The Hashin's damage model [121] consists of interaction of more than one stress components in evaluating failure modes. Hashin's damage initiation assumes that the response of the undamaged material is linearly elastic with the onset damage involving four failure modes. These modes are (i) fibre rupture in tension, (ii) fibre buckling and kinking in compression, (iii) matrix cracking under transverse tension and shearing and (iv) matrix crushing under transverse compression and shearing. By considering $\hat{\sigma}_{11}$, $\hat{\sigma}_{22}$ and $\hat{\tau}_{12}$ as the longitudinal, transverse and shear effective stresses, Hashin's damage initiation criteria take the general form as follows[121]:

a) Tensile fibre failure for ($\hat{\sigma}_{11} \geq 0$):

$$F_f^t = \left(\frac{\hat{\sigma}_{11}}{X^1} \right)^2 + \alpha \left(\frac{\hat{\tau}_{12}}{S^1} \right)^2 \quad (5.3)$$

b) Compressive fibre failure for ($\hat{\sigma}_{11} < 0$):

$$F_f^c = \left(\frac{\hat{\sigma}_{11}}{X^2} \right)^2 \quad (5.4)$$

c) Tensile matrix failure for ($\hat{\sigma}_{22} \geq 0$):

$$F_m^t = \left(\frac{\hat{\sigma}_{22}}{Y^1} \right)^2 + \left(\frac{\hat{\tau}_{12}}{S^1} \right)^2 \quad (5.5)$$

d) Compressive matrix failure for ($\hat{\sigma}_{22} < 0$):

$$F_m^c = \left(\frac{\hat{\sigma}_{22}}{2S^1} \right)^2 + \left[\left(\frac{Y^c}{2S^1} \right)^2 - 1 \right] \frac{\hat{\sigma}_{22}}{Y^2} + \left(\frac{\hat{\tau}_{12}}{S^1} \right)^2 \quad (5.6)$$

where, X^T and X^C denote the tensile and compressive strength components in longitudinal direction by superscripts T and C, respectively. Similarly, Y^T and Y^C denote the tensile and compressive strengths in transverse direction, S^L and S^T are the longitudinal and transverse shear strengths. Table 5.2 gives a summary of the damage initiation data for carbon fiber/epoxy and glass fiber/epoxy. In Equation (5.3), α is a coefficient that determines shear stress contribution to the fiber tensile damage initiation criterion.

Table 5.2 Summary of the damage initiation and fracture energy data of the carbon and glass fibre/epoxy materials [7].

Symbol	Carbon fibre/epoxy	Glass fibre/epoxy	Parameters
X^1 [MPa]	550	320	Tensile strength in fibre direction
X^2 [MPa]	150	260	Compressive strength in fibre direction
Y^1 [MPa]	550	320	tensile strength in transverse to the fibre direction
Y^2 [MPa]	150	100	compressive strength transverse to the fibre direction
S^1 [MPa]	120	100	In-plane Shear strength
S^2 [MPa]	120	100	Interlaminar Shear strength
G_{ft}^C [kJ/m ²]	42.7	110	Fibre tension
G_{fc}^C [kJ/m ²]	45.0	120	Fibre compression
G_{mt}^C [kJ/m ²]	42.7	110	Matrix tension
G_{mc}^C [kJ/m ²]	45.0	120	Matrix compression

Once the damage criteria are satisfied for all of the element integration points, a failed element was removed from the mesh and the element status in field output variable was set from one to zero. At this point, the stress of the element contributes no resistance to the model stiffness in the subsequent deformation. For a shell model, element deletion can occur from both tensile and compressive damage. In contrast, element deletion for solid model is only possible as a result of fibre tensile damage

[127]. A linear damage evolution law was specified in terms of fracture energy per unit area in the numerical model. Table 5.2 presents the fracture energies for fibre and matrix failure mode.

5.3 Quasi-static compression modelling of contoured core sandwich structure

In this section, the FE modelling procedures for the contoured-core sandwich structures based on CFRP and GFRP materials are presented. The numerical results will be verified using experimental data at the end of this section.

5.3.1 Selection of the part and element

The response of the contoured-core sandwich structures under compression loading was modelled using the shell element with reduced integration. The S4R shell element is defined by four nodal points. This S4R shell element is a general purpose element, and can be used in thin or thick shells.

Two circular upper and lower platens were defined as discrete rigid bodies and the core model was assembled in between the platens. The modelling technique adopted for composite in Abaqus was based on composite layup for conventional shell elements. It was measured that the thickness of each individual layer is 0.10 mm for GFRP and 0.25mm for CFRP.

5.3.2 Loading and boundary conditions

The axial crushing process was simulated by moving the top platen downwards in the y-direction, with the bottom plate being held stationary. This displacement boundary condition was assigned to the reference point, placed at the centre of the upper platen. The reference point was used to record the displacement and reaction load was recorded from the interaction between the platen and panel. The top and bottom edges

of the composite core were allowed to deform freely in all directions. Figure 5.1 shows the one of the cores with 3x3 unit cells between the upper and lower platens. A similar method was also adopted to model the flat-roof contoured structure. Details of the model dimensions and meshes for both types of contoured core structures are presented in Figure 5.2.

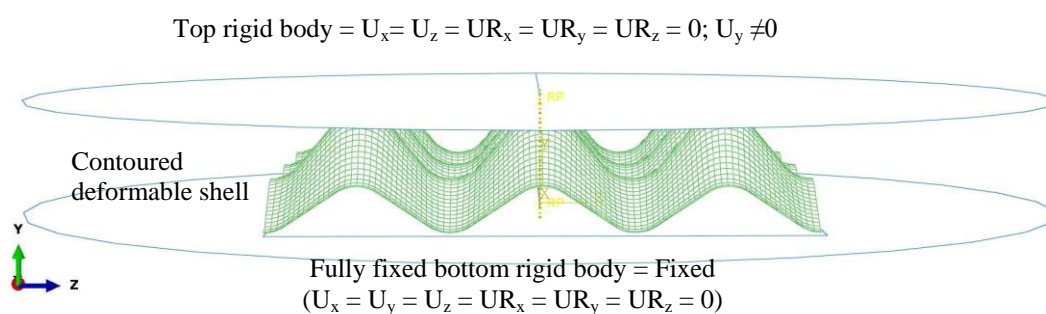


Figure 5.1 Loading direction, boundary conditions and assembly of the contoured core model between two platens.

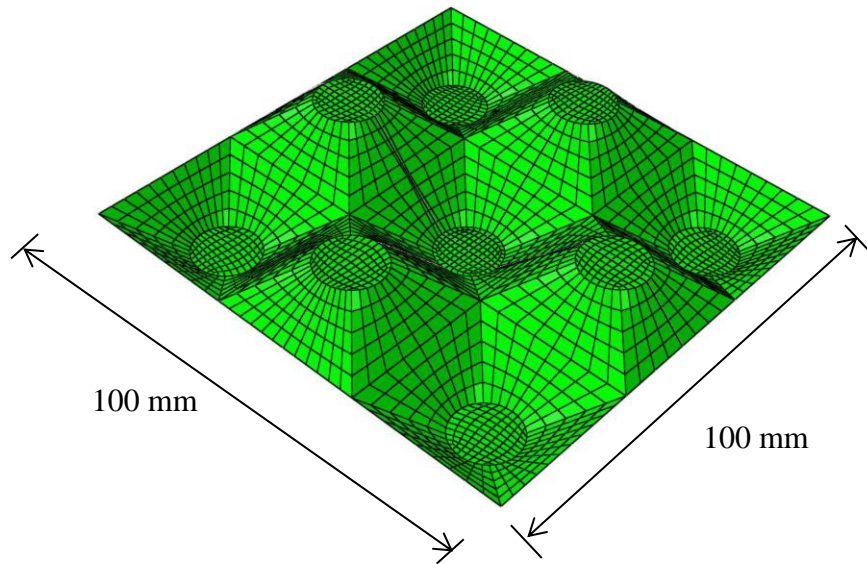
5.3.3 Interaction properties

The panel and the platen were connected using surface to surface contact. A coefficient of friction of 0.1 [128] was used between the panel and the rigid platens to mimic low friction between the smooth platen and the panel. A self-contact constraint was also added to the model in order to prevent the cell wall from penetrating into itself [129].

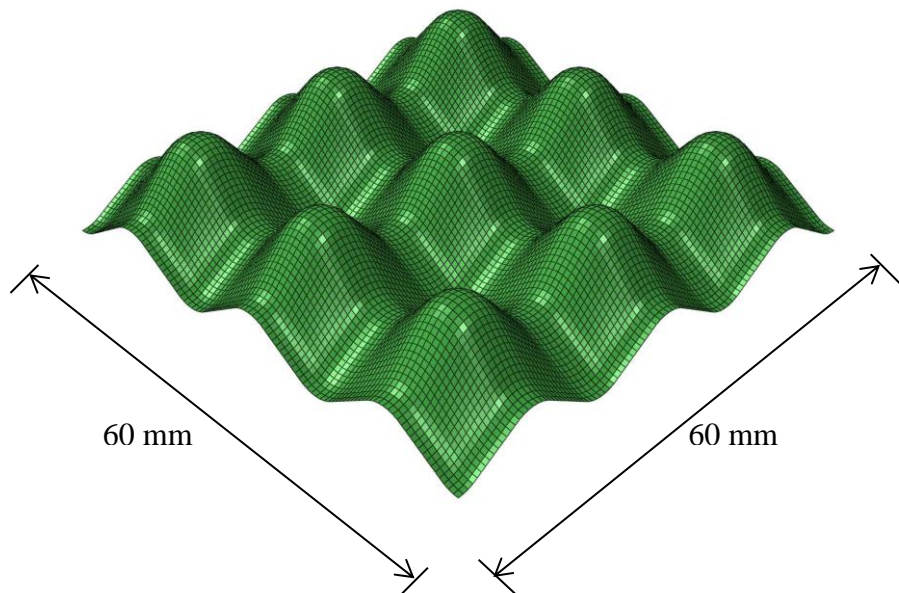
5.3.4 Mesh generation and control

GFRP and CFRP composite panels were modelled by a single layer of 4-noded, reduced integration shell elements (S4R) consisting of one element through the core thickness. Figures 5.2 (a) and (b) show the flat-roof and spherical-roof core models used in the simulation study. The core dimension of the flat-roof contour is (100mm

x100mm), whereas, it is (60mm x 60mm) for spherical-roof contour-core, as shown in Figures 5.2(a) and (b), respectively.



(a) Flat-roof



(b) Spherical-roof

Figure 5.2 Typical meshes used in numerical contoured core modelling.

5.3.5 Model convergence

The results of the model can be closely matched with experimental results by mesh refinement and by introducing the manufacturing defects for uneven cell wall thickness.

5.3.5.1 Model with imperfection

Most manufacturing routes result in some form of ‘small defect’ or imperfection in the finished structure. In fabricating a contoured-core, such flaws may be associated with geometrical imperfections resulting from spring-back following moulding, local variations in the fibre volume fraction as well as voids introduced during the moulding process. FE models that do not account for structural imperfections are likely to overestimate both the peak load and the stiffness of the whole structure. For example, Côté et al.[130] and Kazemahvazi and Zenkert [4] introduced imperfections in their numerical models to accurately predict the load displacement trace of contoured-core structures.

In this study, due to the imperfection in the contoured samples of the core cells, the composite exhibits an initial buckling before the core finally collapses. Therefore, the geometrical imperfection pattern was included in the model to predict the collapse behaviour of the flat-roof and spherical-roof contoured core structures. Here, the predicted buckling modes were applied to the numerical model by introducing a geometrical imperfection through the cell wall, which is given by:

$$\Delta x_i = \sum_{i=1}^M \omega_i \phi_i \quad (5.7)$$

where ϕ_i represents the i th mode shape and ω_i is the related scale factor. Variations in the thicknesses of the cell wall (from measurements) were used to perturb the mesh and the scale factor, which reflects the imperfection, being set to 5% of the core cell wall thickness. The appropriate time step in this explicit analysis was set to 0.1 seconds, which was ascertained through a series of numerical studies conducted with different durations, until dynamic effects were insignificant [4].

Figure 5.3 shows the results of four sensitivity simulations on the GFRP contoured core specimen. It is clear that a perfect model will overestimate the peak stress. In contrast, with increasing imperfection factor the peak stress gradually reduces.

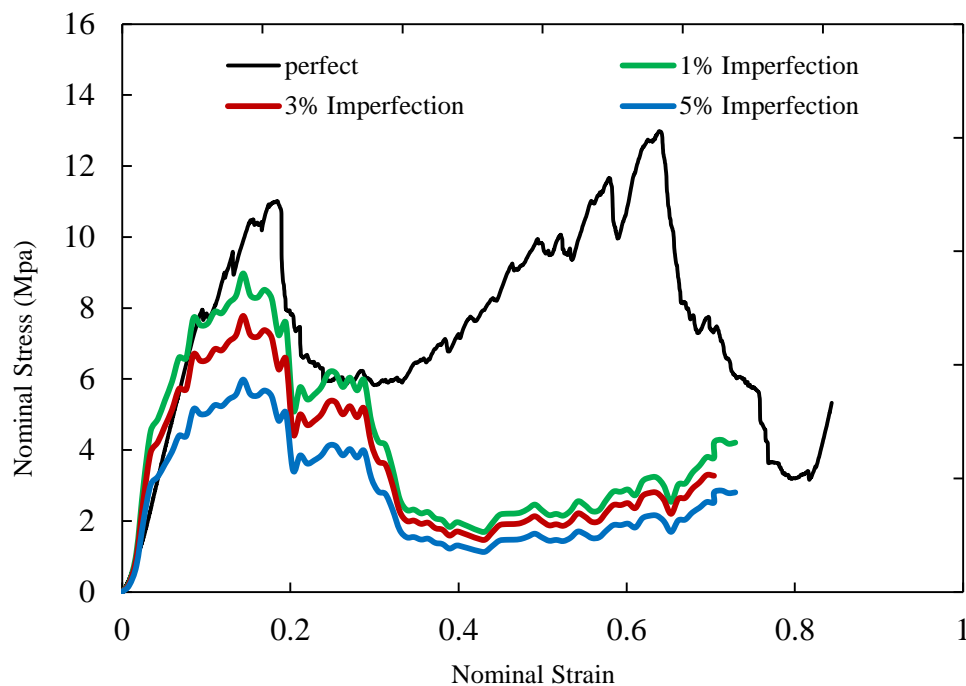


Figure 5.3 An imperfection sensitivity analysis study for the GFRP contoured core.

5.3.5.2 Mesh convergence analysis

A mesh sensitivity analysis was performed using a model of GFRP contoured-core specimen with the cell wall thickness of 1.5 mm. The finite element model was meshed using four different mesh sizes, these being 2 mm (coarse), 1.0 mm (medium), 0.8 mm (fine) and 0.5 mm (very fine).

Figure 5.4 shows the variation of the prediction to test data and CPU time with element size. The accuracy of the model can be improved with the increase of mesh density. However the computation time is also increased. Therefore, it is recommended to identify a balance between element size and the CPU consumption. Table 5.3 also summarises the findings of the mesh convergence analysis, which comprises the relationships between the predicted compressive strength and element size. As anticipated, the CPU time increases as the density of elements is increased. Similarly, the predicted compressive strength reaches close to the experimental values as the size of elements decreases.

Table 5.3 Details of mesh sensitivity analysis.

convergence condition	Mesh size [mm]	Compressive Strength [MPa]	FE/exp difference [%]
Experiment	-	5.6	-
FE	2.0	7.6	+35
FE	1.0	5.9	+5.35
FE	0.8	5.9	+5.35
FE	0.5	5.8	+3.57

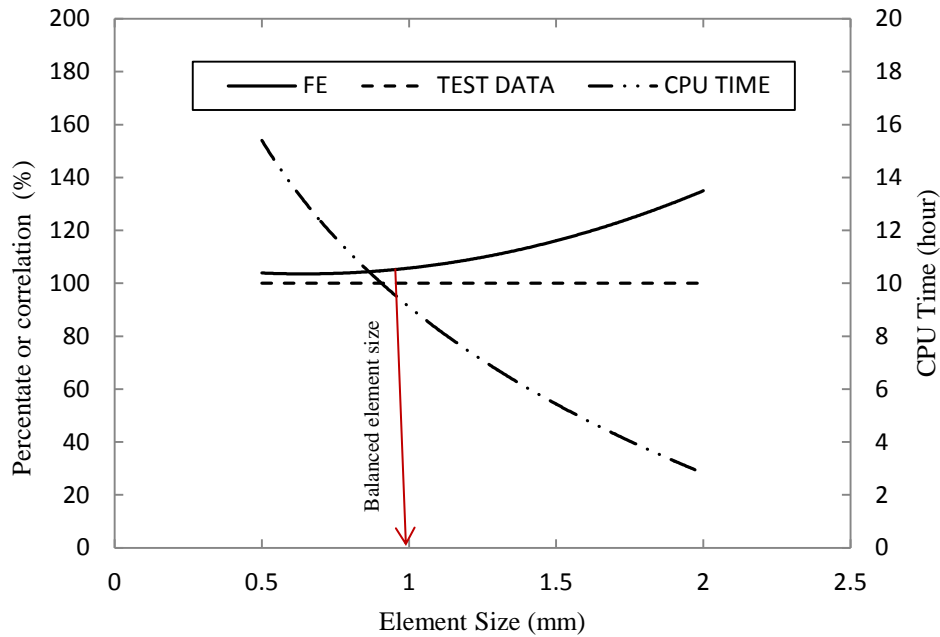


Figure 5.4 Variation of the prediction to test data and CPU time with element size.

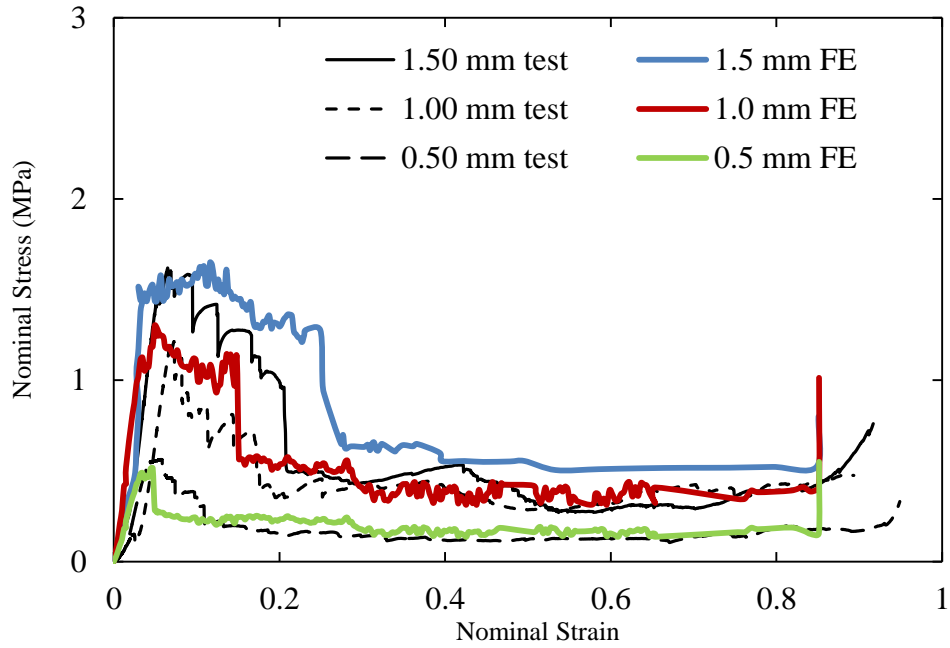
5.3.6 Modelling data output

The data output from the numerical models was specified by creating output requests. The Abaqus solver calculates the values of many variables at every increment. The user may control and manage the data output so that only data required to interpret the results of the analysis is produced. An output request defines which variables are selected and outputted during the simulation step, from which region or integration points of the model and the rate at which the variable are written to the output database.

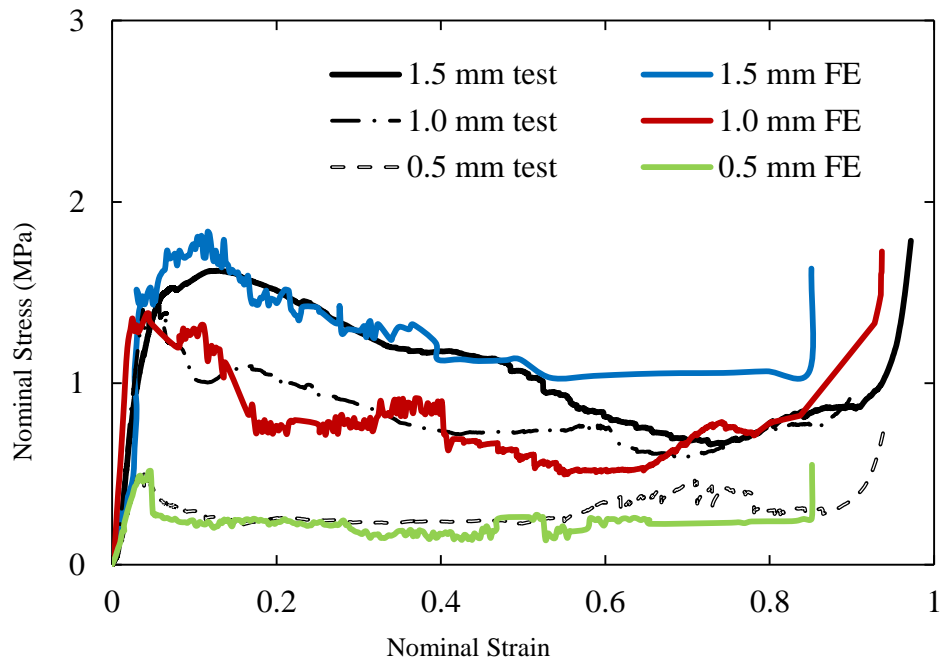
History outputs are generated either from the whole model or specific points in the model. The frequency of data output depends on the user's interest, and can be very high if necessary. When creating a history output request, the individual components of variables can be specified. In this study, the displacement and reaction forces for the relevant direction of the platen were requested in a history output.

5.3.7 Quasi-static compression results from the two dimensional finite element simulations

The FE models were validated against the experimental data relating to the flat-roof and spherical-roof contoured panels, made from GFRP and CFRP materials. Figures 5.4(a) and (b) compare the predicted quasi-static and experimentally obtained stress-strain curves of GFRP and CFRP flat-roof contoured panels with cell wall thicknesses of 0.5, 1.0 and 1.5 mm (imperfection variation of 5% was given to all three cell wall thicknesses of FE models) respectively. It is clear that the FE predictions are in a good agreement with the experimental results for the CFRP and GFRP flat-roof contoured core panels. From the figure, it is evident that the stress-strain curves for the GFRP flat-roof contoured core show a steady increase in stress until they reach the peak value. After the initial peak stress, continuous loading caused the reduction in structural stiffness, results gradual drops in stress between the strains of 0.03 and 0.2, which is followed by a sudden drop in stress level and into a plateau stage in a strain range of 0.2 to 0.7. It should be noted that since a perfect contact between the core and the skin was assumed, the FE predictions slightly over-estimate the measured stiffness. Similar to the GFRP, CFRP flat-roof contoured core shows a steady increase in stress until the peak values for all the three thicknesses. These peak values are almost similar to the peak values of GFRP samples. However, after the peak value, stress dropped much more gradually towards the plateau region, Figure 5.5(b). This plateau lies between the strains of 0.1 to 0.7, before the final densification.



(a) GFRP

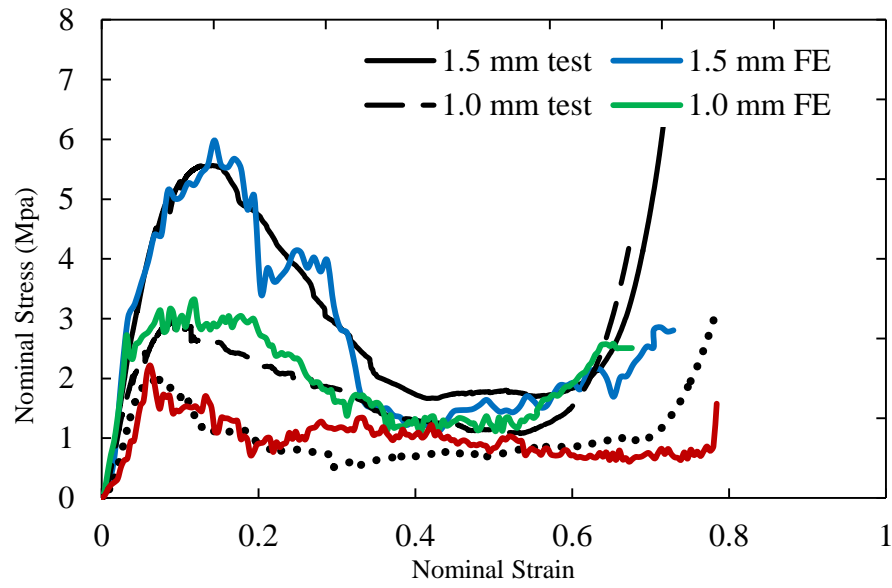


(b) CFRP

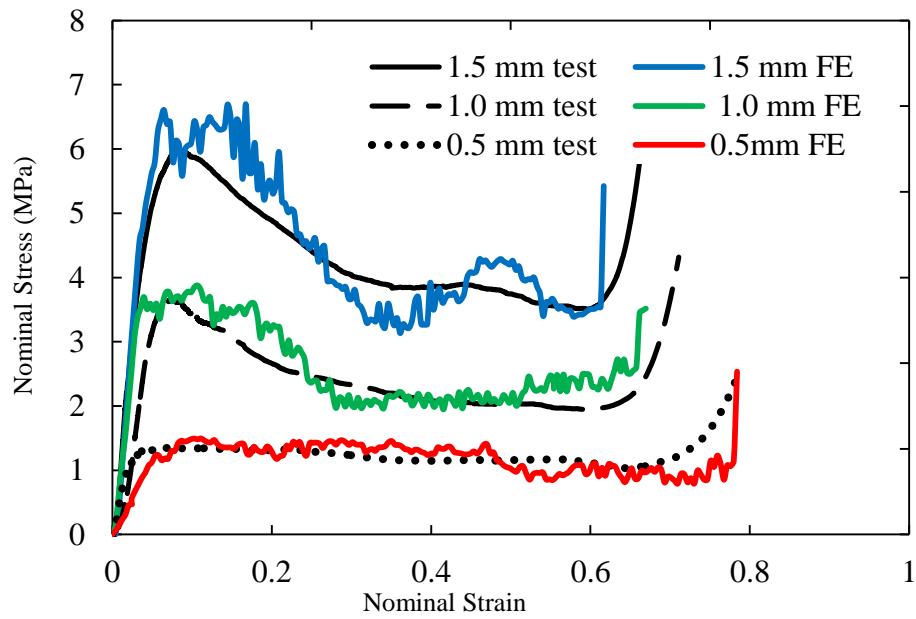
Figure 5.5 Stress-strain traces for the flat-roof contoured core panels, with the predictions from the 2-D imperfection finite element model.

Figure 5.6 compares the measured and simulated compression stress-strain traces for the spherical-roof contoured core based on 3x3 unit cells, with cell wall thicknesses of 0.5, 1.0 and 1.5 mm (imperfection variation of 5% was given to all three cell wall thicknesses of FE models). Generally, correlation between the experimental results and the FE data is good, with all of the main features being captured by the model, including similar values of initial stiffness, peak stress, plateau stress and densification thresholds. In both the experimental and FE models, GFRP and CFRP panels respond in a roughly linear manner up to the peak stress, as shown in Figures 5.5(a) and (b). It is clear from the stress-strain plot of the GFRP contoured core that the stress values for experiment and FE are dropped gradually by 60% at the strain of 0.3 for the thickest core cell wall sample. However, the plateau region is more or less between the strains of 0.3 and 0.8 for all core cell wall thicknesses except for the thickest core. The sever drop of the stress towards the plateau region is associated with the brittle failure of the GFRP, which reflects the failure mode of GFRP as shown in different failure modes in Figure 5.7.

Figure 5.6(b) depicts the stress-strain plots of CFRP spherical-roof contoured core panel. The core with the cell wall thickness of 0.5mm possess the maximum stress of 1.42 MPa, whereas two other thicknesses have reached the maximum stress of 3.76 MPa and 6.46 MPa, respectively. An increase of plateau stresses have been observed in CFRP compared to its GFRP counterparts due to the higher strength of the former. These plateau stresses are continued until densification thresholds for CFRP spherical-roof contoured models.



(a) GFRP



(b) CFRP

Figure 5.6 Stress-strain traces for the spherical-roof contoured core panels, with the predictions from the 2-D imperfection finite element mode.

All Stress-strain curves in Figures 5.5 and 5.6 shows that the model traces exhibit some oscillations as compared to the experimental traces. These oscillations are likely caused by the brittle failure of plies in the composite layup models.

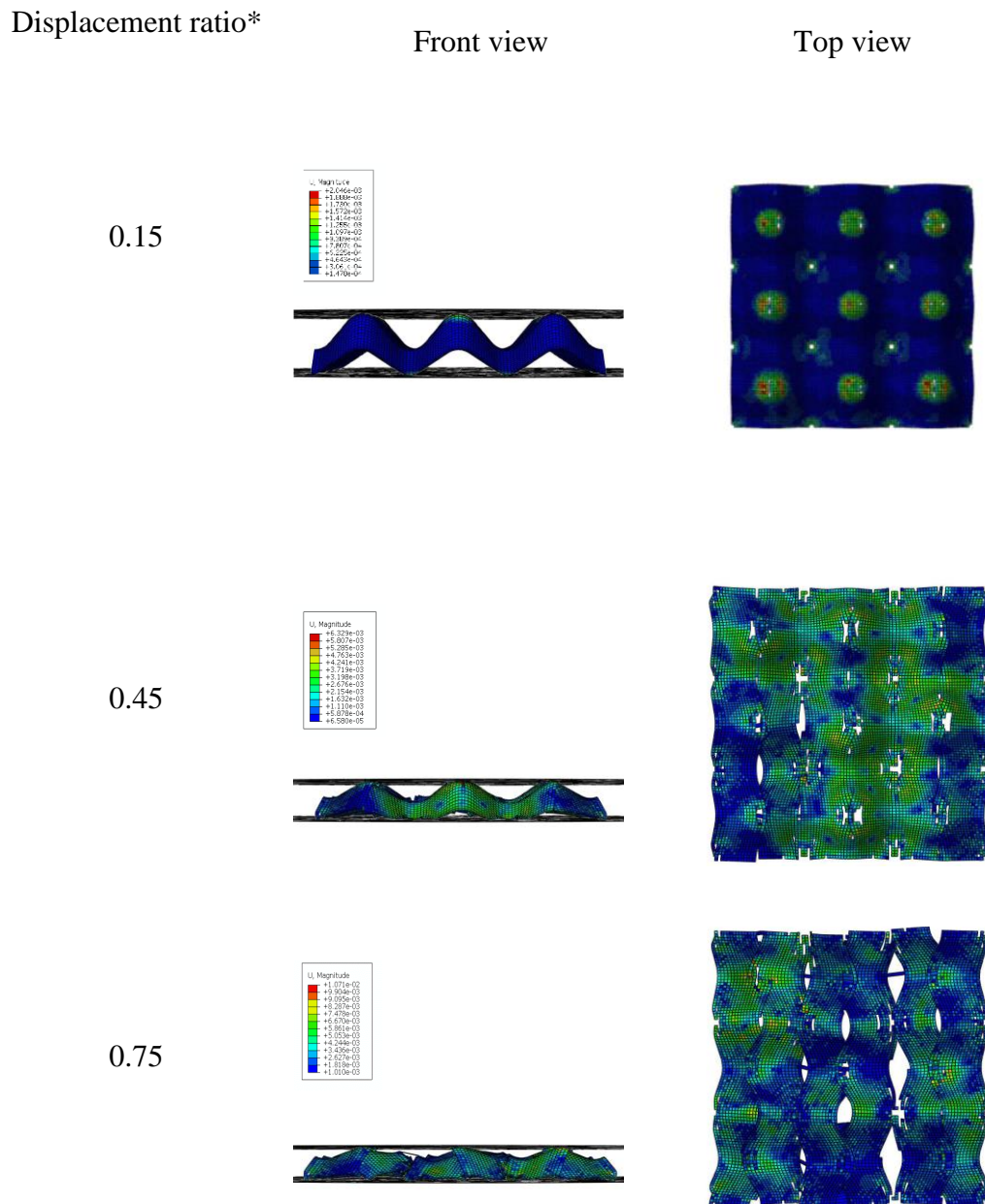


Figure 5.7 Progressive failure of GFRP spherical-roof panels (*displacement ratio=displacement/the original height of the core).

Figure 5.7 shows the progressive damage of a GFRP contoured core. Initial displacement ratio (0.15) indicates chink and flattened domes. Further displacement

shows small cracks as it would appear to be the early stage of failure mode. It is visible from the front view that the cores are flattened along with cracks on its surface. Whereas, the top views visualize the cracks which split the surface at the displacement ratio of 0.75. From these failure modes, it is clear that fracture and cracks dominated the collapse behaviour of the GFRP structures.

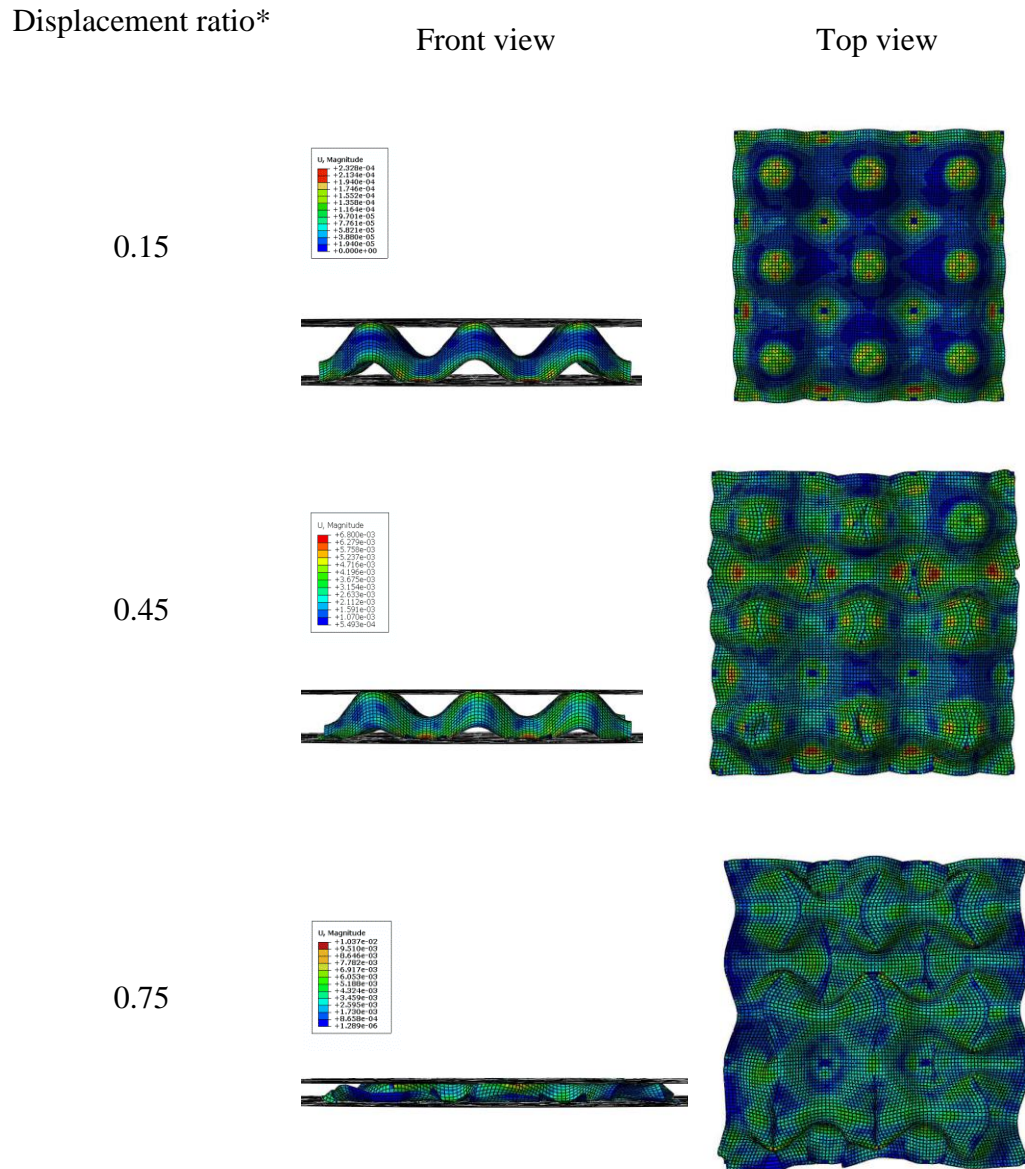


Figure 5.8 Progressive failure of CFRP spherical-roof panels (*displacement ratio=displacement/the original height of the core)..

Figure 5.8 shows the deformation of a CFRP contoured core at different displacement ratios. Initial displacement ratio (0.15) shows flattened domes without any cracks or buckling. Further, dimpling occurs on domes at the displacement ratio of 0.45. Finally, the contoured core is flattened with huge deformation in the structure. It is clear that buckling and hinges dominate the collapse behaviour of the structures, which lead relatively ductile failure modes.

5.4 Dynamic finite element modelling

This section presents details of the numerical modelling procedures for the GFRP and CFRP contoured-core structures under dynamic compression loading. The response of the contoured-core sandwich structures under dynamic loading was modelled using the shell element, same as in the quasi-static modelling in Section 5.2 and 5.3. The impactor was modelled as a flat plate using a discrete rigid surface. A point mass, equal to the mass of the experimental impactor, was assigned to a reference point located at the centre of the flat plate. The reference point was also used to record the displacement from this model. An initial velocity was prescribed to the rigid plate, which is equal to the impact velocity engaged in the experiments. An initial imperfection was also introduced in the sandwich structure modelling in order to accurately predict the deformation behaviour, as mentioned in Section 5.3.5. A surface-to-surface contact was used to define contact between the impactor and the core model. Self-contact within the contoured-core was also specified.

5.4.1 Input data

The input data for the elastic property and progressive damage development in this model were used as described in Sections 5.2. Numbers of studies have shown that the increased strain rates generally lead to increased mechanical properties, such as

strength and modulus of carbon/epoxy and glass/epoxy composites [131-134]. Mechanical properties of these composites are increased ranging from 8% to 43% [131-138]. This implies that the sensitivity of mechanical properties at high strain rate is dependent on composite type and polymer matrix. Therefore, in the current study of dynamic model, the mechanical properties have been increased by 10% for CFRP and 16% for GFRP to consider the strain rate effect.

5.4.2 Output data

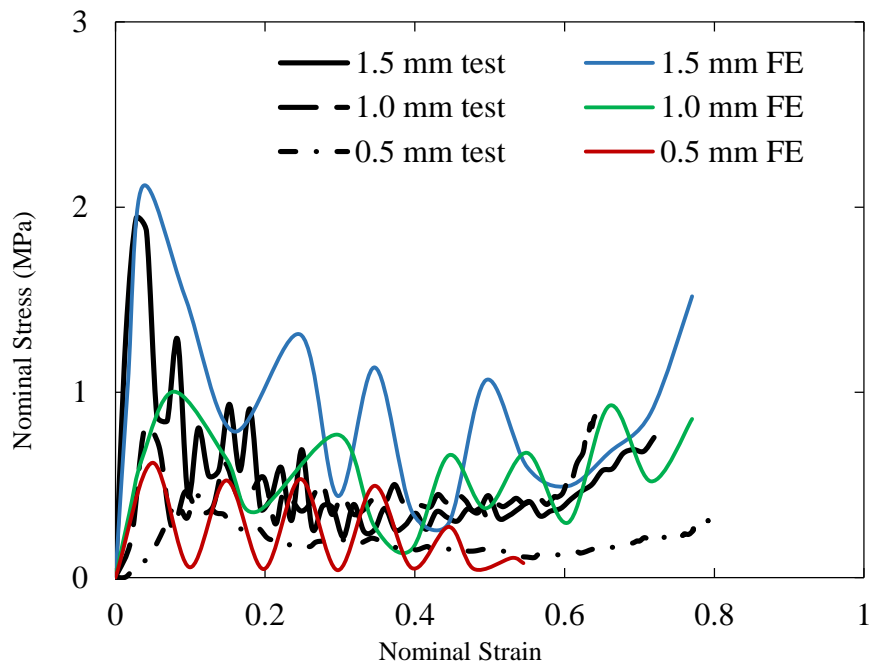
In this analysis, the stress, strain, contact force and displacement output were requested for the whole sandwich structure model. In the history output, the displacement data in the y -direction were obtained at the rigid platen reference point, while the contact force data were measured from the interaction between the impactor and contoured-core panel.

5.4.3 Results from the numerical analysis

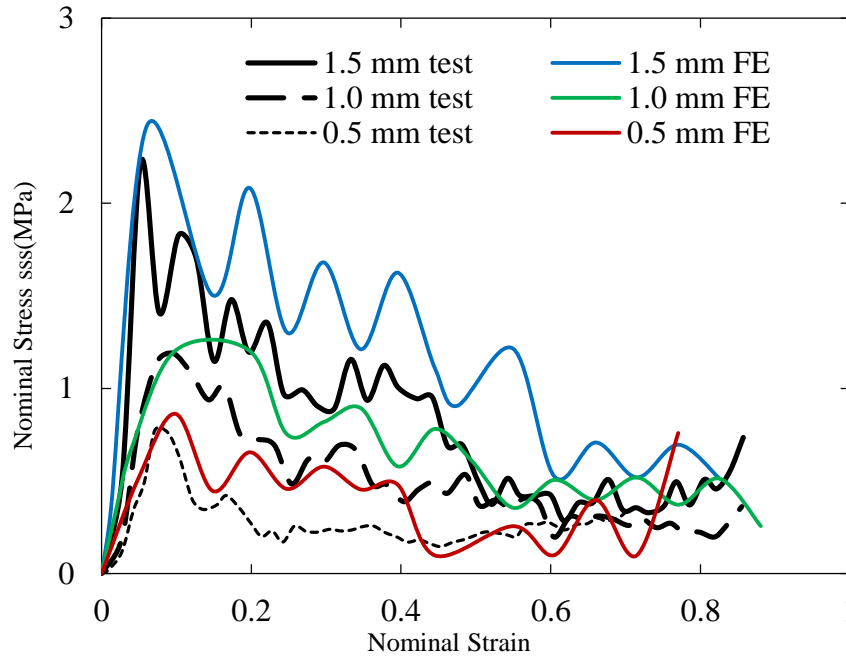
Figures 5.8(a) and (b) shows the stress-strain traces from the experimental and FE results, for flat-roof composite contoured-core structures. The stress-strain curves in Figure 5.8(a) show that the models exhibit a fluctuated trend similar to the experimental data. It should be noted that since perfect contact between the core and the skin was assumed in all cases, the FE predictions were slightly over-estimated.

Figure 5.8(b) compares the experimental stress-strain traces of CFRP contoured panels with the cell wall thicknesses of 0.5, 1.0 and 1.5 mm with the predictions offered by the FE models. It is evident that all traces exhibit similar characteristics, with stress rising to a maximum before the gradual dropping. For example, the core with 1.5 mm cell wall thickness, initially displays a linear response up to the first peak of approximately 2.4 MPa. This is followed by a substantial drop to approximately

1.5MPa before reaching the second peak of 2 MPa. This trend of oscillation continuous until the final densification stage. Again, as perfect contact between the core and the skin was assumed in all cases, the FE predictions were over-estimated in comparison to the measured peaks.



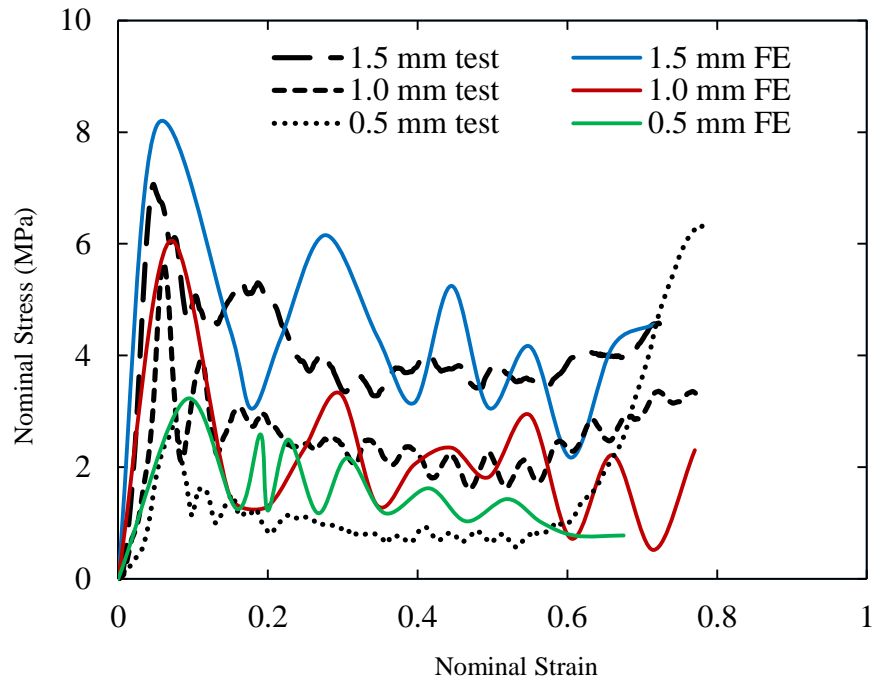
(a) GFRP flat-roof



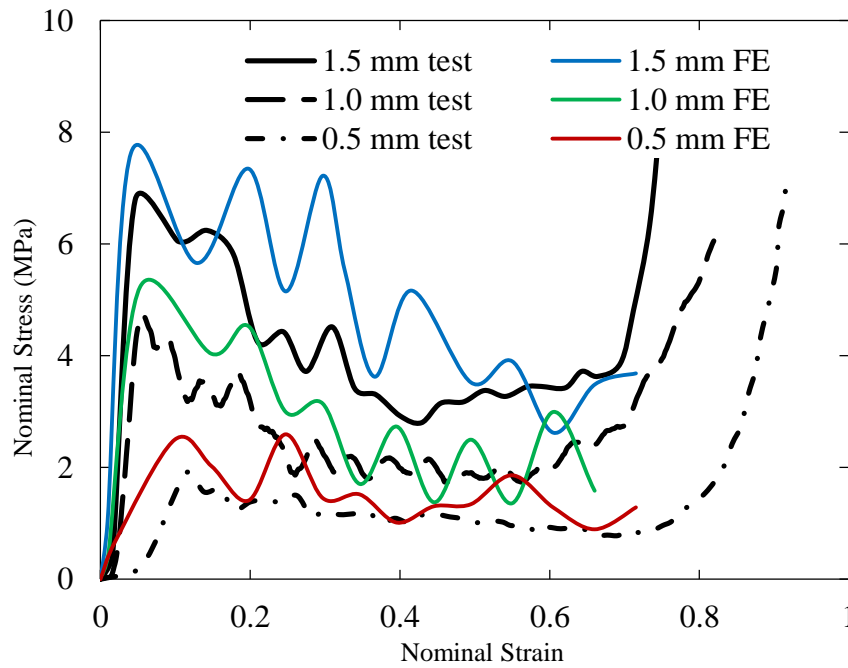
(b) CFRP flat-roof

Figure 5.9 Low-velocity stress-strain traces following compression tests on the contoured panels.

Figure 5.10 (a) and (b) also shows that the FE model is able to exhibit a similar general trend as the experimental results for spherical-roof contoured panels, despite the severe oscillation in the stress strain curve. Here, all of the main features including initial stiffness, peak stress and plateau stress are captured. However, the stabilised crushing stress in the FE model was overestimated by 10 to 20%, due to the perfect contact model. It has been noticed from Figures 5.9(a) and (b), that thin cell wall (i.e. 0.5 and 1.0 mm), have shown much closer correlation with the tests as compared to 1.5 mm cell wall core panel. This may be associated with the low probability of flaws in the core samples with thin cell walls (i.e. 0.5 and 1.0 mm) as compared to the thicker one.



(a) GFRP



(b) CFRP

Figure 5.10 Low-velocity stress-strain traces following compression tests on the spherical-roof contoured panels.

The failure mode of FGRP contoured panel in the dynamic FE model was observed as similar to the quasi-static model (Figure 5.7), where buckling followed by fibre fracture and the flattening of the panels were the typical damage mechanisms of the structure, as shown in Figure 5.11.

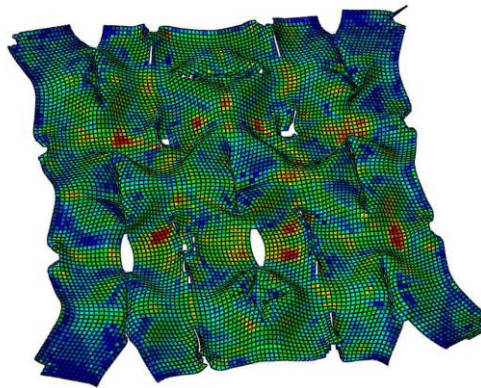


Figure 5.11 Deformation of spherical-roof GFRP contoured under low-velocity impact loading.

5.5 3D finite element modelling

Three dimensional finite element models were developed to simulate the crushing behaviour of these contoured sandwich panels to investigate the influence of the deformation through the thickness on the structural response. The numerical simulations were also compared with the experimental results.

5.5.1 Mesh generation, boundary and loading conditions

Figure 5.12 shows the finite element mesh of the contoured core based sandwich panels. Here, the contoured cores were meshed using six-noded triangular solid elements, while the composite skins using eight-noded brick elements. The loading platens above and below the panel were meshed using discrete rigid elements. The model has a number of interfaces that need to be considered. These include those between the contoured core and platens, those between the face sheet and platen, as

well as those between the composite contoured core and the face sheet. The platens are allowed to contact the contoured core in case the skin is damaged. Material properties of GFRP and CFRP composite cores are presented in Table 5.4.

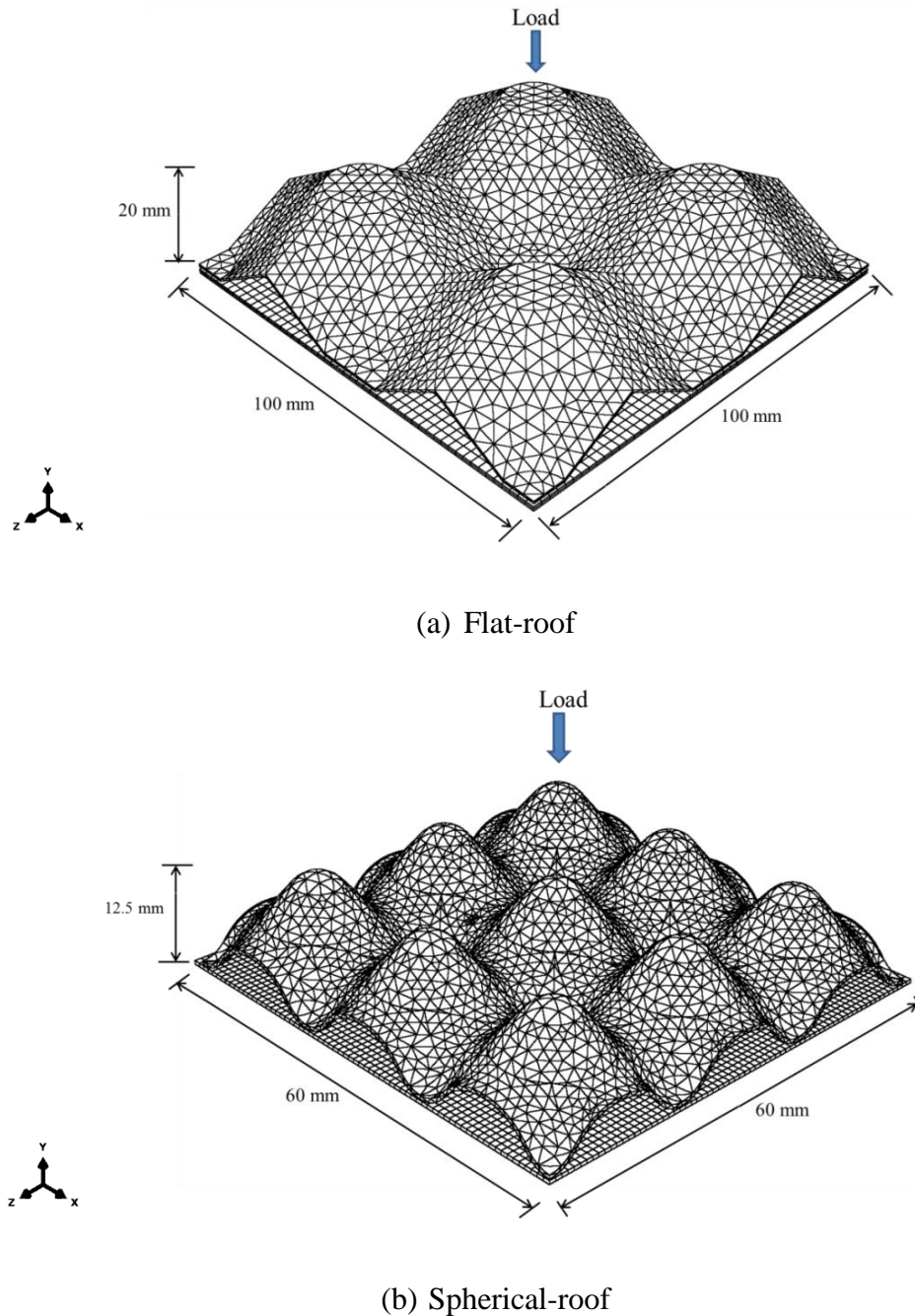


Figure 5.12 The geometry, mesh, boundary and loading conditions of contoured core based sandwich panels (the top skin and loading platen are removed).

Table 5.4 Properties of the woven fabric glass-fibre reinforced plastic, (GFRP) and the woven fabric carbon-fibre reinforced plastic, (CFRP) [7, 122, 123].

Symbol	GFRP	CFRP	Property
E_1 [GPa]	23	48	Young's modulus in longitudinal direction
E_2 [GPa]	23	48	Young's modulus in transverse direction
E_3 [GPa]	5	1	Young's modulus in thickness direction
ν_{12}	0.15	0.1	Poisson's ratio in 1-2 plane
ν_{13}	0.15	0.1	Poisson's ratio in 1-3 plane
ν_{23}	0.27	0.28	Poisson's ratio in 2-3 plane
G_{12} [GPa]	5	9	Shear modulus in 1-2 plane
G_{13} [GPa]	5	9	Shear modulus in 1-3 plane
G_{23} [GPa]	3.5	3.7	Shear modulus in 2-3 plane
X_{1t} [MPa]	320	550	Longitudinal tensile strength
X_{1c} [MPa]	260	150	Longitudinal compression strength
X_{2t} [MPa]	320	550	Transverse tensile strength
X_{2c} [MPa]	260	150	Transverse compressive strength
S_{12} [MPa]	100	120	Shear strength in 1-2 plane
S_{13} [MPa]	100	120	Shear strength in 1-3 plane
S_{23} [MPa]	100	120	Shear strength in 2-3 plane

5.5.2 Modified 3D Hashin's failure criteria

Failure criteria for fibre reinforced composites are available in ABAQUS. However, they can only be applied for 2D cases, i.e. using shell or continuum shell elements. Therefore, in order to develop failure criteria suitable for simulating the composite failure through its thickness, the modified Hashin's 3D failure criteria [139] are employed. The failure criteria, with the related constitutive model, are then implemented into ABAQUS/Explicit using a user-defined subroutine [140]. The modified 3D failure criteria [139, 140] may be used to simulate overall response of contoured-core sandwich in a coordinate system (1,2,3). The failure functions can be expressed as follows:

Fibre tension: ($\sigma_{11} > 0$)

$$\text{If, } \left(\frac{\sigma_{11}}{X_{1t}} \right)^2 + \left(\frac{\sigma_{12}}{S_{12}} \right)^2 + \left(\frac{\sigma_{13}}{S_{13}} \right)^2 = 1, \text{ then } d_{ft} = 1 \quad (5.8)$$

Fibre compression: ($\sigma_{11} < 0$)

$$\text{If, } \frac{|\sigma_{11}|}{X_{1c}} = 1, \text{ then } d_{fc} = 1 \quad (5.9)$$

Matrix tension: ($\sigma_{22} + \sigma_{33} > 0$)

$$\text{If, } \frac{(\sigma_{22} + \sigma_{33})^2}{X_{2t}^2} + \frac{\sigma_{23}^2 - \sigma_{22}\sigma_{33}}{S_{23}^2} + \frac{\sigma_{12}^2 + \sigma_{13}^2}{S_{12}^2} = 1, \text{ then } d_{mt} = 1 \quad (5.10)$$

Matrix compression: ($\sigma_{22} + \sigma_{33} < 0$):

$$\text{If, } \left[\left(\frac{X_{2c}}{2S_{23}} \right)^2 - 1 \right] \frac{(\sigma_{22} + \sigma_{33})}{X_{2c}} + \frac{(\sigma_{22} + \sigma_{33})^2}{4S_{23}^2} + \frac{\sigma_{23}^2 - \sigma_{22}\sigma_{33}}{S_{23}^2} + \frac{\sigma_{12}^2 + \sigma_{13}^2}{S_{12}^2} = 1, \text{ then } d_{mc} = 1 \quad (5.11)$$

where X_{1t} , X_{1c} , X_{2t} , X_{2c} , S_{12} , S_{13} and S_{23} are the various strength components [141] and d_{ft} , d_{fc} , d_{mt} and d_{mc} are the damage variables associated with the four failure modes. The response of the material after damage initiation (which describes the degradation of the material stiffness once the initiation criterion is satisfied) is defined by the following equation:

$$\sigma = C(d) \cdot \varepsilon \quad (5.12)$$

$$\begin{bmatrix} \sigma_{11} \\ \sigma_{22} \\ \sigma_{33} \\ \sigma_{12} \\ \sigma_{23} \\ \sigma_{13} \end{bmatrix} = \begin{bmatrix} C_{11} & C_{12} & C_{13} & & & \\ C_{12} & C_{22} & C_{23} & & & \\ C_{13} & C_{23} & C_{33} & & & \\ & & & C_{44} & & \\ & & & & C_{55} & \\ & & & & & C_{66} \end{bmatrix} \begin{bmatrix} \varepsilon_{11} \\ \varepsilon_{22} \\ \varepsilon_{33} \\ \varepsilon_{12} \\ \varepsilon_{23} \\ \varepsilon_{13} \end{bmatrix} \quad (5.13)$$

where the non-zero terms of the above C_{ij} (6 x 6) symmetric damage degradation matrix can be written as:

$$\begin{aligned} C_{11} &= (1-d_f)E_1(1-v_{23}v_{32})\Gamma \\ C_{22} &= (1-d_f)(1-d_m)E_2(1-v_{13}v_{31})\Gamma \\ C_{33} &= (1-d_f)(1-d_m)E_3(1-v_{12}v_{21})\Gamma \\ C_{12} &= (1-d_f)(1-d_m)E_1(v_{21}-v_{31}v_{23})\Gamma \\ C_{23} &= (1-d_f)(1-d_m)E_2(v_{32}-v_{12}v_{31})\Gamma \\ C_{31} &= (1-d_f)(1-d_m)E_1(v_{31}-v_{21}v_{32})\Gamma \\ C_{44} &= (1-d_f)(1-s_{mt}d_{mt})E_1(1-s_{mc}d_{mc})G_{12} \\ C_{55} &= (1-d_f)(1-s_{mt}d_{mt})E_1(1-s_{mc}d_{mc})G_{23} \\ C_{66} &= (1-d_f)(1-s_{mt}d_{mt})E_1(1-s_{mc}d_{mc})G_{13} \end{aligned} \quad (5.14)$$

where E_1 , E_2 and E_3 are the Young's modulus in the 1, 2 and 3 directions respectively, G_{ij} is the shear modulus in the i - j plane and ν_{ij} ($i, j = 1, 2, 3$) is the Poisson's ratio for transverse strain in the j direction. The terms s_{mt} and s_{mc} are introduced to control the reduction in shear stiffness resulting from tensile and compressive failure in the matrix respectively. The following values for these parameters are given in Abaqus: $s_{mt} = 0.9$ and $s_{mc} = 0.5$ [142].

$$\begin{aligned} d_f &= 1 - (1 - d_{ft})(1 - d_{fc}) \\ d_m &= 1 - (1 - d_{mt})(1 - d_{mc}) \\ \Gamma &= 1 / (1 - \nu_{12}\nu_{21} - \nu_{23}\nu_{32} - \nu_{13}\nu_{31} - 2\nu_{21}\nu_{32}\nu_{13}) \end{aligned} \quad (5.15)$$

The Young's moduli, shear moduli, Poisson's ratios and strengths of the composites are given in Table 5.4.

5.6 Implementation of the material model in ABAQUS/Explicit

The user-defined VUMAT subroutine was used to implement the material model and the aforementioned failure criteria in ABAQUS/Explicit. Here, during each computational iteration, this subroutine is called enabling ABAQUS/Explicit to obtain the necessary information regarding the state of the material and its mechanical response at each integration point within each element. The appropriate time step in this analysis was set to 0.1 seconds, which was ascertained through a series of numerical studies conducted with different durations, until dynamic effects were insignificant. Hashin's 3D failure criteria given in Equations (5.8) to (5.11) are introduced. The stresses are computed within the VUMAT subroutine using the given material stiffness coefficients. Once the failure criteria are satisfied to all integration points within an element, the failed element would be removed from the mesh. At this

point, the stress of the element contributes no resistance to the model stiffness in the subsequent deformation.

5.6.1 Cohesive elements and material properties

The resin layer at the interface between the skins and core was modelled using cohesive elements available in ABAQUS [142]. The elastic response was defined in terms of a traction-separation model by assuming an initially linear elastic behaviour, followed by initiation and evolution of damage. The elastic behaviour of the element is written in terms of elastic constitutive matrix. The diagonal terms in the elasticity matrix should be calculated using the true thickness of the cohesive layer (t_c) as follows:

$$\begin{aligned} K_{nn} &= \frac{E_n}{t_c} \\ K_{ss} &= \frac{E_s}{t_c} \\ K_{tt} &= \frac{E_t}{t_c} \end{aligned} \quad (5.16)$$

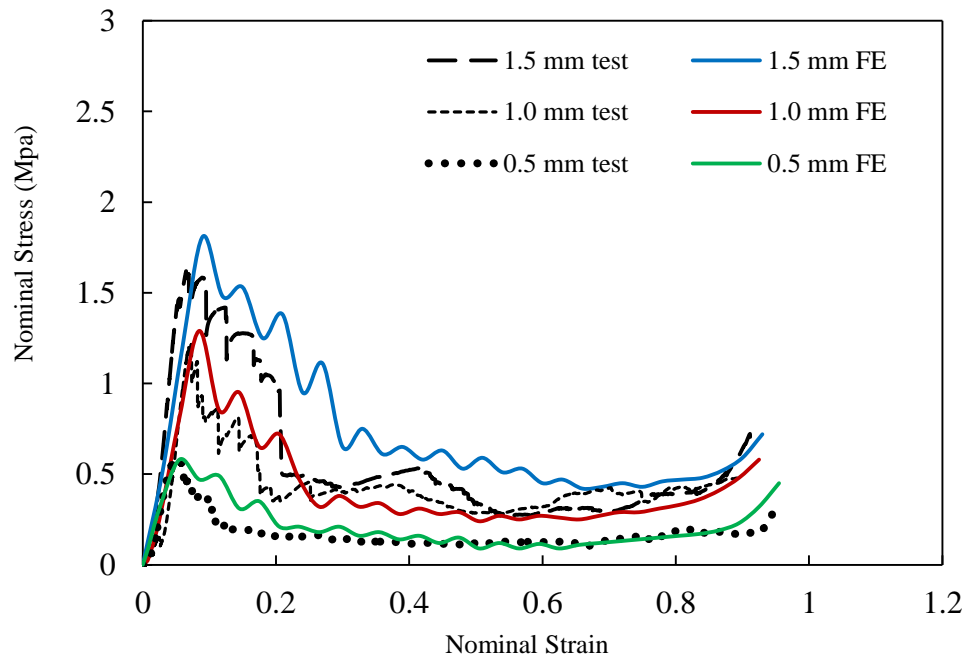
where E_n , E_s and E_t are stiffness along the normal and two tangential directions, respectively. The quadratic nominal stress and energy criterion were used to model damage initiation and damage evolution of the cohesive layer, respectively. Damage evolution was defined based on the energy conjunction with a linear softening law. The mechanical properties of the cohesive elements were obtained from [143].

5.7 3D Numerical modelling of the compression response of flat-roof and spherical-roof contoured cores

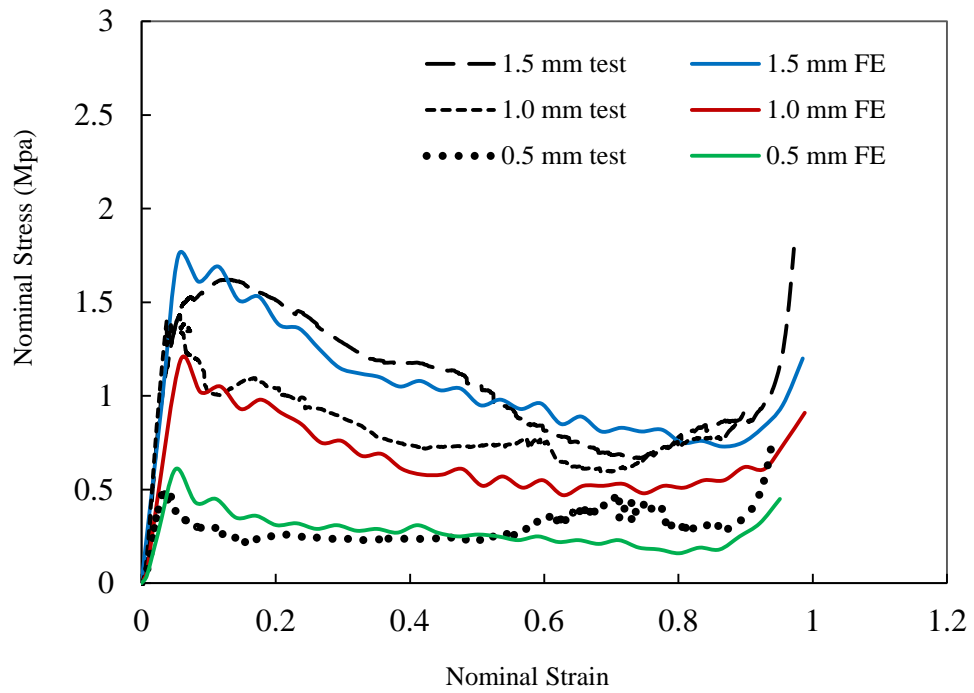
Figure 5.13 and Figure 5.15 show the predicted stress-strain traces for the flat-roof and spherical-roof contoured cores based on the GFRP and CFRP, together with the corresponding test results. In general, correlation between the experimental and numerical data is very good, with all of the main features being captured, including the initial stiffness, peak stress, initial failure, plateau and densification stages. The evidence in these figures suggests that energy absorption up to densification can be reasonably predicted using the 3D FE models. The traces predicted for all three cell wall thicknesses show a very good agreement in the subsequent plateau stages. The finite element models provide a slightly higher peak load for the thickest cell wall cores made from both the GFRP and the CFRP. This may be associated with a slight variation on the wall thickness of the sample, which is not considered in the modelling.

The progressive failure modes predicted by the finite element models were compared with those observed experimentally. Figures 5.13 and 5.15 compares the predicted deformation modes produced by the model with the specimens tested subjected to various levels of deformation. A completely crushed sample and model with the skins removed are also shown in Figures 5.16 (a) and (b). Clearly, the basic characteristics of the experimental failure modes are captured in the model, in which flattening of the flat-roof contoured core and their final collapse are evident. The progressive failure modes predicted in the spherical-roof core are shown in Figure 5.18. The skins were also removed to assist viewing the progressive deformations. Clearly, the GFRP samples exhibited a brittle failure, involving extensive crushing and matrix cracking

with fibre fracture. Again, the matrix cracking observed in the finally collapsed GFRP sample is reproduced by the finite element simulations, as shown in Figure 5.18(a). On the contrary, the CFRP panels were failed in a ductile manner with the core almost flattened due to matrix cracking, Figure 5.18(b).



(a) GFRP



(b) CFRP

Figure 5.13 Quasi-static stress-strain traces following compression tests on the flat-roof contoured panels.

Displacement

ratio

Test

Modelling

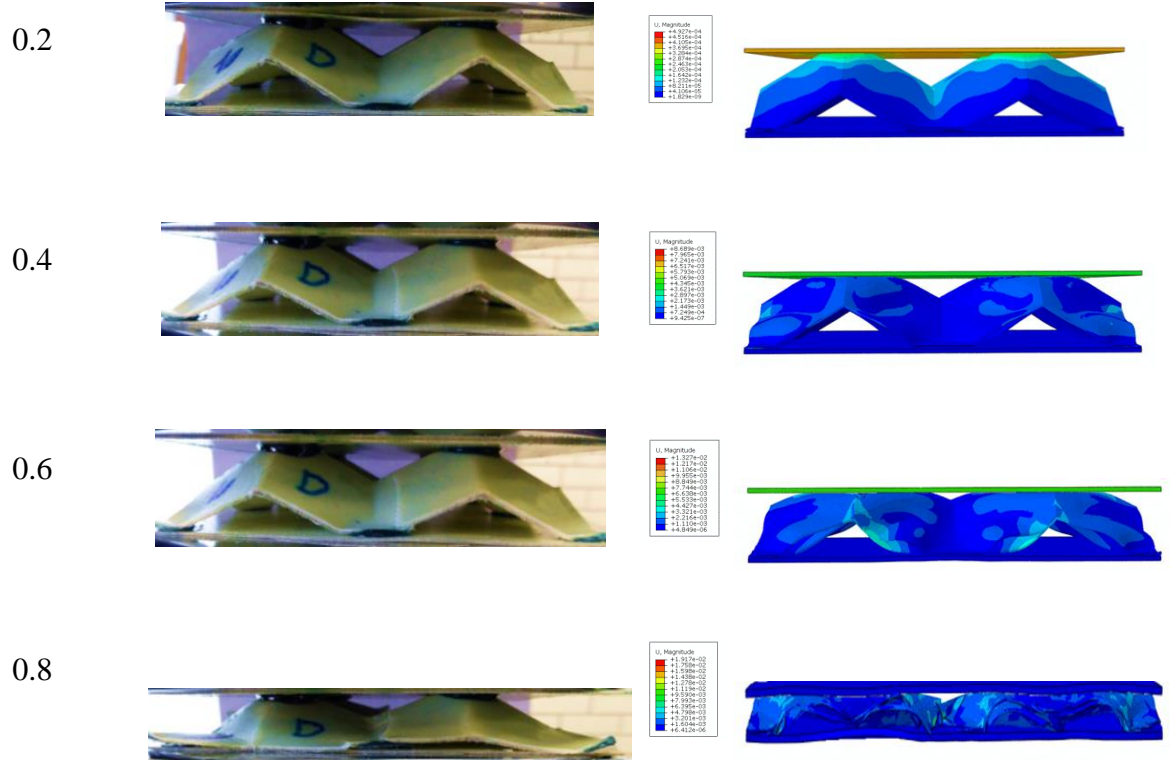
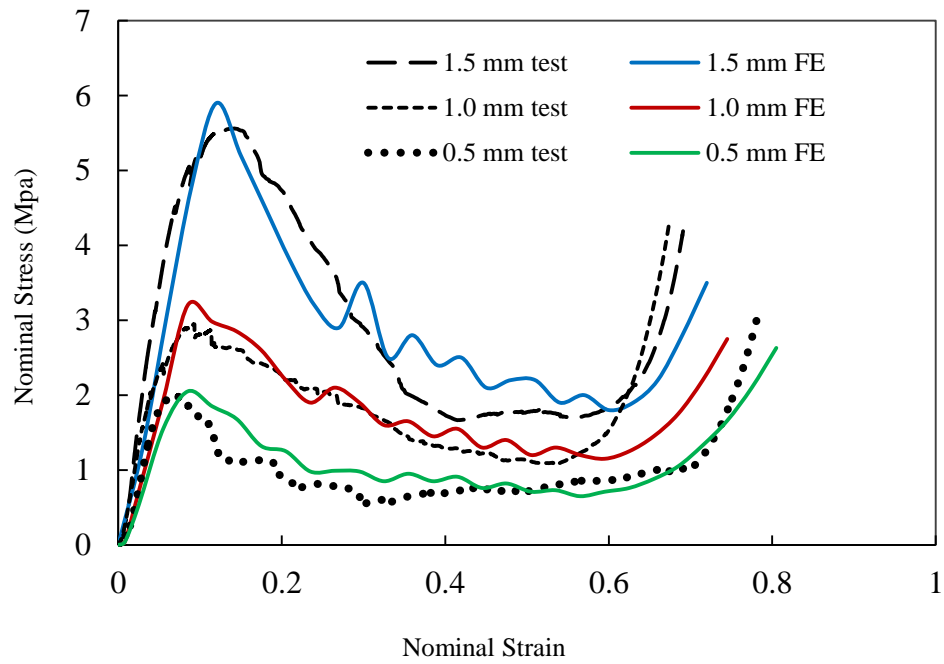
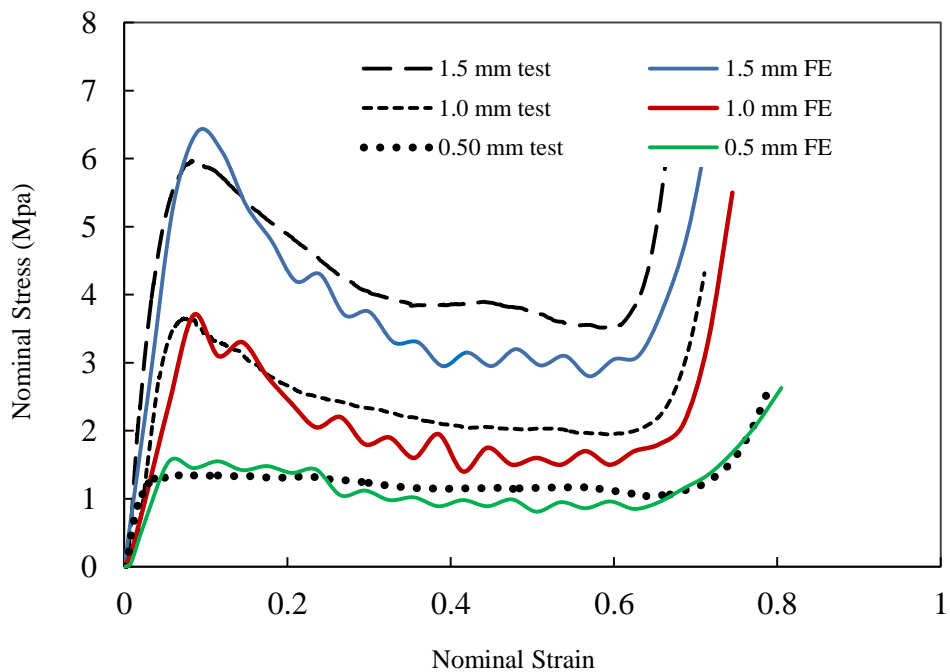


Figure 5.14 Various level of deformation in the flat-roof glass fibre contoured panel during compression (*displacement ratio=displacement/the original height of the core).



(a) GFRP



(b) CFRP

Figure 5.15 Quasi-static stress-strain traces following compression tests on the spherical-roof contoured panels.

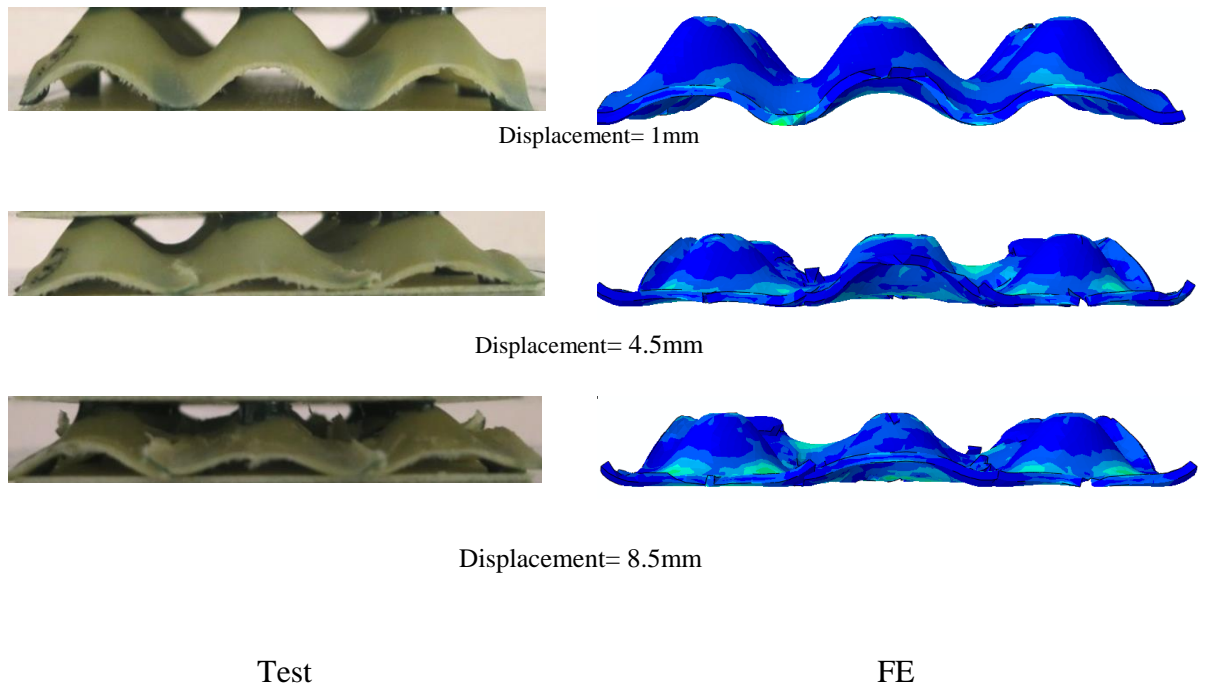


Figure 5.16 Various level of deformation in the spherical-roof glass fibre contoured panel during compression.

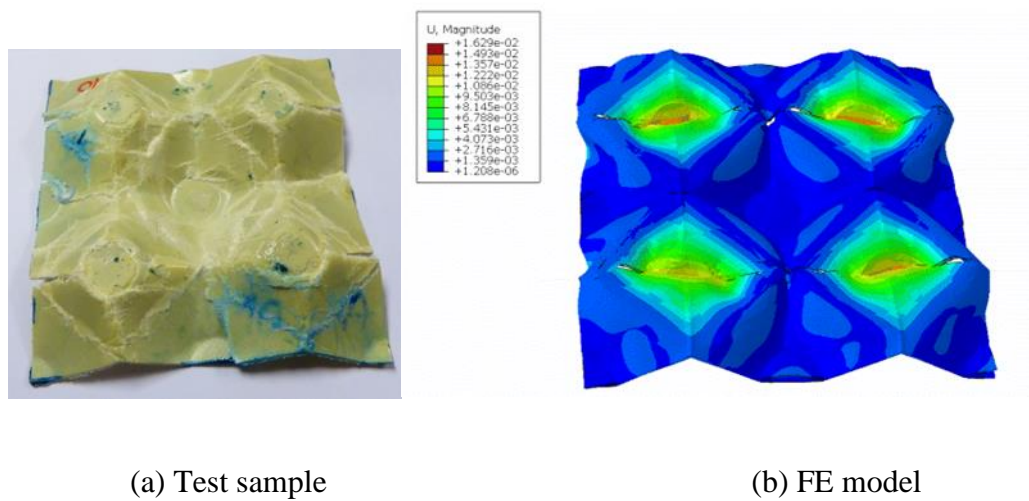


Figure 5.17 Ultimately collapsed flat-roof contoured core (legend in meter).

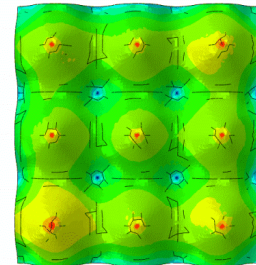
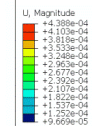
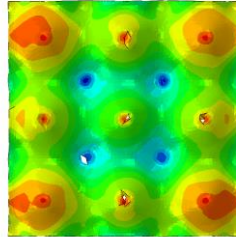
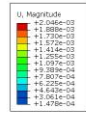
Displacement

ratio*

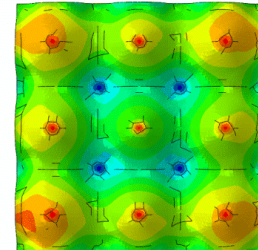
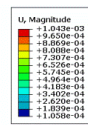
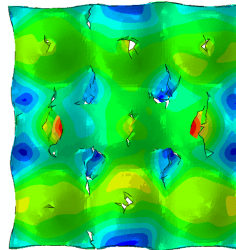
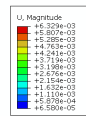
GFRP

CFRP

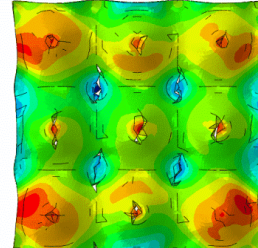
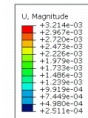
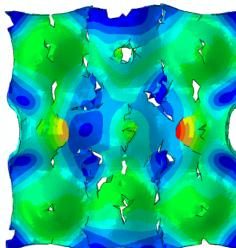
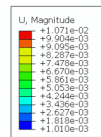
0.15



0.45



0.75



0.75

(crushed samples)

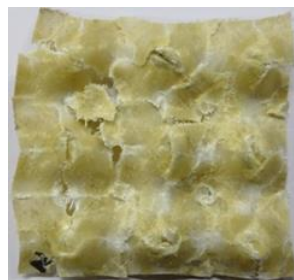


Figure 5.18 Crushed core of spherical-roof contoured panels (*displacement ratio=displacement/the original height of the core).

5.8 The effect of varying the number of unit cells

Further, numerical modelling of a unit cell and a 2x2 unit cell made of GFRP and CFRP were carried out on those spherical roof contoured cores to provide more comparisons of the experimental failure mode and the simulated one. Figure 5.19 and Figure 5.20 show such comparisons, which clearly indicate that the numerical model provides the reasonably good predictions of the failure modes.

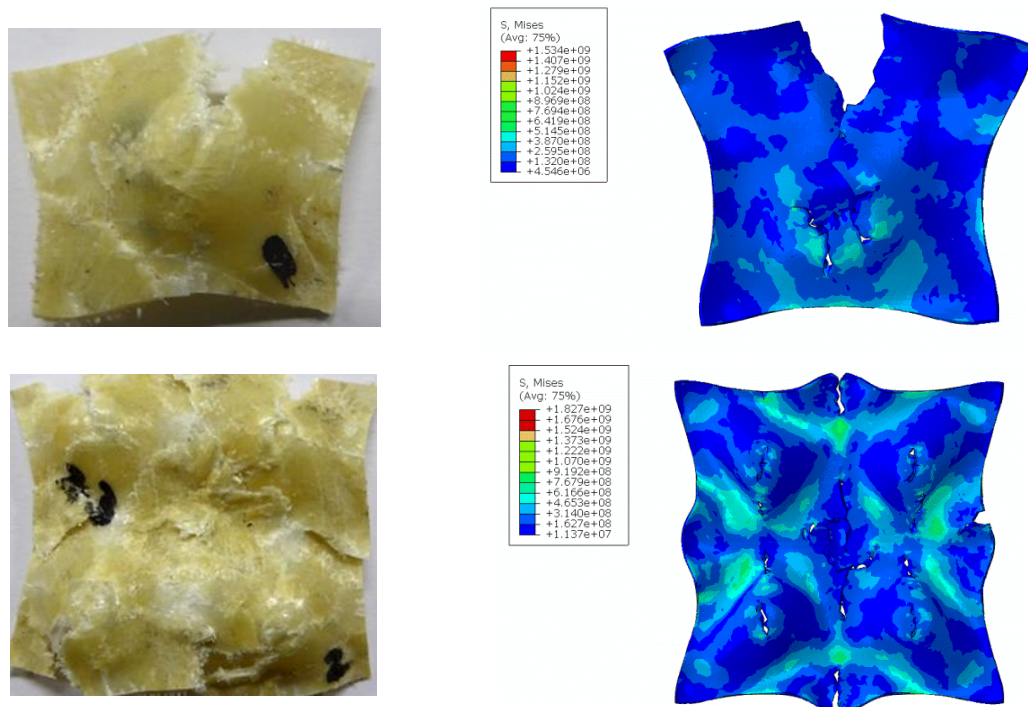


Figure 5.19 Comparison of the 1x1 and 2x2 unit cells of GFRP predicted by the numerical model with the experimental samples.

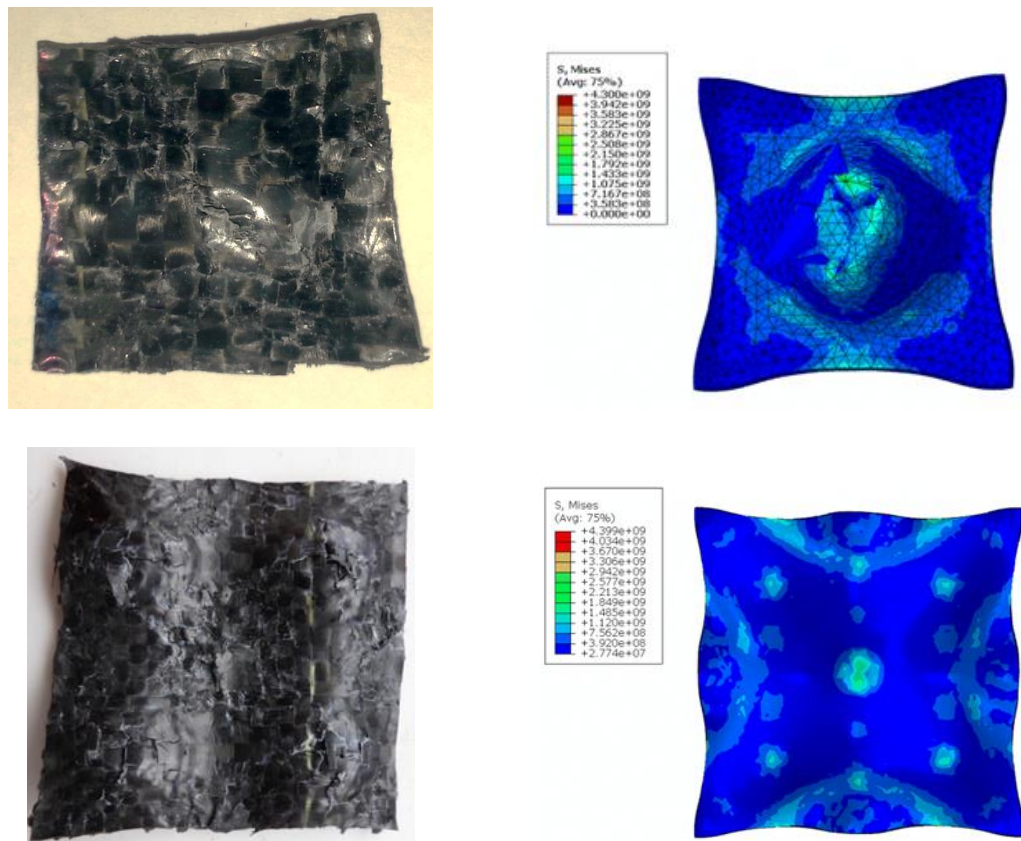


Figure 5.20 Comparison of the 1x1 and 2x2 unit cells of CFRP predicted by the numerical model with the experimental samples.

5.9 Specific energy absorption

Figure 5.21 compares the experimental results and the FE predictions for the SEA of the sandwich cores, under quasi-static loading as a function of cell wall thicknesses. Here, solid and dotted lines in the figure correspond to the FE predictions. The values from the parametric studies with reduced cell wall thicknesses (0.1 mm and 0.3 mm) are also included, which has followed the similar trend as for other three thicknesses. The experimental and FE results have shown a reasonably good agreement with each other. The results show that the SEA of the sandwich model was increased with increasing cell wall thicknesses, as expected. Therefore, these models can be used for

further parametric studies to assist in designing and optimising the structural behaviour of lightweight energy-absorbing sandwich structures, including different material properties and stacking sequences.

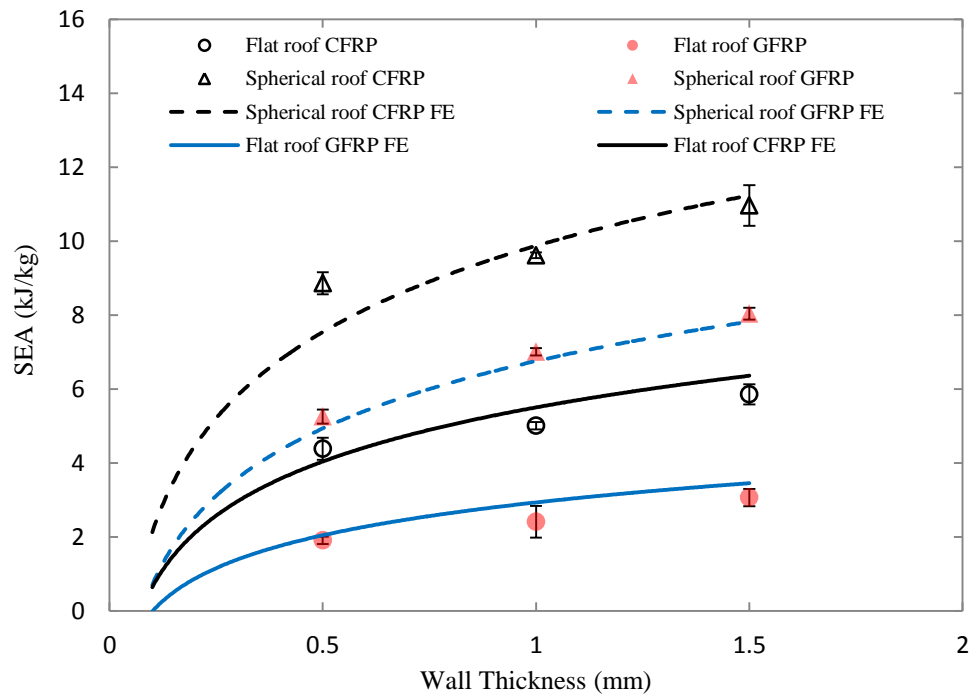


Figure 5.21 Specific energy absorption of Spherical-roof and Flat-roof contoured structures made of CFRP and GFRP.

Summary of the chapter

This chapter presents the details of the FE modelling procedures and discussion on validating the modelling output against the results the experimental data. Abaqus/Explicit was used in simulating the quasi-static and low velocity impact test results. In general, the numerical models are in a good agreement with the related test results in terms of the essential features of the experimental stress-strain traces and failure modes. The evidence suggests that the FE modelling techniques developed could be used to model contoured-core sandwich structures with different material properties and geometries.

Chapter 6. Conclusions and recommendations for future work

6.1 Introduction:

In this chapter, the major findings of the current research are summarized. Following this, recommendations for future work will be given.

6.2 Conclusions of the research work

A series of experimental and numerical work was undertaken to investigate the mechanical properties of novel contoured-core sandwich structures made from the GFRP and CFRP composite materials. Based on the outputs of this work, the following conclusions can be drawn.

Novel Sandwich structures were designed.

Novel lightweight structures based on contoured cores were fabricated using specially designed moulds that were manufactured using CNC machine. Two different profiles of contoured cores were designed, named flat-roof and spherical-roof contour cores respectively. Sandwich structures were fabricated by bonding these contoured cores and skins made from GFRP and CFRP.

Mechanical performance of the contoured-core sandwich structures subjected to various loading was evaluated.

The effects of geometry, material type, cell wall thicknesses, different constraints and number of unit cells were investigated under quasi-static compression and low velocity impact loading. The key mechanical properties under static compression, such as compression strength, stiffness and energy absorption characteristics were recorded for each contoured-core sandwich specimen. The structures showed an excellent repeatability in terms of their mechanical response. The peak load and specific energy absorption increased rapidly with increasing cell wall thickness and

number of unit cells. It was noticed that the stiffness and the plateau stresses were higher for the CFRP panels than their GFRP counterparts, resulting in the higher level of energy absorption of the former. It was also observed that the spherical-roof contoured panels out-perform their flat -roof counterparts.

The impact response of contoured panels to a fully-crashed failure mode was also investigated. Virtually all of the impact energy was absorbed by the panels. It had shown a rate sensitivity effect with the enhanced response for the GFRP and CFRP specimens for both the geometries. However, GFRP was more rate-sensitive than the CFRP specimens under low velocity impact loading.

In addition a series of blast tests was conducted on the spherical roof contoured sandwich structures with aluminum facing sheets. The progressive failure mechanisms observed in these panels highlight the potential of the spherical roof GFRP and CFRP contour cores, suggesting that these structures represent an attractive option for their use in dynamically-loaded structures.

The performance of these panels were compared with similar existing designs (egg box panels) based on aluminium, GFRP and CFRP. The current composite designs offer excellent level of energy absorption per unit mass relative to previous egg-box panels.

Failure mechanisms in contoured-core sandwich structures were investigated.

Quasi-static compression tests were interrupted at certain crosshead displacements to visualize the geometric deformation and to find out the reason of superior performance of the spherical-roof. It was seen that the composite contoured-core specimens failed due to fiber fracture and matrix cracking after the initial instability in

the cones. The inward dimpling was observed in composites cores. These inward dimpling occurred due to the buckling and post-buckling in composites plies. At the end of loading case skins were debonded with the core in most of the sandwich panels.

In comparison to the other panels, the higher energy absorption capacities of these novel spherical-contoured panels are likely attributed to the progressive failure of fiber and matrix, due to the specific contoured geometry of the structure. Initial cracking in egg-box (flat-roof contoured cores) panels occurred at the circular perimeters of the upper and lower surfaces that are in contact with the plates/skins, as a result of stress concentrations. However, no such regions of weakness exist in the spherical-roof, which may explain the great improvement in structural performance. The curvy geometry of spherical-roof contoured also does not allow a catastrophic buckling failure during cyclic loading. Due to these advantages of curvy geometry, spherical-roof contoured panels outperformed the flat-roof contoured panels.

Effect of varying parameters and the properties of foam-filled structures were analyzed.

Varying the number of unit cells, cell wall thickness and core geometry has a significant influence on the compression behaviour of the contoured core sandwich structures. The compression strength and stiffness and specific energy increases with increasing numbers of unit cell and cell wall thickness. In general, the spherical-roof contoured panels have excellent energy absorbing capacities, with values up to ten times better than the corresponding aluminum egg- box panels. Also, it is almost 50 to 60 percent better than the existing composite egg-box panels. Filling the contoured-core sandwich structures with foam significantly improved the specific strength as well as the specific energy absorption characteristics of the structures.

Finite element techniques were developed.

Finite element models were developed to predict the compressive properties of contoured-cores under the conditions of axial crushing. Initial modeling technique adopted for composite contoured-cores was based on composite layup using conventional shell elements with 2D Hashin's failure criteria. A mesh sensitivity analysis was also performed in this investigation which generated a reasonable mesh size for use in the FE models. Buckling imperfection was introduced in the model. The FE response with an initial imperfection of 5 percent through the thickness showed a good agreement with the measured response.

Further, a user-defined constitutive model with modified Hashin's 3D damage criteria was implemented into finite element models using a vectorized user material subroutine (VUMAT) for the composite layers to predict behaviour of contoured-cores through the thickness. The validated finite element models, which cover different cell wall thicknesses and number of unit cells, are ready to be used for further parametric studies of contoured-cores with various configurations subjected to different loading conditions.

Overall, the predicted SEA and deformations of contoured-cores corresponded closely with the experimental observations, indicating that the model developed is capable of predicting the response of these panels.

The current design of the spherical-roof contoured core provides some significant characteristics, which make it more interesting and functional due to the following features:

- Flexibility in design, geometric parameters like core height, thickness and cone angle can be varied to achieve the desired performance for specific applications.
- The manufacturing cost of this design is less expensive due to less complex industrial process when compared to honeycombs or metal foams.
- It can be stacked one over another to minimise the packaging space as the panels.
- The open channel of the geometry provides the air flow exchange, and therefore it can improve the mechanical performance by avoiding the problems associated with humidity retention.

6.3 Recommendations for future work

From the above conclusions, it can be seen that this comprehensive study has contributed to a deep understanding of the development of contoured core systems. However, there is still much research that could be explored to build on the results achieved in this work. The following points address the areas which could be further investigated and highlight important aspects that need to be considered in conducting future research work.

- Some repeated impact tests can be carried out to investigate residual strength of the contoured-core structures.

- Various geometrical modifications such as cone angle, height and contoured wavy shapes can be optimized which may perform more satisfactorily as energy absorbers.
- It would be interesting to undertake the further parametric studies by varying the material properties, stacking sequences in composites and the size of the contoured-core sandwich structures using the numerical modelling developed.
- Efforts can be taken to minimise the FEM computational time by using smart computer.

References

- [1] K. Friedrich and A. A. Almajid, "Manufacturing aspects of advanced polymer composites for automotive applications," *Applied Composite Materials*, vol. 20, pp. 107-128, 2013.
- [2] "Interdisciplinary Labs Using Materials Science Module On Composites (<http://materialsworld.utep.edu/Modules/Composite/>)."
- [3] Furniture, (<http://ammonitum.com/bathroomware/material/furniture/>).
- [4] S. Kazemahvazi and D. Zenkert, "Corrugated all-composite sandwich structures. Part 1: Modeling," *Composites Science and Technology*, vol. 69, pp. 913-919, 2009.
- [5] Y. K. Lin, H. K. Liu, W. S. Kuo, and Y. D. Chen, "Fracture evolution in thick composites under compression," *Polymer Composites*, vol. 28, pp. 425-436, 2007.
- [6] S. H. Chang, M. P. F. Sutcliffe, and S. B. Sharma, "Microscopic investigation of tow geometry changes in a woven prepreg material during draping and consolidation," *Composites Science and Technology*, vol. 64, pp. 1701-1707, 8// 2004.
- [7] M. Rejab and W. Cantwell, "The mechanical behaviour of corrugated-core sandwich panels," *Composites Part B: Engineering*, vol. 47, pp. 267-277, 2013.
- [8] F. Feist, S. Faßbender, R. Puppini, E. Mayrhofer, and T. Smith, "Impact situations and pedestrian/cyclist kinematics based on real world accident scenarios," *APROSYS Deliverables*, 2006.
- [9] S. Nowpada, E. Chirwa, P. Myler, G. K. Chinnaswamy, and E. Matsika, "'Egg-box' panel for commercial vehicle front-compressive loading tests," *International Journal of Crashworthiness*, vol. 15, pp. 59-70, 2010.
- [10] "Australasian New Car Assessment Program (ANCAP) website - Crash Testing Explained (<http://www.ancap.com.au/crashtesting/>)."
- [11] A. A. A. Alghamdi, "Collapsible impact energy absorbers: an overview," *Thin-Walled Structures*, vol. 39, pp. 189-213, 2// 2001.
- [12] S. Lam, X. Tao, and T. Yu, "Comparison of different thermoplastic cellular textile composites on their energy absorption capacity," *Composites Science and Technology*, vol. 64, pp. 2177-2184, 2004.

- [13] T. Yu, X. Tao, and P. Xue, "The energy-absorbing capacity of grid-domed textile composites," *Composites Science and Technology*, vol. 60, pp. 785-800, 2000.
- [14] C. Soutis and R. Poubady, "Crush energy absorption of woven CFRP laminates," *In IMechE Seminar Publication on Foreign Object Impact & Energy Absorbing Structure*, 1998.
- [15] O. Velecela, M. Found, and C. Soutis, "Crushing energy absorption of GFRP sandwich panels and corresponding monolithic laminates," *Composites Part A: Applied Science and Manufacturing*, vol. 38, pp. 1149-1158, 2007.
- [16] M. Zupan, N. Fleck, and M. Ashby, "The collapse and energy absorption of egg-box panels," in *Proceedings of the 3rd TMS Annual Meeting and Exhibition*, 2002, pp. 243-250.
- [17] S. H. Yoo and S. H. Chang, "An experimental study on energy absorbing structures made of fabric composites," *Composite Structures*, vol. 86, pp. 211-219, 2008.
- [18] S. Yoo, S. Chang, and M. Sutcliffe, "Compressive characteristics of foam-filled composite egg-box sandwich panels as energy absorbing structures," *Composites Part A: Applied Science and Manufacturing*, vol. 41, pp. 427-434, 2010.
- [19] *Federal Aviation Administration, Aviation Maintenance Technician Handbook- Airframe, Chapter 7, (available online) follow the link- https://www.faa.gov/regulations_policies/handbooks_manuals/aircraft/amt_airframe_handbook/*
- [20] M. Ashby, "The properties of foams and lattices," *Philosophical Transactions of the Royal Society of London A: Mathematical, Physical and Engineering Sciences*, vol. 364, pp. 15-30, 2006.
- [21] L. J. Gibson and M. F. Ashby, *Cellular solids: structure and properties*: Cambridge university press, 1997.
- [22] H. N. Wadley, "Multifunctional periodic cellular metals," *Philosophical Transactions of the Royal Society A: Mathematical, Physical and Engineering Sciences*, vol. 364, pp. 31-68, 2006.
- [23] K. W. Suh, "Foamed plastics," *Kirk-Othmer Encyclopedia of Chemical Technology*, 1980.
- [24] M. E. Kabir, M. Saha, and S. Jeelani, "Tensile and fracture behavior of polymer foams," *Materials Science and Engineering: A*, vol. 429, pp. 225-235, 2006.

- [25] J. P. Bratfisch, D. Vandepitte, J. Pflug, and I. Verpoest, "Development and Validation of A Continuous Production Concept for Thermoplastic Honeycomb," in *Sandwich Structures 7: Advancing with Sandwich Structures and Materials*, ed: Springer, 2005, pp. 763-772.
- [26] F. Zok*, H. Rathbun, M. He, E. Ferri, C. Mercer, R. McMeeking, *et al.*, "Structural performance of metallic sandwich panels with square honeycomb cores," *Philosophical Magazine*, vol. 85, pp. 3207-3234, 2005.
- [27] B. Russell, V. Deshpande, and H. Wadley, "Quasistatic deformation and failure modes of composite square honeycombs," *Journal of Mechanics of Materials and Structures*, vol. 3, pp. 1315-1340, 2008.
- [28] N. Buannic, P. Cartraud, and T. Quesnel, "Homogenization of corrugated core sandwich panels," *Composite Structures*, vol. 59, pp. 299-312, 2003.
- [29] T. Nordstrand, "Parametric study of the post-buckling strength of structural core sandwich panels," *Composite structures*, vol. 30, pp. 441-451, 1995.
- [30] T. Nordstrand and L. Carlsson, "Evaluation of transverse shear stiffness of structural core sandwich plates," *Composite Structures*, vol. 37, pp. 145-153, 1997.
- [31] M. Biancolini, "Evaluation of equivalent stiffness properties of corrugated board," *Composite Structures*, vol. 69, pp. 322-328, 2005.
- [32] M. Biancolini, C. Brutti, and S. Porziani, "Analysis of corrugated board panels under compression load," *Steel and Composite Structures*, 2009.
- [33] Z. Aboura, N. Talbi, S. Allaoui, and M. Benzeggagh, "Elastic behavior of corrugated cardboard: experiments and modeling," *Composite Structures*, vol. 63, pp. 53-62, 2004.
- [34] T. Yokozeki, S.-i. Takeda, T. Ogasawara, and T. Ishikawa, "Mechanical properties of corrugated composites for candidate materials of flexible wing structures," *Composites Part A: Applied Science and Manufacturing*, vol. 37, pp. 1578-1586, 2006.
- [35] R. Ge, B. Wang, C. Mou, and Y. Zhou, "Deformation characteristics of corrugated composites for morphing wings," *Frontiers of Mechanical Engineering in China*, vol. 5, pp. 73-78, 2010.
- [36] A. Gilchrist, J. Suhling, and T. Urbanik, "Nonlinear finite element modeling of corrugated board," *ASME APPLIED MECHANICS DIVISION-PUBLICATIONS-AMD*, vol. 231, pp. 101-106, 1998.

- [37] A. Krusper, P. Isaksson, and P. Gradin, "Modeling of out-of-plane compression loading of corrugated paper board structures," *Journal of engineering mechanics*, vol. 133, pp. 1171-1177, 2007.
- [38] J. Wallach and L. Gibson, "Mechanical behavior of a three-dimensional truss material," *International Journal of Solids and Structures*, vol. 38, pp. 7181-7196, 2001.
- [39] M. Smith, Z. Guan, and W. Cantwell, "Finite element modelling of the compressive response of lattice structures manufactured using the selective laser melting technique," *International Journal of Mechanical Sciences*, vol. 67, pp. 28-41, 2013.
- [40] R. Gümruk, R. Mines, and S. Karadeniz, "Static mechanical behaviours of stainless steel micro-lattice structures under different loading conditions," *Materials Science and Engineering: A*, vol. 586, pp. 392-406, 2013.
- [41] G. Movchan, "Analysis of folded structures for impact resistance," *Russian Aeronautics (Iz VUZ)*, vol. 50, pp. 439-441, 2007.
- [42] M. Kintscher, L. Kärger, A. Wetzel, and D. Hartung, "Stiffness and failure behaviour of folded sandwich cores under combined transverse shear and compression," *Composites Part A: Applied Science and Manufacturing*, vol. 38, pp. 1288-1295, 2007.
- [43] B. B. Basily and E. Elsayed, "Dynamic axial crushing of multilayer core structures of folded Chevron patterns," *International Journal of Materials and Product Technology*, vol. 21, pp. 169-185, 2004.
- [44] V.T. Nguyen, J.-F. Caron, and K. Sab, "A model for thick laminates and sandwich plates," *Composites Science and Technology*, vol. 65, pp. 475-489, 2005.
- [45] S. Heimbs, T. Mehrens, P. Middendorf, A. Maier, and M. Schumacher, "Numerical determination of the nonlinear effective mechanical properties of folded core structures for aircraft sandwich panels," in *6th European LS DYNA User's Conference*, 2006.
- [46] A. Lebé and K. Sab, "Transverse shear stiffness of a chevron folded core used in sandwich construction," *International Journal of Solids and Structures*, vol. 47, pp. 2620-2629, 2010.
- [47] M. Ashmead, "Energy absorbing bumper structure," ed: Google Patents, 2001.
- [48] J. Chung, S. Chang, and M. Sutcliffe, "Deformation and energy absorption of composite egg-box panels," *Composites Science and Technology*, vol. 67, pp. 2342-2349, 2007.

- [49] P. Du Bois, C. C. Chou, B. B. Fileta, T. B. Khalil, A. I. King, H. F. Mahmood, *et al.*, "Automotive Applications Committee American Iron and Steel Institute Southfield, Michigan."
- [50] M. Ashmead, "Energy-absorbing structures," ed: Google Patents, 2003.
- [51] J. Alexander, "An approximate analysis of the collapse of thin cylindrical shells under axial loading," *The Quarterly Journal of Mechanics and Applied Mathematics*, vol. 13, pp. 10-15, 1960.
- [52] W. Abramowicz and N. Jones, "Dynamic progressive buckling of circular and square tubes," *International Journal of Impact Engineering*, vol. 4, pp. 243-270, 1986.
- [53] P. Qiao, M. Yang, and F. Bobaru, "Impact mechanics and high-energy absorbing materials: review," *Journal of Aerospace Engineering*, vol. 21, pp. 235-248, 2008.
- [54] Z. Ahmad and D. Thambiratnam, "Crushing response of foam-filled conical tubes under quasi-static axial loading," *Materials & design*, vol. 30, pp. 2393-2403, 2009.
- [55] M. Avalle, G. Belingardi, and A. Ibba, "Mechanical models of cellular solids: Parameters identification from experimental tests," *International Journal of Impact Engineering*, vol. 34, pp. 3-27, 2007.
- [56] S. Reid, "Plastic deformation mechanisms in axially compressed metal tubes used as impact energy absorbers," *International Journal of Mechanical Sciences*, vol. 35, pp. 1035-1052, 1993.
- [57] G. M. Nagel and D. P. Thambiratnam, "Dynamic simulation and energy absorption of tapered thin-walled tubes under oblique impact loading," *International Journal of Impact Engineering*, vol. 32, pp. 1595-1620, 2006.
- [58] L. Mirfendereski, M. Salimi, and S. Ziaei-Rad, "Parametric study and numerical analysis of empty and foam-filled thin-walled tubes under static and dynamic loadings," *International Journal of Mechanical Sciences*, vol. 50, pp. 1042-1057, 2008.
- [59] M. Shariatpanahi, A. Masoumi, and A. Ataei, "Optimum design of partially tapered rectangular thin-walled tubes in axial crushing," *Proceedings of the Institution of Mechanical Engineers, Part B: Journal of Engineering Manufacture*, vol. 222, pp. 285-291, 2008.
- [60] S. Reid and T. Reddy, "Static and dynamic crushing of tapered sheet metal tubes of rectangular cross-section," *International Journal of Mechanical Sciences*, vol. 28, pp. 623-637, 1986.

- [61] N. Gupta, "Experimental and numerical studies of impact axial compression of thin-walled conical shells," *International Journal of Impact Engineering*, vol. 34, pp. 708-720, 2007.
- [62] N. Gupta and R. Velmurugan, "Axial compression of empty and foam filled composite conical shells," *Journal of Composite Materials*, vol. 33, pp. 567-591, 1999.
- [63] A. Singace, H. El-Sobky, and M. Petsios, "Influence of end constraints on the collapse of axially impacted frusta," *Thin-walled structures*, vol. 39, pp. 415-428, 2001.
- [64] G. E. Prasad and N. Gupta, "An experimental study of deformation modes of domes and large-angled frusta at different rates of compression," *International Journal of Impact Engineering*, vol. 32, pp. 400-415, 2005.
- [65] A. Mamalis, D. Manolakos, M. Ioannidis, and P. Kostazos, "Numerical simulation of thin-walled metallic circular frusta subjected to axial loading," *International Journal of Crashworthiness*, vol. 10, pp. 505-513, 2005.
- [66] V. Deshpande and N. Fleck, "Energy absorption of an egg-box material," *Journal of the Mechanics and Physics of Solids*, vol. 51, pp. 187-208, 2003.
- [67] S. Nowpada, E. C. Chirwa, P. Myler, G. K. Chinnaswamy, and E. Matsika, "'Egg-box' panel for commercial vehicle front – compressive loading tests," *International Journal of Crashworthiness*, vol. 15, pp. 59-70, 2010/03/23 2010.
- [68] W. Johnson and A. G. Mamalis, "Crashworthiness of vehicles," 0954-4070, 1978.
- [69] T. Wierzbicki and W. Abramowicz, "On the crushing mechanics of thin-walled structures," *Journal of Applied Mechanics*, vol. 50, pp. 727-734, 1983.
- [70] A. Deb, M. Mahendrakumar, C. Chavan, J. Karve, D. Blankenburg, and S. Storen, "Design of an aluminium-based vehicle platform for front impact safety," *International Journal of Impact Engineering*, vol. 30, pp. 1055-1079, 2004.
- [71] M. Zupan, C. Chen, and N. Fleck, "The plastic collapse and energy absorption capacity of egg-box panels," *International Journal of Mechanical Sciences*, vol. 45, pp. 851-871, 2003.
- [72] M. Sanaei and A. Shirvani, "Energy Absorption Characteristics of Aluminum Egg-box Structure Subjected to Experimental Impact."
- [73] A. Mamalis, W. Johnson, and G. Viegelaahn, "The crumpling of steel thin-walled tubes and frusta under axial compression at elevated strain-rates: some

- experimental results," *International Journal of Mechanical Sciences*, vol. 26, pp. 537-547, 1984.
- [74] J. G. De Oliveira and T. Wierzbicki, "Crushing analysis of rotationally symmetric plastic shells," *The Journal of Strain Analysis for Engineering Design*, vol. 17, pp. 229-236, 1982.
- [75] S. Nowpada, E. C. Chirwa, P. Myler, and E. Matsika, "Aluminum "Egg-Box" Panel as an Energy Absorber for Pedestrian Protection," *Advanced Engineering Materials*, vol. 12, pp. 591-595, 2010.
- [76] W. J. Stronge, *Impact Mechanics*: Cambridge university press, 2004.
- [77] M. Wali, M. Abdennadher, T. Fakhfakh, and M. Haddar, "Dynamic analysis of an elasto-plastic sandwich subjected to low velocity impact," *Multidiscipline Modeling in Materials and Structures*, vol. 7, pp. 184-206, 2011.
- [78] Y. Shen, "High-performance sandwich structures based on novel metal cores," University of Liverpool, 2009.
- [79] M. A. Hazizan and W. Cantwell, "The low velocity impact response of foam-based sandwich structures," *Composites Part B: Engineering*, vol. 33, pp. 193-204, 2002.
- [80] D. Cartie and P. Irving, "Effect of resin and fibre properties on impact and compression after impact performance of CFRP," *Composites Part A: Applied Science and Manufacturing*, vol. 33, pp. 483-493, 2002.
- [81] M. Akay and R. Hanna, "A comparison of honeycomb-core and foam-core carbon-fibre/epoxy sandwich panels," *Composites*, vol. 21, pp. 325-331, 1990.
- [82] P. Compston, M. Styles, and S. Kalyanasundaram, "Low energy impact damage modes in aluminum foam and polymer foam sandwich structures," *Journal of Sandwich Structures and Materials*, vol. 8, pp. 365-379, 2006.
- [83] G. Caprino and R. Teti, "Impact and post-impact behavior of foam core sandwich structures," *Composite Structures*, vol. 29, pp. 47-55, 1994.
- [84] G. Zhou, M. Hill, J. Loughlan, and N. Hookham, "Damage characteristics of composite honeycomb sandwich panels in bending under quasi-static loading," *Journal of Sandwich Structures and Materials*, vol. 8, pp. 55-90, 2006.
- [85] F. Zhu, G. Lu, D. Ruan, and Z. Wang, "Plastic deformation, failure and energy absorption of sandwich structures with metallic cellular cores," *International Journal of Protective Structures*, vol. 1, pp. 507-541, 2010.

- [86] G. McShane, D. Radford, V. Deshpande, and N. Fleck, "The response of clamped sandwich plates with lattice cores subjected to shock loading," *European Journal of Mechanics-A/Solids*, vol. 25, pp. 215-229, 2006.
- [87] A. Hanssen, L. Enstock, and M. Langseth, "Close-range blast loading of aluminium foam panels," *International Journal of Impact Engineering*, vol. 27, pp. 593-618, 2002.
- [88] N. Jacob, G. Nurick, and G. Langdon, "The effect of stand-off distance on the failure of fully clamped circular mild steel plates subjected to blast loads," *Engineering Structures*, vol. 29, pp. 2723-2736, 2007.
- [89] G. Langdon, D. Karagiozova, M. Theobald, G. Nurick, G. Lu, and R. Merrett, "Fracture of aluminium foam core sacrificial cladding subjected to air-blast loading," *International Journal of Impact Engineering*, vol. 37, pp. 638-651, 2010.
- [90] M. F. Ashby, T. Evans, N. A. Fleck, J. Hutchinson, H. Wadley, and L. Gibson, *Metal Foams: A Design Guide: A Design Guide*: Elsevier, 2000.
- [91] G. L. Farley, "Effect of specimen geometry on the energy absorption capability of composite materials," *Journal of Composite Materials*, vol. 20, pp. 390-400, 1986.
- [92] C. Chen, A. Harte, and N. Fleck, "The plastic collapse of sandwich beams with a metallic foam core," *International Journal of Mechanical Sciences*, vol. 43, pp. 1483-1506, 2001.
- [93] A. Reyes, O. Hopperstad, and M. Langseth, "Aluminum foam-filled extrusions subjected to oblique loading: experimental and numerical study," *International Journal of Solids and Structures*, vol. 41, pp. 1645-1675, 2004.
- [94] A. Mamalis, D. Manolakos, M. Ioannidis, P. Kostazos, and G. Hassiotis, "Finite element simulation of the axial collapse of thin-wall square frusta," *International Journal of Crashworthiness*, vol. 6, pp. 155-164, 2001.
- [95] M. Ulker, M. S. Rahman, R. Zhen, and A. Mirmiran, "Traffic barriers under vehicular impact: from computer simulation to design guidelines," *Computer-Aided Civil and Infrastructure Engineering*, vol. 23, pp. 465-480, 2008.
- [96] A.-G. Olabi, E. Morris, M. Hashmi, and M. D. Gilchrist, "Optimised design of nested oblong tube energy absorbers under lateral impact loading," *International Journal of Impact Engineering*, vol. 35, pp. 10-26, 2008.
- [97] E. Morris, A.-G. Olabi, and M. Hashmi, "Analysis of nested tube type energy absorbers with different indenters and exterior constraints," *Thin-walled structures*, vol. 44, pp. 872-885, 2006.

- [98] Z. Zhang, S. Liu, and Z. Tang, "Crashworthiness investigation of kagome honeycomb sandwich cylindrical column under axial crushing loads," *Thin-Walled Structures*, vol. 48, pp. 9-18, 2010.
- [99] D. Karagiozova, M. Alves, and N. Jones, "Inertia effects in axisymmetrically deformed cylindrical shells under axial impact," *International Journal of Impact Engineering*, vol. 24, pp. 1083-1115, 2000.
- [100] D. Karagiozova and N. Jones, "Dynamic buckling of elastic-plastic square tubes under axial impact—II: structural response," *International Journal of Impact Engineering*, vol. 30, pp. 167-192, 2004.
- [101] A. Aljawi, "Finite element and experimental analysis of axially compressed plastic tubes," *European journal of Mechanical and Environmental Engineering*, vol. 45, pp. 3-10, 2000.
- [102] M. Tilbrook, D. Radford, V. Deshpande, and N. Fleck, "Dynamic crushing of sandwich panels with prismatic lattice cores," *International Journal of Solids and Structures*, vol. 44, pp. 6101-6123, 2007.
- [103] Q. Qin, J. Zhang, and T. Wang, "Low velocity impact response of lightweight metal sandwich panel with corrugated core," *Materials Research Innovations*, vol. 15, pp. s198-s200, 2011.
- [104] A. Vaziri, Z. Xue, and J. W. Hutchinson, "Metal sandwich plates with polymer foam-filled cores," *Journal of Mechanics of Materials and Structures*, vol. 1, pp. 97-127, 2006.
- [105] M. Avalle, G. Chiandussi, and G. Belingardi, "Design optimization by response surface methodology: application to crashworthiness design of vehicle structures," *Structural and Multidisciplinary Optimization*, vol. 24, pp. 325-332, 2002.
- [106] K. K. Choi and B. D. Youn, "An investigation of nonlinearity of reliability-based design optimization approaches," in *ASME 2002 International Design Engineering Technical Conferences and Computers and Information in Engineering Conference*, 2002, pp. 881-890.
- [107] A.-M. Harte, N. A. Fleck, and M. F. Ashby, "Energy absorption of foam-filled circular tubes with braided composite walls," *European Journal of Mechanics-A/Solids*, vol. 19, pp. 31-50, 2000.
- [108] N. Gupta, "A study of the influence of diameter and wall thickness of cylindrical tubes on their axial collapse," *Thin-Walled Structures*, vol. 44, pp. 290-300, 2006.
- [109] Y. Liu, "Design optimisation of tapered thin-walled square tubes," *International Journal of Crashworthiness*, vol. 13, pp. 543-550, 2008.

- [110] S. Hou, Q. Li, S. Long, X. Yang, and W. Li, "Design optimization of regular hexagonal thin-walled columns with crashworthiness criteria," *Finite Elements in Analysis and Design*, vol. 43, pp. 555-565, 2007.
- [111] A. Spagnoli and M. Chryssanthopoulos, "Elastic buckling and postbuckling behaviour of widely-stiffened conical shells under axial compression," *Engineering Structures*, vol. 21, pp. 845-855, 1999.
- [112] A. Akisanya and N. Fleck, "Plastic collapse of thin-walled frusta and egg-box material under shear and normal loading," *International Journal of Mechanical Sciences*, vol. 48, pp. 799-808, 2006.
- [113] "BS. Plastic - Determination of Tensile Properties," *Part 4: testing condition for isotropic and orthotropic fiber reinforced plastic composites*, vol. 527-4, 1997.
- [114] "ASTM standard test method for compressive properties of rigid cellular plastic " 2000.
- [115] G. S. Langdon, D. Karagiozova, M. D. Theobald, G. N. Nurick, G. Lu, and R. P. Merrett, "Fracture of aluminium foam core sacrificial cladding subjected to air-blast loading," *International Journal of Impact Engineering*, vol. 37, pp. 638-651, 6// 2010.
- [116] <http://www.bisru.uct.ac.za/>.
- [117] R. Mines, Q. Li, A. Alias, R. Birch, and J. Close, "On the measurement of the crush behaviour of structural foams," *Experimental Mechanics*, vol. 1, p. 287, 1998.
- [118] N. Gupta and G. E. Prasad, "Quasi-static and dynamic axial compression of glass/polyester composite hemi-spherical shells," *International Journal of Impact Engineering*, vol. 22, pp. 757-774, 1999.
- [119] M. Smith, W. Cantwell, Z. Guan, S. Tsopanos, M. Theobald, G. Nurick, *et al.*, "The quasi-static and blast response of steel lattice structures," *Journal of Sandwich Structures and Materials*, vol. 13, pp. 479-501, 2011.
- [120] S. Palanivelu, W. Van Paepegem, J. Degrieck, D. Kakogiannis, J. Van Ackeren, D. Van Hemelrijck, *et al.*, "Parametric study of crushing parameters and failure patterns of pultruded composite tubes using cohesive elements and seam, Part I: Central delamination and triggering modelling," *Polymer Testing*, vol. 29, pp. 729-741, 2010.
- [121] Z. Hashin, "Failure criteria for unidirectional fiber composites," *Journal of Applied Mechanics*, vol. 47, pp. 329-334, 1980.

- [122] A.Ruzana, "The Energy-absorbing Characteristics of Novel Tube-reinforced Sandwich Structures,Ph.D Thesis, University of Liverpool," 2015.
- [123] J. Zhou, "The Energy-absorbing Characteristics of Novel Aerospace composite Structures,Ph.D Thesis, University of Liverpool," 2015.
- [124] A. Matzenmiller, J. Lubliner, and R. Taylor, "A constitutive model for anisotropic damage in fiber-composites," *Mechanics of Materials*, vol. 20, pp. 125-152, 1995.
- [125] Z. Hashin, "Analysis of properties of fiber composites with anisotropic constituents," *Journal of Applied Mechanics*, vol. 46, pp. 543-550, 1979.
- [126] T. M. ABAQUS, Version 6.11, Pawtucket, Hibbitt, Karlsson & Sorensen, Inc. , 2012.
- [127] D. Systèmes, "Abaqus 6.13 Online Documentation; 2013," ed.
- [128] R. Alia, Z. Guan, A. Haldar, and W. Cantwell, "A numerical study of the energy-absorption characteristics of metal tube-reinforced polymer foams," *Journal of Sandwich Structures and Materials*, p. 1099636215603035, 2015.
- [129] M. Seitzberger, F. G. Rammerstorfer, H. P. Degischer, and R. Gradinger, "Crushing of axially compressed steel tubes filled with aluminium foam," *Acta Mechanica*, vol. 125, pp. 93-105, 1997.
- [130] F. Côté, V. Deshpande, N. Fleck, and A. Evans, "The compressive and shear responses of corrugated and diamond lattice materials," *International Journal of Solids and Structures*, vol. 43, pp. 6220-6242, 2006.
- [131] M. I. Alam and S. Fawzia, "Numerical studies on CFRP strengthened steel columns under transverse impact," *Composite Structures*, vol. 120, pp. 428-441, 2015.
- [132] J. Harding and L. M. Welsh, "A tensile testing technique for fibre-reinforced composites at impact rates of strain," *Journal of Materials Science*, vol. 18, pp. 1810-1826, 1983.
- [133] D. F. Adams and L. G. Adams, "Tensile impact tests of AS4/3501-6 and S2/3501-6 unidirectional composites and the 3501-6 epoxy matrix," *Journal of Composite Materials*, vol. 24, pp. 256-268, 1990.
- [134] H. Al-Zubaidy, X.-L. Zhao, and R. Al-Mahaidi, "Mechanical characterisation of the dynamic tensile properties of CFRP sheet and adhesive at medium strain rates," *Composite Structures*, vol. 96, pp. 153-164, 2013.

- [135] W. Wang, G. Makarov, and R. Shenoi, "An analytical model for assessing strain rate sensitivity of unidirectional composite laminates," *Composite Structures*, vol. 69, pp. 45-54, 2005.
- [136] J. Hou and C. Ruiz, "Measurement of the properties of woven CFRP T300/914 at different strain rates," *Composites Science and Technology*, vol. 60, pp. 2829-2834, 2000.
- [137] N. Naik, P. Yernamma, N. Thoram, R. Gadipatri, and V. Kavala, "High strain rate tensile behavior of woven fabric E-glass/epoxy composite," *Polymer Testing*, vol. 29, pp. 14-22, 2010.
- [138] T. Gomez-del Rio, E. Barbero, R. Zaera, and C. Navarro, "Dynamic tensile behaviour at low temperature of CFRP using a split Hopkinson pressure bar," *Composites Science and Technology*, vol. 65, pp. 61-71, 2005.
- [139] T. Vo, Z. Guan, W. Cantwell, and G. Schleyer, "Low-impulse blast behaviour of fibre-metal laminates," *Composite Structures*, vol. 94, pp. 954-965, 2012.
- [140] T. Vo, Z. Guan, W. Cantwell, and G. Schleyer, "Low-impulse blast behaviour of fibre-metal lami," 2012.
- [141] Z. Hashin and A. Rotem, "A fatigue failure criterion for fiber reinforced materials," *Journal of Composite Materials*, vol. 7, pp. 448-464, 1973.
- [142] A. Version, "5.8, Hibbitt, Karlsson & Sorensen," *Inc. USA*, 1998.
- [143] D. Karagiozova, G. Langdon, G. Nurick, and S. C. K. Yuen, "Simulation of the response of fibre-metal laminates to localised blast loading," *International Journal of Impact Engineering*, vol. 37, pp. 766-782, 2010.

